MODELING BOUNDARY EFFECT PROBLEMS OF HETEROGENEOUS STRUCTURES BY EXTENDING MECHANICS OF STRUCTURE GENOME

A Dissertation

Submitted to the Faculty

of

Purdue University

by

Bo Peng

In Partial Fulfillment of the

Requirements for the Degree

of

Doctor of Philosophy

May 2019

Purdue University

West Lafayette, Indiana

THE PURDUE UNIVERSITY GRADUATE SCHOOL
STATEMENT OF DISSERTATION APPROVAL

Dr. Wenbin Yu, Chair

School of Aeronautics and Astronautics

Dr. R. Byron Pipes

School of Aeronautics and Astronautics

Dr. Pablo D. Zavattieri

School of Civil Engineering

Dr. Kejie Zhao

School of Mechanical Engineering

Approved by:

Dr. Wayne Chen, Head of the Graduate Program

School of Aeronautics and Astronautics

To my family.

ACKNOWLEDGMENTS

First and foremost, I would like to express my greatest appreciation to my advisor Professor Wenbin Yu for his continuous support, encouragement, and guidance in the last five years. He has taught me more than I could ever give him credit here. I appreciate the advice and guidance he gave me, not only in my research but also for my personal life. He has shown me, by his example, what a good researcher and a good person should be. Without his patience and guidance this dissertation would have not been possible.

My great gratitude also extends to my committee members: Distinguished Professor R. Byron Pipes, Professor Pablo D. Zavattieri and Professor Kejie Zhao for their willingness to review my work and provide their valuable advices and comments on my research.

I would like to thank the Institute for Advanced Composites Manufacturing Innovation (IACMI) for their financial support. My special thanks goes to Professor Weinong Chen for his financial support and encouragement when I was in the hard time of my study. I am also thankful to Professor Vikas Tomar, Professor Johnathan Goodsell for their help in my study and research. I also thank Prof. Michael Sangid for his input in my study.

I would like to thank my colleagues from the Multiscale Structural Mechanics Group at Purdue University: Dr. Tian Tang, Dr. Liang Zhang, Dr. Hamsasew Moges Sertse, Dr. Fang Jiang, Haiqiang She, Ning Liu, Yufei Long, Zhenyuan Gao, Su Tian, Xin Liu, Orzuri Rique Garaizar, Ankit Deo, Kshitiz Swaroop, Lingxuan Zhou, Albert Chang, Banghua Zhao, Ernesto Camarena, Fei Tao, Khizar Rouf, Haodong Du, Rong Chiu, Ye Yu. It is a great experience to work in a team of active minds.

I would like to thank all my lab mates and classmates, especially Benjamin Claus, Genghua Lin for their great help in my course study. My gratitude also goes to the faculty and staff in School of Aeronautics and Astronautics and IACMI for making my time at Purdue University a great experience.

I would also like to thank all my friends and family for the sincere care I have received.

Last but not least, I would like to thank my parents Pengfei Peng and Meicheng Peng for their persistent understanding, encouragement and love all these years. My heartfelt gratitude goes to my husband Junwei Xing for all the support and encouragement from him.

TABLE OF CONTENTS

LIST OF TABLES

LIST OF FIGURES

Figure Page

Figure Page

Figure Page

ABSTRACT

Peng, Bo Ph.D., Purdue University, May 2019. Modeling Boundary Effect Problems of Heterogeneous Structures by Extending Mechanics of Structure Genome. Major Professor: Yu W. Professor.

Heterogeneous structures with complicated micro-structures are comprised of several length scales. In order to analyze heterogeneous structures with reasonable accuracy and cost, numerous multi-scale modeling methods have been developed based on the scale separation assumption, in which the micromechanics and structural analysis models are usually developed separately. However, in cases when this assumption does not stand and thus periodicity is lost or edge effect arises, modeling error might be significant, especially when the local fields in the microstructure are interested.

This work is based on Mechanics of Structure Genome (MSG), in which the micromechanics and structural analysis models are derived from the original heterogeneous model simultaneously, based on the principle of minimum information loss. In previous research works MSG has been developed for periodic heterogeneous solid and beam/plate-like structures. The objective of this work is to extend MSG and its companion code SwiftComp to address two issues due to ambiguous scale separation in some heterogeneous structures.

The first issue is that when the microstructure is not small enough compared with the whole heterogeneous material, micro-structural periodicity can only be observed in part of the three directions of the material. A typical example is the textile composite structures consisting of a small number of layers, in which periodic constraints cannot be applied to the top and bottom surfaces due to the finite thickness of the structure. To address this issue, in this work, the theory of MSG is extended to aperiodic heterogeneous solid structures. Integral constraints are introduced to decompose the

displacements and strains of the heterogeneous material into a fluctuating part and a macroscopic part, of which the macroscopic part represents the responses of the homogenized material. One advantage of this theory is that boundary conditions are not required. Consequently, it is capable of handling micro-structures of arbitrary shapes. In addition, periodic constraints can be incorporated into this theory as needed to model periodic or partially periodic materials such as textile composites. In this study, the newly developed method is employed to investigate the finite thickness effect of textile composites.

Second, the free-edge problem, as a special case of the edge effect, is studied. At the free-edges of composite laminates subjected to external loads, highly concentrated interlaminar stresses could be observed, which might result in premature failure. This work reveals the potential of MSG analysis for solving a generalized free-edge problem, in which composite laminates with general layups and loading conditions including extension, shear, torsion, in-plane and out-of-plane bending, and their combinations can be considered, as well as arbitrary laminate cross section. Within the framework of MSG the composite laminate strip is decoupled into a beam model and a two dimensional cross section of the beam at the microstructural level. To improve the accuracy when shear loads exist, a higher order beam model, referred as a generalized Timoshenko beam model is developed and implemented into SwiftComp. The results from MSG analysis agree very well with the simulation results of three dimensional finite element analysis with detailed microstructural modeling. To expand the usage of the generalized Timoshenko beam model of MSG, beam theory dealing with microstructure with span wise heterogeneity is also developed and implemented into SwiftComp.

The capability of MSG to predict accurate local fields such as stress and strain ensure its application in the failure analysis of heterogeneous solids and structures. In this work, a new criterion was presented for the strength analysis of heterogeneous beam-like structures in terms of the internal forces and moments. This criterion is based on the generalized Timoshenko beam model of MSG. It can be used to serve as a guidance in the micro-structural design of beam-like structures. To demonstrate the applicability and advantage of the newly proposed criterion it is employed to study the strength of a periodic beam-like structure with span-wise heterogeneity.

1. INTRODUCTION

1.1 Background and Motivation

The wide applications of heterogeneous structures have been seen in mechanical and civil engineering, aerospace, automotive and marine industries, as well as in biomedical and sport products. Heterogeneous structures can be made of various materials, of which a very important category is composites, such as fibre-reinforced polymers, ceramic composites, metal composites, etc. Despite the highly developed computing power of today, it is still too costly to directly use the conventional finite element method (FEM) to model all the details of the composite structures, since it needs refined meshes for composite microstructure and leads to a huge number of degrees of freedom (DOFs) and hence prohibitive computing time. Instead of using direct numerical simulation (DNS), heterogeneous structures are usually simulated using multiscale methods based on their hierarchical nature, that is heterogeneous structures are associated with a variety of length scales. As shown in Fig. 1.1, the length scales considered in this work are: 1) the macroscale in which the whole structure with loading and boundary conditions are defined, 2) the microscale that is associated with the material constituents such as matrix and fibers in fiber-reinforced composite laminate, and 3) the mesoscale, an intermediate scale at which a heterogeneous material can be viewed as an equivalent homogeneous material, for example each layer of a fiber-reinforced laminate or each yarn of a textile composite. Based on the separation of length scales, multiscale methods are developed for the analysis of heterogeneous structures with the advantage of reducing the computational cost with acceptable accuracy. Multiscale methods analyze the original heterogeneous structure by separating it into boundary value problems (BVPs) at different length scales. At the macroscale, the model can be solids, beams, and plates/shells, de-

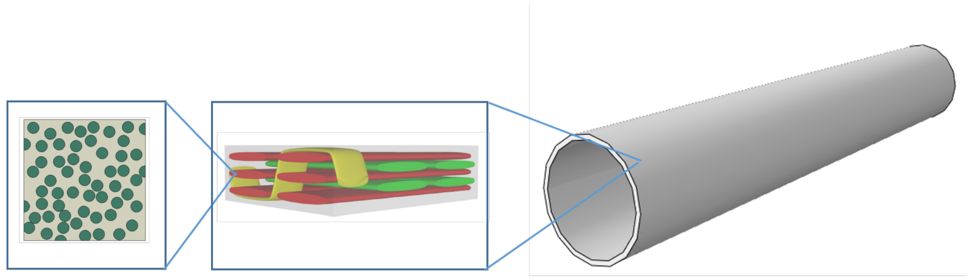

Fig. 1.1. Schematic of multiscale modeling

pending on their spatial characteristics. The constitutive relation of the macroscale model can be obtained from micromechanics analysis, referred as homogenization. In many situations, the prediction of local fields at the level of the microstructure, such as stress, strain, and etc., is very important. To obtain the local fields, a dehomogenization (also referred as recovery or localization) procedure is required. The dehomogenization procedure is usually based on the constitutive relation obtained from the micromechanics analysis. Since the accuracy of the local fields is concerned in this work, multiscale methods involved with analytic micromechanics models that cannot consider the detailed distributions of the micro-scale heterogeneity are beyond the scope of this work.

When the scales are well separated, representative volume elements (RVEs) can be defined for the micromechanics analysis. RVEs are material volumes that are typical of the whole mixture on average and contain a sufficient number of inclusions for the apparent overall properties to be effectively independent of the prescribed boundary conditions [1, 2]. Although this definition is theoretically sound with the assumption of ergodicity, it creates a paradox. On one hand, RVE must include a large number of heterogeneity to be representative, while on the other hand, it must be small enough to be justified as a material point for the macroscopic structural analysis. For periodic materials, the smallest RVE can be the repeating unit cell

(UC). For random materials, RVEs are usually chosen out of practical considerations despite the requirements of a rigorous RVE based on the ergodic principle.

In some cases, the microstructure is quite large compared with the component size and the wavelength of the macroscopic stress field, hence the different length scales cannot be well separated. A typical example is a three dimensional (3D) interlock woven composite plate with only a few plies stacked in the thickness direction. In most of the studies, only a single UC is taken for the micromechanics analysis to obtain the effective material properties with periodic boundary conditions (PBCs) applied. Since the UC is not small enough compared with the whole heterogeneous structure, the local fields recovered will not be very accurate. This is because the PBCs imposed cannot well represent the actual boundary conditions, consequently introducing unfavorable extra constraints.

Another problem is the edge effect. At the boundary of periodic heterogeneous structures, local fields recovered from UC analysis are not accurate because the PBCs are not realistic at the body boundary. Therefore the local fields at the boundary need to be corrected by taking into account of the edge effect. Among this type of problem, free-edge effect have aroused a persistent attention. free-edge effect states that due to a mismatch in elastic properties of adjoining layers of laminates, full-scale 3D and highly concentrated stress fields occur along the free-edges at the interfaces between two dissimilar layers of thermally and/or mechanically loaded laminates. The stress fields are usually localized within the boundary region and exhibit steep stress gradients with a rapid decaying behavior towards the inner laminate region. Such localized fields can result in destructive premature failures in the laminates due to delamination, transverse cracking, etc. This is due to the fact that the interlaminar material strengths are usually much weaker than other parts of the laminates [3, 4]. Thus it is important to obtain accurate 3D stress fields near the free-edge for the optimum design and prevention of premature failure of composite laminates.

Both problems mentioned above can be viewed as resulted from the boundary effect in the dehomogenization procedure. These type of problems are widely investigated, either using general multiscale approaches, or focusing on specific problems.

Multiscale approaches can be generally categorized into sequential (or hierarchical), concurrent, and semi-concurrent methods. By sequential methods, the constitutive relations are pre-computed based on a representative volume element (RVE) and stored in a form such as parameters of constitutive equations, a database etc. The sequential methods are very efficient, but suffer from the defects that they cannot provide a relation between evolving micro-scale local fields and the macroscale behavior.

In semi-concurrent methods, the micro-scale model response is calculated at each material point of the macroscale model and passed to the macroscale model at each load increment during the simulation. Compared to the sequential method, all the complexity of the local microstructures is allowed to be kept during the analysis of the structural components. Therefore, it is also referred as integrated multiscale procedure [5]. The macro length scale and the micro length scale are weakly coupled, because the equilibrium and compatibility across the interface between the macro model and the micro model are not exactly satisfied and the DOFs of the kinetic and kinematic variables passed between the macroscale and micro-scale is much lower than the degrees-of-freedom of the micro model [6]. Therefore, the semi-concurrent methods sometimes are also viewed as sequential methods. The difference between these two types of methods is that the constitutive model in semi-concurrent methods is computed during the simulation, i.e. on-the-fly.

Several methods can be categorized into semi-concurrent method, such as Transformation Field Analysis (TFA) [7, 8], the method of cells (MOC) [9], the Mathematical Homogenization Theory (MHT) [10–13], and the FE^2 methods [14, 15], etc. In these methods, the local fields at the micro-scale can be recovered. However, at the boundary the accuracy will be significantly decreased due to the week coupling of the two scales. In order to deal with the boundary effect, special treatment must be introduced.

The TFA method [7, 8] discretizes the RVE into finite sub-volumes to compute the stress-concentration tensor and the transformation influence factors to provide the micro/macro couplings. To address the boundary effct, different solutions are proposed. For example, Dumontet introduced a boundary layer field, Buannic and Cartraud [16] proposed additional specific boundary conditions, and Kruch [17] introduced spatially decaying stress localization functions near the boundary.

MOC [9] includes the generalized method of cells (GMC) and the high fidelity method of cells (HFGMC). This type of methods employ cuboid subcells to discretize the UC. Traction and displacement continuity conditions are imposed in an averaged sense between the subcells on the UC boundary, along with periodic constraints, to calculate the constitutive relations of the material. Thus errors can be introduced due to the inaccurate description of the microstructure and the averaging scheme adopted for the local fields. The local fields computed has been shown not as accurate as the 3D RVE analysis [18]. This drawback originated from the inaccurate description of the microstructure is also shared with the TFA methods.

MHT is developed on the strict mathematical basis of the formal asymptotic method through a two-scale formulation. MHT was first proposed by Bensoussan [10] for heterogeneous materials with periodic structural characteristics, and has been implemented using FEM by many researchers [11–13]. When the scale is not well separated, second-order terms in the expansion of displacement can be kept for higher accuracy of local fields [10, 13]. However, this method still cannot provide accurate solution at the boundary. Although MHT was originally developed for periodic media formed by UCs, it can be applied to RVE because for heterogeneous materials the assumption of locally statistical periodicity must stand for it to be replaced with an effective homogeneous material in the macroscopic structural analysis. Using MHT, PBCs must be applied. It allows the direct coupling of finite element models on the macro and the micro scales, but usually requires special codes for specific problems.

FE^2 methods [14, 15] implement a finite element based RVE analysis at each integration point of the macroscopic finite element model. FE^2 methods have been implemented to treat the second-order continua for better local fields when the scales are not well separated. However this solution is not a remedy for the boundary effect [5].

In concurrent models [6, 19–23] the fine-scale is strongly coupled with the coarse-scale. Concurrent methods directly insert the microstructure details into the homogenized model by enforcing the equilibrium (or momentum balance in the case of dynamics) and compatibility across the interface between the macro model and the micro model. It solves the micro and macro models simultaneously [6]. The transitional elements or well-defined kinematic relations are defined at the interface to relate the regions of varying element size or types. Although concurrent methods are more efficient compared with direct numerical simulation (DNS), this method is still computational expensive and complicated to implement, because strong coupling between the scales is dealt with adaptive re-meshing algorithms and modified transitional elements. Parallel computing usually are recommended for structure analysis using this method.

To solve the boundary effect problems mentioned previously, usually specific methods are developed respectively, which will be reviewed in later sections of this chapter. From the discussion, it is obvious that currently an general and efficient solution for these problems are not available. In this work, the problems are found to be solved by extending a newly developed theory, the Mechanics of Structure Genome (MSG) [24]. MSG is developed based on the variational asymptotic method (VAM). It provides a unified theory for multiscale constitutive modeling of composites based on the concept of Structure Genome (SG). Generalized from the concept of representative volume element (RVE), a SG is defined as the smallest mathematical building block of a structure. Geometrical nonlinearity is systematically captured for Cauchy continuum, beams and plates/shells using a unified formulation [24]. Using this method, a sequential implementation of the method is sufficient. In addition, no special treatment for the boundary effect is needed.

To be clear, in this work, the following two problems due to the ambiguous separation of the length scales are investigated.

1. Derive the micromechanics model with least information loss for heterogeneous 3D structures where the micro and macro scales are not well separated and the periodicity condition is not maintained in some directions. In the case where the periodicity is not kept in all the directions, the 3D heterogeneous structures is referred as 'aperiodic'.

2. The free-edge stress analysis of general composite laminates with general layups and subject to general loads such as tension, shear forces, bending moments and torques.

This work will be arranged as follows. Chapter 1 introduces the background and motivation of this study, as well as a review of related works in literature. In Chapter 2, a very brief introduction of MSG is given. Chapter 3 addresses the first problem by extending the MSG theory to aperiodic heterogeneous solids. Chapter 4 tackles the generalized free-edge stress analysis by implementing the MSG theory for beams. As a more general case, MSG based Timoshenko beam model is implemented into the general-purpose computer code SwiftComp for both homogenization and dehomogenization. In Chapter 5, a strength analysis based on the local fields obtained from the MSG dehomogenization is given for beam-like structures composed of spanwise heterogeneous SGs. Finally, a summary will be given in Chapter 6.

1.2 Literature Review

In this section special methods are reviewed separately for the two problems concerned in this work. First, for microscale analysis of heterogeneous materials, the basics of RVE analysis are first summarized. Then the special methods dealing with textile composites are reviewed as an important and typical problem for the case that length scale is not well separated. In the second part of this section, as a special case of boundary effect, free-edge stress analysis is reviewed. At last, the failure analysis of composite materials is briefly reviewed.

1.2.1 Modeling of 3D Heterogeneous Solids

In RVE analysis, boundary conditions and the selection of the RVE are two main concerns. To obtain the effective properties of heterogeneous materials, specific boundary conditions must be prescribed on the RVE. According to Hill [1], if the material is not periodic, the effective properties obtained from RVE must be independent of the boundary conditions prescribed. However the selected analysis domain in most cases has been based on volume elements that are know smaller than the RVE. The main reasons are limits in the size of models that can be handled and difficulties in providing suitable RVEs for actual materials such as porous materials [25]. In this situation the term 'apparent properties' is used instead of 'effective properties', and the analysis domain can be a 'window' [26] or statistical volume elements (SVEs) [27].

The boundary conditions we can apply to an RVE is usually governed by the Hill-Mandel macrohomogeneity condition [1] so that the homogenized material is energetically equivalent to the original heterogeneous material. Hill-Mandel macrohomogeneity condition is generalized by Hazanov in [28] for arbitrary materials, in particular for nonlinear inelastic composites with imperfect interfaces. De Souza Neto et al. proposed a generalized unified micromechnics theory [29], in which the Hill-Mandel macrohomogeneity condition is rephrased as a variational statement by requiring the total macroscale virtual power to coincide with the volume average of its micro-scale counterpart. This requirement is named as the principle of multiscale virtual power. Various problems such as dynamics, high order strain effects, material failure can be addressed with this new principle.

Hill-Mandel macrohomogeneity condition can be written as

$$\langle\langle \sigma_{ij}\epsilon_{ij} \rangle\rangle = \bar{\sigma}_{ij}\bar{\epsilon}_{ij} \tag{1.1}$$

where angle brackets denote the volume average over the RVE and

$$\bar{\sigma}_{ij} = \langle\langle \sigma_{ij} \rangle\rangle \qquad \bar{\epsilon}_{ij} = \langle\langle \epsilon_{ij} \rangle\rangle \tag{1.2}$$

This condition means that the average of the product of the stress σ_{ij} and strain ϵ_{ij} at the micro level equals the product of their averages at the macro level. For materials without cavities and with perfect bonded interfaces among constituents, the Hill-Mandel macrohomogeneity condition can be written in the form of

$$\langle\langle \sigma_{ij}\epsilon_{ij} \rangle\rangle - \bar{\sigma}_{ij}\bar{\epsilon}_{ij} = \frac{1}{\Omega}\oint_{\partial\Omega} n_k \left(\sigma_{ik} - \bar{\sigma}_{ik}\right)\left(u_i - y_j\bar{\epsilon}_{ij}\right) d\Omega = 0 \tag{1.3}$$

where u_i is displacement at the micro level, Ω denotes the volume of the RVE and $\partial\Omega$ is the boundary of the RVE, y_j denotes the micro coordinates, and n_k is the outward normal of the boundary. $i, j, k = 1, 3$.

The most commonly used boundary conditions satisfying the Hill-Mandel macrohomogeneity condition are:

1. kinematically uniform boundary conditions (KUBCs), also known as uniform displacement boundary condition or Dirichlet boundary condition:

$$u_i = \epsilon^0_{ij} y_j \quad \forall \boldsymbol{y} \in \partial\Omega \tag{1.4}$$

with ϵ^0_{ij} being constant along the boundary.

2. statically uniform boundary conditions (SUBCs), also known as uniform traction boundary condition or Neumann boundary condition:

$$t_i = \sigma^0_{ij} n_j \quad \forall \boldsymbol{y} \in \partial\Omega \tag{1.5}$$

with t_i denoting the traction on the RVE boundary and σ^0_{ij} being constant along the boundary.

3. PBCs

$$t^+_i = -t^-_i \qquad u^+_i - u^-_i = d_j\epsilon^0_{ij} \quad \forall \boldsymbol{y} \in \partial\Omega \tag{1.6}$$

where u^+_i and u^-_i denoting the displacements at the RVE boundary surfaces and superscripts '+' and '−' denote the normal direction of the corresponding surface in the coordinate system. ϵ_{ij}^0 denotes the given strain load case and d_j is the RVE dimension in the y_j direction.

4. mixed uniform boundary conditions (MUBCs), also called orthogonal mixed boundary conditions, uniform displacement-traction boundary condition.

$$(t_i - \sigma_{ij}^0 n_j)(u_i - \epsilon_{ij}^0 y_j) = 0 \quad \forall \boldsymbol{y} \in \partial\Omega \tag{1.7}$$

In the case of MUBCs, different combinations of a priori prescribed boundary conditions are possible but have to fulfill the condition in Eq. (1.7). Each of these mixed boundary conditions yields different apparent properties if the minimum size of RVE is not reached. MUBCs can only be applied to rectangular cuboid volume elements that have at least orthotropic effective properties. Only when these requirements are satisfied, the volume averaged normal stress components are uncoupled with the volume averaged shear stress, and thus the Hill-Mandel condition can be satisfied [30]. Since only under the chosen MUBCs the Hill-Mandel condition is satisfied, MUBCs cannot be applied to nonlinear regime for dehomogenization as the superposition principle no longer holds [31]. Within the MUBCs category, Pahr and Zysset [32] proposed periodicity compatible mixed uniform boundary conditions (PCMUBCs). This type of MUBCs is so named because when applying PCMUBCs to UC of orthotropic effective behavior, the UC will deform in a pattern closing to periodic configuration, and predict very close effective properties as does PBCs. Using PCMUBCs can avoid prescribing nonzero tractions on the boundary surfaces, which is especially attractive for cellular materials.

Mesarovic et al. [33, 34] proposed minimal kinematic boundary conditions (MKBCs) with linearized kinematics for simulations of disordered microstructures based on Cauchy continuum. It has later been proved that the first-order homogenization schemes based on the MKBCs predicts uniform traction on the boundary of RVE if no body force is included [34].

A number of literature worked on choosing RVE and the boundary conditions and some general conclusions can be summarized as follows:

1. The effective elastic moduli obtained from a RVE analysis are bounded by the average apparent responses of finite size domains under KUBCs and SUBCs [35]. As the domain size increases, the two bounds converge to the effective properties [36–39].

2. The convergence of the two bounds is influenced by the contrast of the material properties of the constituents, and the higher the contrast between the moduli of matrix and inclusions, the slower the convergence [26, 37, 40, 41].

3. For periodic microstructures, a single UC using PBCs will predict effective properties. For random microstructures, while KUBCs and SUBCs on small domains result in large, oppositely biased errors from the effective property, PBCs give a smaller error for the same window size [42].

4. With the same analysis domain, the apparent properties predicted using any type of MUBCs will lie between the bounds of using KUBCs and SUBCs for finite elasticity [43].

In the practical sense, KUBCs and SUBCs are fairly easy to prescribe in a finite element (FE) codes. It is noted that SUBCs cannot be applied to porous materials because the strain average $\bar{\epsilon}_{ij}$ cannot be calculated when the volume elements have cavities intersect the boundaries and are not discretized [30, 31].

From the previously mentioned conclusions, PBCs are most efficient in terms of convergence rate. The standard way of implementing PBCs requires identical meshes on opposite RVE boundaries, which cannot always be guaranteed, leading to a non-periodic mesh. In [44] a weak enforcement of PBCs are applied by independent FE-discretization of boundary tractions, which allows for a parameterized transition between the strongest form (PBCs) to the weakest form (SUBCs). In [45], the displacement field of two opposite RVE sides is interpolated by linear combinations of shape functions such as Lagrange shape functions or Hermite shape functions. [46] used surface-to-surface constraints in ABAQUS to apply PBC approximately. [47] developed a method to apply PBCs allowing multiple-parts meshes in the in-house developed ORAS software. All of these methods require special treatment on the nodes at the RVE boundaries.

Nowadays, textile composites are often used in important structural applications due to their exceptional mechanical properties. In order to fully exploit the advantages of fabrics, the accuracy of the modeling approaches in predicting effective stiffness and strength is very important. The existing methods can be classified into analytic methods and numerical methods. Analytic methods [48–51] allow for efficient and reasonably accurate predictions of the stiffness but the prediction of strength values is not accurate in most cases. In contrast, numerical methods are usually based on 3D continuum elements and thus computationally more expensive, however, they allow for accurate stress recovery which is important in the failure prediction. When using numerical methods in textile composites, many of them choose a UC as the analysis domain postulated that the UC is far away from the boundaries both in the plane and in the thickness directions of the composites.

However, textile composites are usually applied with only a few layers stacked in the thickness direction. It is apparent that the periodicity in the thickness direction is lost since the UC cannot be treated as a material point in the whole structure. In addition, the inter-ply shift between the neighboring layers from manufacturing also exerts influence to the mechanical behavior of the textile composites. These phenomenon have been demonstrated both experimentally and numerically [52, 53].

To account for these factors, [53, 54] developed novel boundary conditions on a single UC which mimic the constraint applied by adjacent layers. These boundary conditions account for the distinction of different positions of the ply within the laminate, arbitrary inter-ply shifts and user-defined numbers of layers. The novel boundary conditions are applied by a weighted average of displacement solution from UC analysis in regard to inter-ply shifts and displacement solutions using traction-free boundary conditions in the out-of plane direction. To obtain the effective properties, first UC analysis should be carried out to obtain the displacement as basis functions and then an optimal problem need to be solved to ensure energy equivalence of the original heterogeneous material and the homogenized material. [55, 56] used shell elements to represent yarns and matrix of each ply in 3D woven composites to reduce the computational cost compared with continuum element modeling. A concept of UC is also used in the method, and six different loading cases are required to obtain the A, B, D matrices of the woven composite shell. Both these two methods are developed specifically for textile composite which involve a lot of ad doc assumptions.

Espadas-Escalante considered the finite thickness effect of textile composites and simulated the exact number of layers using PBCs in the in-plane directions and SUBCs in the thickness direction [57]. The surface strain field using the mixed boundary conditions is shown to have better correspondence than using PBCs compared with experimental result.

1.2.2 Modeling of Free-edge Effect

Increasing use of composite laminates in the last several decades has stimulated intensive research efforts in many new problems encountered in the engineering application. Among the problems, free-edge effect has aroused a persistent attention.

Although the free-edge effect is known in 1970s, no analytical solution satisfying the 3D elasticity governing equations along with all the free-edge boundary conditions and interlaminar continuity conditions is known due to the inherent complexities involved in the problem. Detailed reviews on the methods proposed for determining the free-edge stress fields have been presented in [58, 59].

To simplify the original 3D free-edge problem, a considerable number of approaches have been developed based on quasi-3D (Q3D) models or reduced 2D plate models, while a few numerical methods attempted 3D solutions directly.

Approaches relied on Q3D models are concerned with a long rectangular composite laminate. These approaches adopt a hypothesis of zero gradients along the axial coordinate x and retain an axial warping of the cross sections which depends only on y and z (axis notation according to Fig. 1.2. Most of the analytical approaches and several numerical methods [60–62] lie in this class. Since a generalized plane deformation state [63] must be satisfied by applying the Q3D model, many methods only work for special classes of laminate layups or load cases, thus are often restricted to some limited applications. Only a few studies have been devoted to study the interlaminar stresses due to combined loads in general layups. Pipes and Pagano

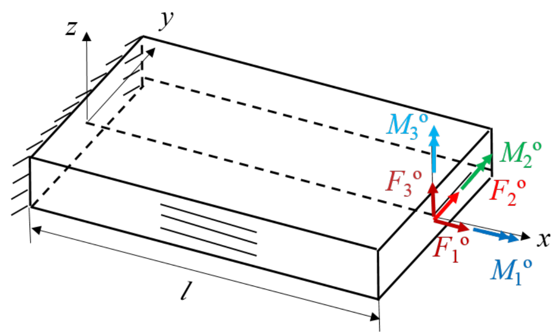

(a)

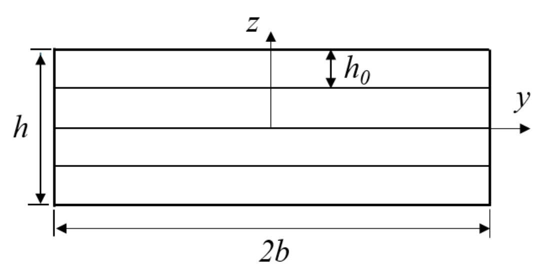

(b)

Fig. 1.2. The laminate geometry and coordinate system.

developed an approximate elasticity solutions for symmetric and balanced angle-ply composite laminates subjected to uniaxial extension in 1974 [3]. This approach was later extended to loading conditions of uniform temperature change and anticlastic bending by Pipes and Goodsell [64–66]. Early works of analytic approaches include perturbation technique by Hsu and Herakovich [67], the boundary layer theory by Tang and Levy [68], etc.

Displacement-based equivalent single-layer (ESL) theories are developed by Pagano [69], Becker [70, 71], Murty and Kumar [72]. Tahani and Nosier [73, 74] studied cross-ply laminates under extension and thermal loading using layer-wise (LW) theories. Based on the reduced elasticity displacement field of a long laminated composite plate, Nosier and Bahrami [75, 76] studied interlaminar stresses in antisymmetric angle-ply laminates under extension and torsion. Nosier and Maleki [77] used a LW theory and an improved first-order shear deformation theory (FSDT) for analyzing free-edge stresses in general composite laminates subjected to extension loads. Sarvestani and Sarvestani [78] later generalized the solution to obtain interlaminar stress as in general composite laminates subjected to extension, torsion, and bending moment.

Employing stress based LW theories, Kassapoglou and Lagace [79] developed force-balance method using the principle of minimum complementary energy to assess the free-edge stress fields in symmetric laminated plates under uniaxial extension. A large amount of developments devoted to free-edge stresses analysis have been formulated based on this procedure, of which Lin [80] introduced bending and torsion into force-balance method for general laminates. Yin [81, 82] implemented Lekhnitskii's stress functions [63] and investigated laminates with arbitrary layups under uniaxial extension, bending and torsion. Kim and Atluri [83, 84] also investigated interlaminar response for cross-ply and angle-ply laminates under uniform thermal loading and mechanical loads. Cho and Kim [85] used an iterative method applied to analyze free-edge interlaminar stresses of composite laminates which are subject to extension, bending, twisting and thermal loads. The stresses, which satisfy the traction-free conditions not only at the free-edges but also at the top and bottom surfaces of laminates, are obtained by using the complementary virtual work and the extended Kantorovich method.

Tahani and Andakhshideh [86, 87] developed an analytical method based on a 3D multi-term extended Kantorovich method to calculate interlaminar stresses in thick rectangular composite laminated plates with arbitrary laminations and general boundary conditions subjected to lateral loads. In 2016, Dhanesh and Kapuria [88] developed mixed-field multiterm extended Kantorovich method to solve free-edge problem for symmetrical and antisymmetrical laminates subjected to uniform extension, bending, twisting and thermal loading, which can satisfy all the boundary conditions and the interfacial continuity conditions exactly at all points.

FEM are usually implemented in 2D plate models to solve free-edge problem of laminates. The 2D plate models include displacement-based ESL theories, displacement-based LW theories, stress-based ESL theories and stress-based LW theories, which are reviewed by Carrera [89]. Using 2D theories to study the free-edge effects does not exert restriction on the laminate layups and loads applied. However, in 2D plate theories the through-thickness distributions of the displacement or stress are assumed a priori, the boundary conditions at the free-edge are generally satisfied in an integral sense, which can have adverse effects on the accuracy of the solution. D'Ottavio and his colleges [90, 91] assessed various plate theories in Carrera's unified formulaton for free-edge problems and found that only high-order LW models (fourth order in their study), either displacement-based or stress-based, can provide results that compare well with full 3D finite element analysis (FEA). It is known that high-order LW models require long computing time similar as 3D FEA. Recently, Vidal [92] developed a method which solve the free-edge problem by an iterative process consisting of solving a 2D plate problem and a 1D problem in the thickness direction successively at each iteration. In the thickness direction, a fourth-order expansion in each layer is considered.

The numerical methods directly solving the 3D free-edge problem usually focused on generation of new and efficient meshing approaches [93], developing special purpose element for dealing with the singular stress field [94, 95]. A multi-particle finite element is utilized by Nguyen and Caron [95] which is applied for general laminates and is shown to be capable of simultaneously predicting global and local responses.

1.2.3 Modeling of Composite Failure

Similar to conventional homogeneous and isotropic materials like bulk metals and ceramics, the prediction of damage initiation and evolution, and post failure behaviors of composite material is crucial to its applications in advanced structures. However, due to its inherent anisotropy, coupling between different deformation modes, and the microstructural heterogeneity, an accurate assessment of its failure is much complicated and challenging. Since the wide application of composite materials in advanced engineering structures in aerospace, automobile, and other industries that require the highest safety standard, it is not surprising that numerous researches have been conducted in this field.

Among these, probably the simplest and easiest-to-use ones are the so-called generalized failure criteria which treat the composite as a homogenized anisotropic material and incorporate into a polynomial expression the different failure mechanisms [96]. Belonging to this category are the maximum stress, maximum strain [97], Tsai-Hill [98], and Tsai-Wu [99] theories. Maximum stress and maximum strain criteria are limit or non-interactive theories, in the sense that failure is judged based on individual stress or strain component compared to its ultimate failure value, while Tsai-Hill and Tsai-Wu are interactive criteria. The applicability and performance of these criteria can be assessed by means of failure envelopes. Daniel [100] calculated the failure envelopes of the above failure criteria for two biaxial stress states, i.e. (σ_1, σ_2) and (σ_2, τ_{12}), for unidirectional carbon/epoxy composite. The failure envelopes show quasi-elliptical shapes for the interactive theories, whereas rectangular or parallelogram shapes for the non-interactive theories. Sun [101] and Pipes and Cole [102] compared the off-axis tensile strength predictions of the various theories with experimental data for boron/epoxy laminae. Their studies reveal that the interactive criteria predictions agree well with the experimental results, while the limit theories show obvious deviations, especially around the off-axis angle of the transition from shear to transverse tension failure modes. A more comprehensive evaluation of these theories are given in Sun [101] and Swanson et al. [103] by the comparisons of theoretical predictions of the failure envelope in biaxial stress state with experimental data for carbon/epoxy lamina. Their results show that in the region of transverse normal tension all of the interactive criteria predictions match well with the experimental data, while in the region of transverse normal compression only Tsai-Wu theory leads to a relatively good agreement. Other interactive theories do not capture well the higher shear strength due to the compressive transverse normal stress.

The above failure theories do not separately take into consideration the different microstructural failure modes, such as fiber breaking, matrix cracking, fiber kinking/buckling, fiber/matrix debonding, etc. Instead, the microstructurally heterogeneous composite materials are treated as macroscopically homogeneous and anisotropic continua. A failure mode based theory was proposed by Hashin and Rotem [104] in which the failure mechanisms of fiber and matrix are separated and a quadratic interaction are assumed between the stress components. This theory was extended in Hashin [105] to distinguish the tensile and compressive failure modes. The beneficial effect of the transverse normal compression on the shear strength was considered in Sun et al. [106] by a modification of Hashins theory. As observed in Bailey et al. [107] and Flaggs and Kural [108], the transverse strength of laminates, i.e. the in-situ transverse strength, usually is much higher than that measured for unidirectional reinforced lamina. Sun and Tao [109] employs the in-situ transverse strength in Hashins theory to predict the failure envelopes of unidirectional and multidirectional laminates. In the theory developed by Puck [110–114] the fiber failure under a combined stress state is assumed to happen at the same fiber stress at failure under uniaxial tensile or compressive load. A correction factor is employed to account for the effect of different moduli of the fiber and matrix on the fiber strain under biaxial stress state. Puck and Schrmann [114] incorporated into the matrix fracture Mohr's hypothesis that failure is exclusively determined by the stress acting on the fracture plane. Consequently, the application of Pucks criterion needs the transformation of the stresses into a local coordinate system attached to the fracture plane, the angle of which needs to be calculated by a numerical procedure. The experimental observation that compressive stress normal to the fracture plane impedes shear fracture is accounted for in the theory. Mayes and Hansen [115] proposes a multi-continuum failure criterion, where instead of the homogenized stress of the composites phase-averaged constituent stress and strain fields are used. As in Hashin's theory, the stress invariants under the transversely isotropic symmetry group are used to formulate a quadratic polynomial interactive failure criterion separately for each constituent. Davila et al. [116] developed a criterion incorporating the ideas of Hashin and Puck in different failure modes. Matrix failure under transverse compression is characterized by the stress state on the fracture plane that calculated by maximizing the Mohr-Coulomb effective stresses. Fiber misalignment and matrix failure criterion in the local coordinate system of the misalignment are employed to predict fiber kinking. Ha [117] proposed a failure theory based on micro-stresses of the constituents and at the fiber-matrix interface which are computed by using UCs of square or hexagonal arrays. In addition to the matrix and fiber failure, a fiber-matrix interface failure criterion is also given. The strengths for the matrix and the interface are determined by comparing the micro-stresses of the constituents with the macroscopic matrix tensile and compressive strengths.

The failure theories cited above are usually used as criteria for the initiation of damage in the composite material. After the initiation of failure, the composite material frequently still has sufficient residual strength to carry considerable external loads. The damage process from its initiation to the ultimate failure is usually simulated either by a progressive damage model, where the material properties are gradually degraded, or by the fracture mechanics based techniques like virtual crack closure technique (VCCT), see Tay et al. [118]. Probably the simplest and conservative property degradation method is the ply discount method, where the affected stiffness of a failed laminae is completely discounted, see Pal and Ray [119]. In Sun and Tao [109], the longitudinal modulus is discounted to zero when fiber breakage occurs, while the transverse and shear moduli are reduced to zero when the matrix cracking is observed. The complete ply-discount methods are plausible in laminated composite because of the loading-carry ability of other intact laminae. Within the framework of the finite element method, instead of completely discounting the whole lamina when a failure mode is detected, a more realistic strategy is to completely discount the properties of the failed element, see Hwang and Sun [120] and Tolson and Zabaras [121]. However, an issue with this approach is that it neglects the effect of the size of the element. A remedy is proposed by Reddy et al. [122] where a stiffness reduction coefficient is introduced to gradually reduce the stiffness of the failed element. In this approach, after failure initiation the stiffness of the element will be gradually reduced, depending on the extent of damage. Consequently, repeated failure of the same element is allowed until it is unloaded sufficiently when the failure criteria are no longer satisfied. More sophisticated schemes of property degradation are developed by employing the idea of continuum damage mechanics (CMD) [123–129]. In the damage model proposed by Matzenmiller et al. [123] an elastic response is assumed before the damage initiation. The failure theory in Hashin and Rotem [104] is used as the criterion for failure initiation. Five damage variables are introduced to account for the gradual property degradation for different failure modes. The evolution of the damage variables is formulated by a multi-surface dissipation potential. Each damage mode and their interactions are captured by individual surface which is formulated in the space of the thermodynamic forces. Maim et al. [125] proposed a model where the damage activation is based on the criteria developed in Davila et al. [116]. The property degradation is characterized by the evolution of five damage variables which is expressed as a set of exponential functions of the damage thresholds. The requirement of non-negative energy dissipation is trivially satisfied by the restriction of monotonically increasing damage variables, as a result of the specific Gibbs free energy assumed. Mesh-dependency in finite element simulation could be observed for strain-softening materials where strain localization happens because of unloading of the surrounding material points, see Lapczyk and Hurtado [128]. To alleviate the mesh-dependency the idea of crack band proposed in Bažant and Oh [130] is employed where a characteristic element length is introduced. Assuming that the damage variable corresponding to shear is solely determined by those associated with other failure modes, Lapczyk and Hurtado [128] proposed a model with four independent damage variables. The boundary of the elastic domain is characterized by the failure surfaces based on the criteria in Hashin [105]. Mesh-dependency is alleviated noticeably by a characteristic length at the material point which simply equals to the square root of the area associated with this point. Equivalent displacements for each failure modes are defined based on the characteristics length to formulate the evolution of damage variables. The ultimate failure for each mode is achieved when the current equivalent displacement reaches its final value which is a material property determined by the fracture energy of the corresponding failure mode. Numerical convergence difficulties in implicit finite element implementation due to strain-softening are mitigated based on the viscous regularization of the damage variables [131, 132].

2. MECHANICS OF STRUCTURE GENOME

2.1 Introduction

MSG is a unified multiscale method that decouples the original heterogeneous structure into a macroscopic structural analysis and a constitutive modeling over SG. Depending on the spatial characteristic of the original heterogeneous structure, the macroscopic structure model can be classified into 3D solid, 1D beam or 2D plate/shell. This chapter gives a brief introduction to the MSG and SG, which closely follows the presentation in Yu [24, 133]. The connection and difference between SG and RVE are explained. In the last section, the extension of MSG in this work is introduced.

The formulation of MSG starts with expressing the kinematics of the original heterogeneous structure u_i, ϵ_{ij} in terms of those of the macroscopic structure model $\bar{u}_i$, $\bar{\epsilon}_{ij}$ and fluctuating functions w_i. Note for heterogeneous solid, $\bar{\epsilon}_{ij}$ are the macro strain of the equivalent homogeneous solid, while for heterogeneous beam or plate/shell like structures, $\bar{\epsilon}_{ij}$ denotes the macroscopic strains and curvatures of beams or plates/shells. Proper constraints are introduced to ensure unique mapping between the deformation state of the original model and the macroscopic model. Then the governing statement of the original heterogeneous structures Π, such as the principle of minimum potential energy for linear elastic behavior, can be expressed in terms of the kinematics of the macroscopic model, i.e. $\bar{\epsilon}_{ij}$ and the w_i which is a function of $\bar{\epsilon}_{ij}$. Then the control functional can be obtained based on the principle of minimum information loss (PMIL) [134] that states the difference between the governing statement of the original model and the homogenized macroscopic structure model should be minimized. VAM [135] is implemented to simplify the control functional. In this way, the governing statement of the original model can be simplified to a macroscopic structure model and a constitutive model on SG that is the smallest mathematical building block of the original structure. It is seen from the formulation procedure, the structural model and the SG analysis are formulated simultaneously based on the PMIL and VAM, which ensured the accuracy of the this method.

As the macroscopic structural model is formulated as a general continuum of 3D solid, 1D beam or 2D plate/shell, the structural analysis can be conducted using the solid elements, beam elements or plate/shell elements in commercial FEA softwares such as ABAQUS, ANSYS, etc., or other analysis methods.

The SG analysis contains two parts. First, through homogenization, the constitutive model of the macroscopic structure is obtained, as well as the dehomogenization relations, which is the relation between the fluctuating functions w_i and $\bar{\epsilon}_{ij}$. Second, dehomogenization can also be carried out to obtain the local fields within the microstructure using the macroscopic displacements and strains from the structural analysis and the dehomogenization relations. Therefore, the SG analysis bridges the macroscopic structural analysis and the microstructure directly. The constitutive modeling over SG, also referred as SG analysis, has been implemented into a Fortran code called Swiftcomp.

Fig. 2.1 shows the framework of a MSG multiscale analysis. The first step is to identify the SG considering from two aspects: first from the spacial characteristic of original structure to determine whether it should be modelled as a solid, a beam or a plate/shell; then based on the macroscopic model and the heterogeneity feature of the microstructure to find the SG. This is discussed in detail in the next section. Once the SG has been identified, a constitutive modeling can be performed over SG, from which the effective constitutive model for structural analysis can be obtained as well as the dehomogenization relations. This step is also called homogenization. Then the macroscopic structural analysis can be carried out using any tool that can deal with traditional structural analysis, for example analytic method or commercial FEA softwares. Then utilizing dehomogenization relations from the constitutive modeling, the local fields in the original heterogeneous structure can be obtained with the global structural behavior.

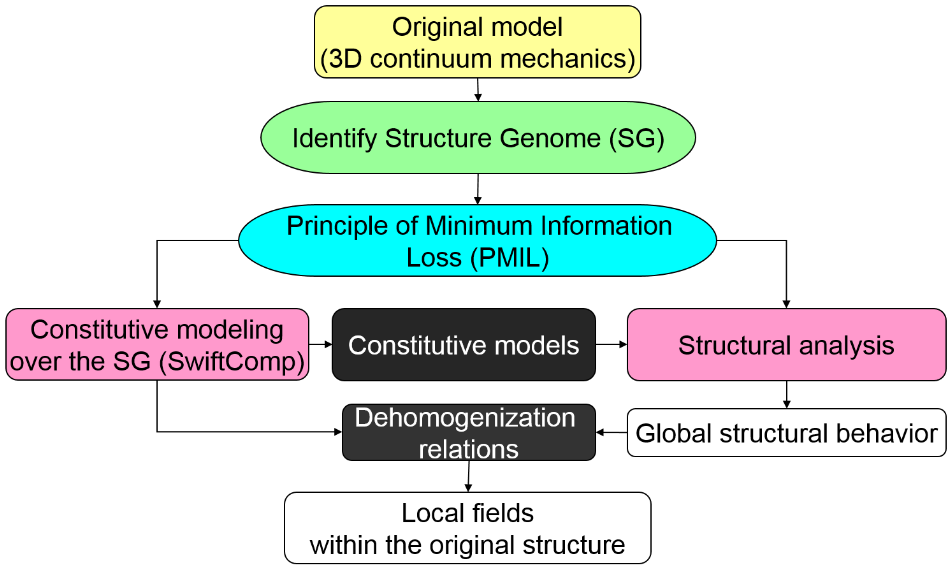

Fig. 2.1. The framework of a MSG multiscale analysis [136]

2.2 SG for 3D Solid Structures

For 3D structures, SG generalizes from the RVE concept with two fundamental differences. First, the dimension of the SG can be 1D, 2D or 3D based on the heterogeneity of the material microstructure as shown in Fig. 2.2. For a binary composites made of two alternating layers, the entire structure can be constructed by repeating a straight line with two segments in 3 directions of the Cartesian coordinate system, in which each segment containing the thickness and the material properties of a layer. Consequently, this straight line can be used as the SG to homogenize the composite laminates to be an equivalent solid. In the same fashion, for composite structures such as continuous unidirectional fiber reinforced composites, the heterogeneity is characterized by 2D building units. Hence, the SG could be modeled as a 2D domain. For

3D heterogeneous structures such as particle reinforced composites, a 3D volume is needed to build the SG.

Even though the dimensionality of SGs might be different from that of the original heterogeneous structure, the effective properties and the dehomogenization results obtained from SG analysis are 3D. Taking binary composites with linear elastic behavior as an example, the complete 6×6 stiffness matrix can be obtained from the analysis over the 1D SG. This methodology has the highest efficiency, since the heterogeneity is modeled by the lowest possible dimension. In contrast, in the RVE analysis the properties needed for the macroscopic structural analysis determines the RVE dimension. Taking continuous unidirectional fiber reinforced composites as an example, micromechaincs analyses should be conducted over a 3D RVE if the macroscopic structural analysis requires 3D material properties.

Second, to obtain the 6×6 stiffness matrix using the finite element (FE) based RVE analysis, 6 different boundary conditions in terms of displacements or tractions must be applied. Since the boundary conditions need to be revised in the load cases of the FE model, extra time will be consumed to configure and solve these BVPs of RVE. In addition, in the dehomogenization, for each macro strain $\bar{\epsilon}$ a BVP needs to be solved. This is because the boundary conditions are applied in terms of the 6 different loading cases of strain ϵ_{ij}^0 or stress σ_{ij}^0 as shown in Eqs. (1.4), (1.5), (1.6), (1.7).

In the SG analysis formulation, fluctuating functions w_i are to be solved, and the periodic constraints can be expressed in the form of

$$w_i^+ = -w_i^- \tag{2.1}$$

where w_i^+ and w_i^- denoting the fluctuating fields at the SG boundary surfaces and superscripts '+' and '$-$' denote the normal direction of the corresponding surface in the coordinate system. It is obvious the periodicity constraints are not involved with ϵ_{ij}^0 and can be easily applied by removing the DOFs of w_i^+ using Eq. (2.1). This also will reduce the dehomogenization analysis to be simple algebraic operations. All these merits will make the SG analysis very efficient.

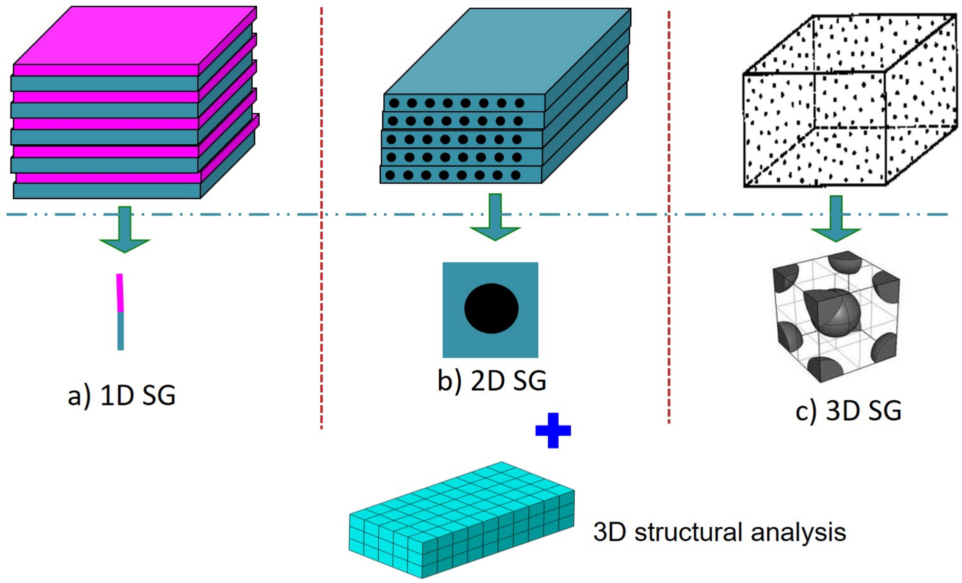

Fig. 2.2. Analysis of 3D structures approximated by a constitutive modeling over the SG and a correspond 3D macroscopic structural analysis [24].

2.3 SG for Dimensionally Reducible Structures

SG also allows a direct connection between the material constituents and the dimensionally reducible structures, i.e. the plate/shell like structures and the beam-like structures. Using MSG, for heterogeneous dimensionally reducible structures with buildup structures as shown in Figs. 2.3 and 2.4, each point in the macroscopic model can be viewed as associated with a microstructure of SG. In this sense, the constitutive modeling over SG can also be treated as an application of micromechanics of structures.

2.3.1 2D Plate-like Structures

A properly chosen SG for plate-like structures can be used to derive the homogenized properties and also dehomogenize the local fields for macrostructural FEA with plate/shell elements. Typical examples of SGs for plate-like structure are shown in

Fig. 2.3. In Fig. 2.3a no in-plane heterogeneities present, so a transverse normal line is chosen as the SG. Each layer of the composites is represented by the corresponding segment in the SG. Heterogeneous panels are shown in Fig. 2.3b and Fig. 2.3c with heterogeneity in one in-plane direction or both of the in-plane directions. Consequently, the corresponding SGs are 2D and 3D, respectively.

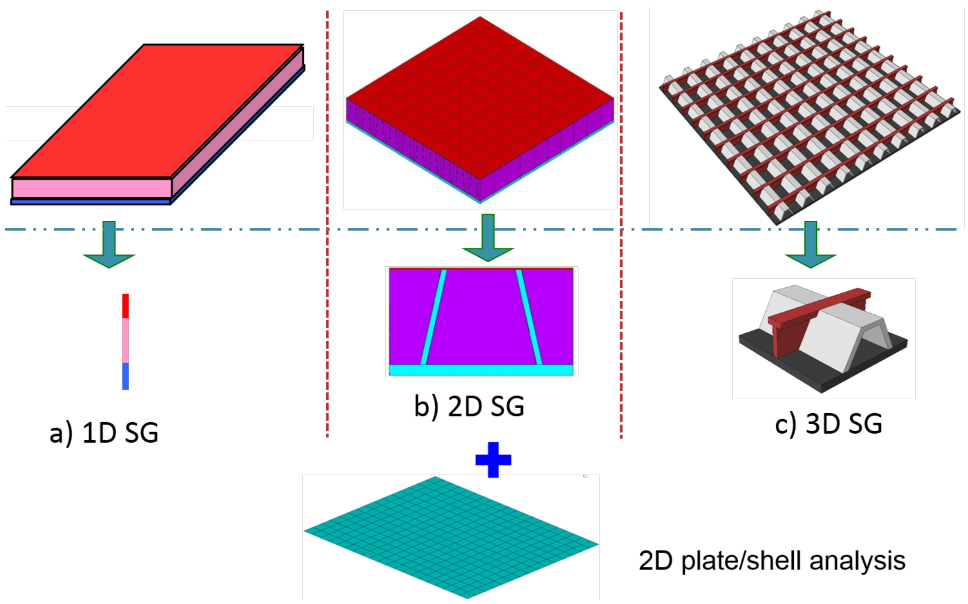

Fig. 2.3. Analysis of plate-like structures approximated by a constitutive modeling over the SG and a corresponding 2D plate analysis [24].

2.3.2 1D Beam-like Structures

Typical examples of SGs for beam-like structures are shown in Fig. 2.4. The airplane wing in Fig. 2.4a has a uniform cross section, so it can be built by sweeping the 2D cross sectional domain along its reference line. The cross section can be consisted of homogeneous materials or composites. Consequently, the 2D cross-sectional domain can be selected as the SG. As in Fig. 2.4b, if heterogeneity presents also in the spanwise direction, to capture its microstructural details, a 3D SG is necessary.

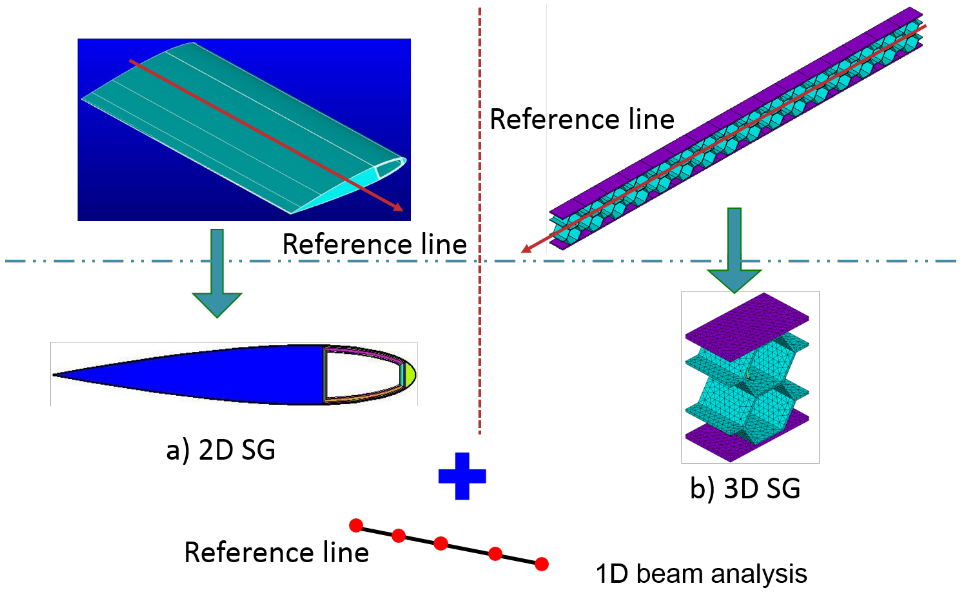

Fig. 2.4. Analysis of beam-like structures approximated by a constitutive modeling over SG and a corresponding 1D beam analysis [24].

For dimensionally reducible structures, the effective properties and the dehomogenization results obtained from the SG modeling will be the same despite of the dimension of SG, once the chosen SG contains all the required constitutive information. For example, for the wing in Fig. 2.4a, the 2D SG, which is the airfoil is equivalent to a segment of the wing in terms of the constitutive modeling results.

If a zeroth-order approximation of the governing statement is performed [137], for heterogeneous beam structures the effective properties can be represented as a 4×4 stiffness matrix simultaneously accounting for extension, torsion, and bending in two directions and all the coupling terms; for plate/shells, the effective properties are composed of A, B, and D matrices. The second-order approximation of the governing statement can also be performed to obtain more accurate results [137, 138] if the influence of the transverse shear is significant and needed to be included explicitly in the macroscopic structural model.

Since the obtained effective stiffness matrices have the same form of that of the traditional Euler-Bernoulli beam model or Kirchhoff plate model, these traditional structural models can be used for the macroscopic structural analysis, of which the constitutive modeling can be treated as special applications of micromechanics using the concept of SG. When a 1D or 2D continua is adopted to model the beam reference line or the plate/shell reference plane, then the detailed microstructure at each material point is captured by the associated SG.

It is noteworthy that although the obtained effective stiffness matrices possess the same form of that of the traditional Euler-Bernoulli beam model or Kirchhoff plate model, the macroscopic beam model and plate model are essentially different compared with these traditional beam or plate model. From the theory formulation aspect, there is no ad hoc assumptions made to the kinematics as in traditional structural models. For example, in Euler-Bernoulli beam model, it is assumed that the beam cross section is rigid and inextensible, and a plane cross section must remain planar and normal to the deformed reference line subjected to loads. It is apparent the constraints introduced are over stiff, from the first assumption no stretching is allowed at the cross section, from the second assumption the transverse shear are neglected. In MSG, the only assumptions involved are the small strain and small local rotations of deformed SG. In addition it should be satisfied that the size of the microstructure should be asymptotically smaller than the size of the original structure in the dimensions that are kept in the macroscopic model, for example the size of the SG should be asymptotically smaller than the length of the beam-like structure. From the results obtained, all the coupling terms in effective stiffness matrices are naturally considered, the fluctuating field of the microstructure subjected to no unrealistic constraints. The accuracy of MSG beam analysis has been demonstrated to be comparable to that of the DNS through numerical example in [139–141].

For periodic structures, it is easy to identify the SG as shown in Fig. 2.4 for beams and Fig. 2.3 for plates. However, for some real structures in engineering applications, periodic microstructures may not exist, such as randomly distributed fiber enforced composites, rotor blades with varying cross section, plates with varying thickness or changing stiffeners, etc. In such cases, we rely on the expert opinion of the analysts to determine what will be the smallest representative building block of the structures, which is similar as choosing RVEs in the RVE analysis.

2.4 Extension of Mechanics of Structure Genome

Previously the MSG theory has been derived for periodic SGs in three directions for the heterogeneous solids, in which the assumption that the SG should be asymptotically smaller than the original heterogeneous solid in all the three dimensions should be satisfied. In order to deal with the problem when this assumption is not satisfied, for example the textile composites with finite thickness or inter-ply shifting, the MSG is extended. The situation when the PBCs are not physically sound and thus not applicable in all the three directions is referred as 'aperiodic' for simplicity in this work.

For beam-like structures, previously only the generalized Euler-Bernoulli beam (GEB) model is implemented in SwiftComp. When transverse shear deformation is significant, a generalized Timoshenko beam (GTB) model is required. In order to study the influence of the transverse shear loads in the free-edge stress analysis, the MSG GTB model need to be developed and implemented in SwiftComp.

In addition, GTB model with SG featuring spanwise heterogeneity is of special interest. From literature review, only very few research works successfully considered both the transverse shear deformation modes of beam and the spanwise heterogeneity in the same model. This is because the transverse shear deformation modes are inherently coupled with the bending modes in an equilibrium state of beam. In another word, an independent pure shear mode of a segment of beam with only shear force applied at the two ends cannot be in the equilibrium state except the length of the segment goes to zero, which is a cross section of the beam. Therefore, most of the work find solutions for spanwise uniform beams [137,142,143]. Based on the symplectic transfer-matrix method, Bauchau and Han [144] generalized their previous work dealing with spanwise uniform beams [142]. This is done by condensing all the DOFs in the UC to the nodes at the boundary surfaces of the UC using commercial FEA software. Then a symplectic analysis need to be conducted by specially developed codes. Both the central and extremity solutions can be solved. The results of the local fields from this method shows a very good agreement with DNS. Cheng [145] developed a new implementation of asymptotic method for the heterogeneous beam structures with periodic microstructure along its axial direction. This method can take into account the spanwise heterogeneity, and also can be conveniently implemented in commercial FEA softwares by solving BVP problems over the UC for 18 times. However, it suffers from the limitation that only the coupling terms between the two bending modes, and the coupling terms between the extension and twisting can be considered. To use this method, the other coupling terms are assumed to be zero, however, these coupling terms are unknown before the analysis. Therefore it relies on the user's experience to determine if this method can be applied to the interested heterogeneous periodic beam structure. There is also no potential to extend the method to the nonlinear regime.

This work extended the MSG and SwiftComp to deal with Timoshenko beam-like structures with spanwise heterogeneity in both homogenization and dehomogenization. This new functionality will first be used in the free-edge analysis with a 2D SG, which is a reduced case of 3D SG with spanwise heterogeneity. Then the MSG analysis of Timoshenko beam-like structures with spanwise heterogeneity will also be studied. A new strength criterion of heterogeneous beam-like structures in terms of internal forces and moments of beam is proposed, taken advantage of the accurate local fields obtained from constitutive modeling of SG.

In addition, a graphic user interface (GUI) of SwiftComp in ABAQUS is developed, which expedites the application of SwiftComp and allows user to work in a single GUI to complete the whole multiscale MSG analysis conveniently. It is noted that after creating a free account on cdmhub.org, many files used to create the results in this work can be obtained from https://cdmhub.org/projects/bopengsphdfile.

3. MSG FOR APERIODIC 3D STRUCTURES

3.1 Theory Formulations

To facilitate the formulation, two coordinate systems are set up. The macro coordinate system $\boldsymbol{x} = (x_1, x_2, x_3)$ is applied to describe the original heterogeneous structure, while micro coordinate system $\boldsymbol{y} = (y_1, y_2, y_3)$ is introduced to denote the rapid change in the material characteristics in SG. Here and throughout the paper Latin indices assume 1, 2, and 3. Repeated indices are summed over their range except where explicitly indicated. As the size of SG is much smaller than the wavelength of the macroscopic deformation, we denote $y_i = x_i/\varepsilon$, with ε being a book keeping small parameter denoting the order of the associated quantity. A field function of the original heterogeneous structure can be generally written as a function of the macro coordinates x_i and the micro coordinates y_i. The partial derivative of a function $f(x_i, y_j)$ can be expressed as

$$\frac{\partial f(x_i, y_j)}{\partial x_i} = \frac{\partial f(x_i, y_j)}{\partial x_i}|_{y_j=\text{const}} + \frac{1}{\varepsilon}\frac{\partial f(x_i, y_j)}{\partial y_i}|_{x_i=\text{const}} \equiv f_{,i} + \frac{1}{\varepsilon} f_{|i} \tag{3.1}$$

where the vertical line in the subscript indicates partial derivative with respect to a micro coordinate, that is, $w_{2|3} = \frac{\partial w_2}{\partial y_3}$. As explained in Chapter 2, SG can be 1D, 2D or 3D based on the microstructure heterogeneity. If a SG is 1D, only y_3 is needed; if a SG is 2D, y_2 and y_3 are needed; if a SG is 3D, all three coordinates y_1, y_2, y_3 are needed. For generality, we will formulate the theory for 3D SG which can be easily reduced to deal with 1D or 2D SGs.

The first step in MSG formulation derivation is to express the kinematics, including displacement field and the strain field of the original structures using those of the macroscopic structural model. To replace the original heterogeneous material with an equivalent homogeneous material, we need to first assume that the average displacement can be represented by the equivalent homogeneous material, in other words,

$$\bar{u}_i = \langle\langle u_i \rangle\rangle \tag{3.2}$$

where u_i is the displacement of the heterogeneous material. $\langle\langle \cdot \rangle\rangle$ denotes average over the SG.

We are free to express the displacement of the original heterogeneous material as two parts, namely an averaged part depending only on the macro coordinates and a fluctuating part depending both on the macro and the micro coordinates,

$$u_i(\boldsymbol{x}; \boldsymbol{y}) = \bar{u}_i(\boldsymbol{x}) + \varepsilon w_i(\boldsymbol{x}; \boldsymbol{y}) \tag{3.3}$$

with w_i termed as fluctuating functions. Substituting Eq. (3.3) into Eq. (3.2) we get the following constraints on the fluctuating functions,

$$\langle w_i \rangle = 0 \tag{3.4}$$

where $\langle \cdot \rangle = \int \cdot \mathrm{d}\Omega$ denotes an integration over the domain of the SG and Ω denotes the volume of the domain occupied by the SG. If the original heterogeneous structure is made of materials described using a Cauchy continuum, the infinitesimal strains are defined as

$$\epsilon_{ij}(\boldsymbol{x}; \boldsymbol{y}) = \frac{1}{2}\left[\frac{\partial u_i(\boldsymbol{x}; \boldsymbol{y})}{\partial x_j} + \frac{\partial u_j(\boldsymbol{x}; \boldsymbol{y})}{\partial x_i}\right] = \bar{\epsilon}_{ij} + w_{(i|j)} + \varepsilon w_{(i,j)} \tag{3.5}$$

with $\bar{\epsilon}_{ij} = \bar{u}_{(i,j)}$. Here, the parenthesis in the subscripts denotes a symmetric operation, for example, $u_{(i,j)} = \frac{1}{2}(u_{i,j} + u_{j,i})$. The last term in Eq. (3.5) is asymptotically smaller than the first two terms and its contribution to the energy can be neglected according to VAM [146]. As the equivalent homogeneous material is what created mathematically to approximate the original heterogeneous material, we need to define the strain field in terms of that of the original heterogeneous material. For 3D structures, the natural choice is

$$\bar{\epsilon}_{ij} \equiv \langle\langle \epsilon_{ij} \rangle\rangle \tag{3.6}$$

In view of Eqs. (3.5) and (3.6), we have the following constraints on the derivatives of the fluctuating functions:

$$\left\langle w_{(i|j)} \right\rangle = 0 \tag{3.7}$$

Eq. (3.7) can be written as a form of surface integration so that it can be applied to SGs with voids. The constraints will be discussed in detail in the next section.

$$\oint_{\partial\Omega} \frac{1}{2} \left(w_i n_j + w_j n_i \right) \mathrm{d}s = 0 \tag{3.8}$$

The elastic behavior of the original heterogeneous material is governed by the principle of minimum total potential energy. The governing variational statement is

$$\delta\mathcal{J} = \delta\mathcal{U} - \delta\mathcal{W} = 0 \tag{3.9}$$

where δ is the usual Lagrangian variation, $\mathcal{J}$ is the potential energy, $\mathcal{U}$ is the strain energy, and $\mathcal{W}$ is the work done by the loads of the original structure.

If we are only interested in the constitutive relations of the equivalent Cauchy continuum, it has been proved in [24] that the effects of loads can be neglected and hence the governing variational statement can be rewritten as

$$\delta\mathcal{U} = \delta \int \frac{1}{2\Omega} \left\langle D_{ijkl} \epsilon_{ij} \epsilon_{kl} \right\rangle \mathrm{d}\Omega_{\mathrm{M}} = 0 \tag{3.10}$$

where Ω_{M} is the volume of the macroscopic 3D solid model.

It is obvious that the governing statement can be further simplified to a variational statement over SG. Considering the constraints in Eqs. (3.4) and (3.7), the following functional need to be minimized:

$$\begin{aligned} J &= \left\langle \frac{1}{2} D_{ijkl} \epsilon_{ij} \epsilon_{kl} \right\rangle - \lambda_{kl} \langle w_{(k|l)} \rangle - \eta_i \left\langle w_i \right\rangle \\ &= \left\langle \frac{1}{2} D_{ijkl} \left(\bar{\epsilon}_{ij} + w_{(i|j)} \right) \left(\bar{\epsilon}_{kl} + w_{(k|l)} \right) \right\rangle - \lambda_{kl} \langle w_{(k|l)} \rangle - \eta_i \left\langle w_i \right\rangle \end{aligned} \tag{3.11}$$

where λ_{kl} and η_i are Lagrange multipliers to enforce the constraints in Eqs. (3.7) and (3.4), respectively. Note $\lambda_{ij} = \lambda_{ji}$.

Introducing the matrix notation of the strain field of the original structure Γ, the generalized strain measures for the macroscopic structural model $\bar{\epsilon}$, and the fluctuating function w as follows

$$\Gamma = \lfloor \epsilon_{11} \quad \epsilon_{22} \quad \epsilon_{33} \quad 2\epsilon_{23} \quad 2\epsilon_{13} \quad 2\epsilon_{12} \rfloor^{\mathrm{T}} \tag{3.12}$$

$$\bar{\epsilon} = \lfloor \bar{\epsilon}_{11} \quad \bar{\epsilon}_{22} \quad \bar{\epsilon}_{33} \quad 2\bar{\epsilon}_{23} \quad 2\bar{\epsilon}_{13} \quad 2\bar{\epsilon}_{12} \rfloor^{\mathrm{T}} \tag{3.13}$$

$$w = \lfloor w_1 \quad w_2 \quad w_3 \rfloor^{\mathrm{T}} \tag{3.14}$$

The strain field of the 3D original structures can also be rewritten using the matrix notation

$$\Gamma = \Gamma_h w + \Gamma_\epsilon \bar{\epsilon} \tag{3.15}$$

where Γ_h is an operator matrix depending on the dimension of the SG. If a 3D SG is used,

$$\Gamma_h = \begin{bmatrix} \frac{\partial}{\partial y_1} & 0 & 0 \\ 0 & \frac{\partial}{\partial y_2} & 0 \\ 0 & 0 & \frac{\partial}{\partial y_3} \\ 0 & \frac{\partial}{\partial y_3} & \frac{\partial}{\partial y_2} \\ \frac{\partial}{\partial y_3} & 0 & \frac{\partial}{\partial y_1} \\ \frac{\partial}{\partial y_2} & \frac{\partial}{\partial y_1} & 0 \end{bmatrix} \tag{3.16}$$

If the SG is a lower-dimensional one, one just needs to vanish the corresponding terms corresponding to the micro coordinates which are not used in describing the SG. For example, for 2D SG,

$$\Gamma_h = \begin{bmatrix} 0 & 0 & 0 \\ 0 & \frac{\partial}{\partial y_2} & 0 \\ 0 & 0 & \frac{\partial}{\partial y_3} \\ 0 & \frac{\partial}{\partial y_3} & \frac{\partial}{\partial y_2} \\ \frac{\partial}{\partial y_3} & 0 & 0 \\ \frac{\partial}{\partial y_2} & 0 & 0 \end{bmatrix} \tag{3.17}$$

Using the matrix notation, the governing statement becomes

$$J = \left\langle \frac{1}{2}(\Gamma_h w + \Gamma_\epsilon \bar{\epsilon})^{\mathrm{T}} D (\Gamma_h w + \Gamma_\epsilon \bar{\epsilon}) - \lambda \Gamma_h w - \eta \Gamma_c w \right\rangle \tag{3.18}$$

where D is the 6×6 stiffness matrix for the material, $\Gamma_h w$ denotes the constraints of Eq. (3.7), and $\Gamma_c w$ denotes the constraints of Eq. (3.4), of which Γ_c is an identity matrix. In MSG the variables to solve are the fluctuating functions. Since we directly solve the fluctuating functions, PBCs are not applied in terms of macro strain $\bar{\epsilon}_{ij}$ as in RVE analysis.

3.2 Remarks on the Constraints

Several remarks can be made within the framework of the proposed theory. First, the constraints in Eq. (3.7) are equivalent to SUBCs applied in the RVE analysis when the material constituents are perfectly bonded. This can be derived from Eq. (3.11). The principle of minimum total potential energy requires that $\delta J = 0$. By integration by parts we get

$$\begin{aligned}
0 = \delta J &= \left\langle D_{ijkl} \left(\bar{\epsilon}_{ij} + w_{(i|j)} \right) \delta \left(\bar{\epsilon}_{kl} + w_{(k|l)} \right) \right\rangle \\
&\quad - \lambda_{kl} \langle \delta w_{(k|l)} \rangle - \delta \lambda_{kl} \langle w_{(k|l)} \rangle - \eta_i \langle \delta w_i \rangle - \delta \eta_i \langle w_i \rangle \\
&= \int_\Omega \left[D_{ijkl} \left(\bar{\epsilon}_{ij} + w_{(i|j)} \right) - \lambda_{kl} \right] \delta w_{(k|l)} \mathrm{d}\Omega \\
&\quad - \delta \lambda_{kl} \langle w_{(k|l)} \rangle - \eta_i \langle \delta w_i \rangle - \delta \eta_i \langle w_i \rangle \\
&= - \int_\Omega \left[D_{ijkl} \left(\bar{\epsilon}_{ij} + w_{(i|j)} \right) - \lambda_{kl} \right]_{|l} \delta w_k \mathrm{d}\Omega \\
&\quad + \oint_{\partial\Omega} \left[D_{ijkl} \left(\bar{\epsilon}_{ij} + w_{(i|j)} \right) - \lambda_{kl} \right] n_l \delta w_k \mathrm{d}s \\
&\quad - \delta \lambda_{kl} \langle w_{(k|l)} \rangle - \eta_i \langle \delta w_i \rangle - \delta \eta_i \langle w_i \rangle \\
&= - \int_\Omega (\sigma_{kl|l} + \eta_k) \delta w_k \mathrm{d}\Omega + \oint_{\partial\Omega} \left(\sigma_{kl} - \lambda_{kl} \right) n_l \delta w_k \mathrm{d}s \\
&\quad - \delta \lambda_{kl} \langle w_{(k|l)} \rangle - \delta \eta_i \langle w_i \rangle
\end{aligned} \tag{3.19}$$

where $\partial\Omega$ denotes the boundary surfaces of the SG, and n_l are the components of the unit vector $\boldsymbol{n}$ along the exterior normal of of the boundary surfaces. In the above deduction we have utilized the fact that $\bar{\epsilon}_{ij}$ and λ_{kl} do not depend on the micro coordinates and that $\sigma_{kl} = D_{ijkl} \left(\bar{\epsilon}_{ij} + w_{(i|j)} \right)$. Since δw_k in the surface integral of the above equation is arbitrary, to make $\delta J = 0$ we have tractions $t_k = \sigma_{kl} n_l = \lambda_{kl} n_l$ on

$\partial\Omega$. It is noted λ_{kl} are six constants, therefore t_k represent uniform tractions on the boundary surfaces.

Second, other constraints, such as PBCs can be easily added to Eq. (3.18). In addition, PBCs are consistent with Eq. (3.7). For example, if a heterogeneous structure is periodic in three directions, the fluctuating functions w_i must be periodic and satisfy Eq. (2.1). It is noted that since we directly solve the fluctuating functions, the PBCs are not applied in terms of macro strain $\bar{\epsilon}_{ij}$ as in RVE analysis. PBCs automatically satisfy the constraints in Eq. (3.7), which can be easily concluded from Eq. (3.8).

Third, the present theory can also handle heterogeneous materials with partial periodicity. For convenience, the boundary surfaces normal to y_i axis are denoted as A_i, the surface with a positive exterior normal is denoted as A_i^+ while the one with a negative exterior normal is denoted as A_i^-. If a material is periodic in the in-plane directions y_1 and y_2, it is only reasonable to apply PBCs on the boundary surfaces normal to the in-plane directions, that is A_1 and A_2. In addition, the constraints in Eq. (3.7) should still be applied in the SG. We name these combined constraints as 'MIX001', where the '0' at the first place denotes periodicity in the y_1 direction, the '0' at the second place denotes periodicity in the y_2 direction, and the '1' at the third place means that no extra constraint is applied in the A_3. From the derivation in Eq. (3.19), the combined constraints MIX001 is equivalent to applying PBCs at A_1 and A_2 and apply SUBCs at A_3. Following the same notation, different combination of constraints can be named as 'MIXijk'. In 'MIXijk', the place of the number i, j, k denotes the corresponding axis direction, and number '0' at i denotes periodicity in y_i direction. Therefore, as shown in Fig. 3.1, PBCs are applied to the pair of blue surfaces: 'MIX011' means that periodic constraints are applied to the surfaces normal to y_1, 'MIX010' means periodic constraints are applied to the surfaces normal to y_1 and y_3 respectively.

When PBCs are applied in addition to the volume integral constraints in Eq. (3.7), some of the constraints can be satisfied by the PBCs applied as shown in Table 3.1. In

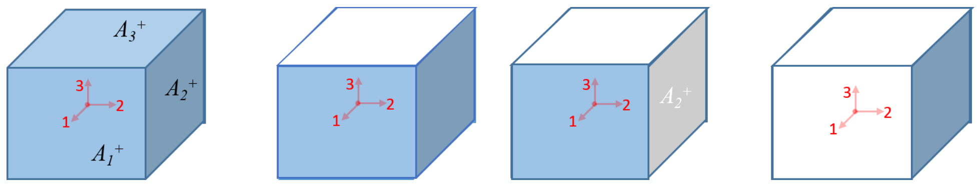

(a) PBCs (b) MIX001 (c) MIX011 (d) MIX010

Fig. 3.1. Combined boundary conditions referred in the form of 'MIXijk': PBCs are applied to the pair of surfaces in blue in addition to the volume integral constraints in Eq. (3.7).

the first three cases MIX011, MIX101 and MIX110, PBCs are applied on one pair of boundary surfaces A_i, $i = 1, 2$ or 3 respectively, five volume integral constraints need to be exerted. When PBCs are applied on two pairs of boundary surfaces, only three volume integral constraints will remain. If PBCs are applied to all the three pairs of boundary surfaces on the SG, all the volume integral constraints will be removed.

Table 3.1.
Mixed constraints of 3D SGs.

Constraints	PBCs on	$\langle w_{(1\|1)} \rangle$	$\langle w_{(2\|2)} \rangle$	$\langle w_{(3\|3)} \rangle$	$\langle w_{(2\|3)} \rangle$	$\langle w_{(1\|3)} \rangle$	$\langle w_{(1\|2)} \rangle$
MIX011	A_1	0	-	-	-	-	-
MIX101	A_2	-	0	-	-	-	-
MIX110	A_3	-	-	0	-	-	-
MIX100	A_2, A_3	-	0	0	0	-	-
MIX010	A_1, A_3	0	-	0	-	0	-
MIX001	A_1, A_2	0	0	-	-	-	0
PBCs	A_1, A_2, A_3	0	0	0	0	0	0

A 2D SG lying in the $o - y_2y_3$ plane, could be viewed as equivalent to a 3D SG that is uniform in the y_1 direction and having PBCs applied to boundary surface A_1. Comparing the constraints of Eq. (3.7) and Table 3.2, it is obvious that some components of constraints for 3D SG have been satisfied in 2D SG. Therefore, the combined constraints in a 2D SG should be written in a form of 'MIX0jk'. In addition, by applying the same boundary conditions on A_2 and A_3 on 3D SG and 2D SG, that is when the notation 'MIX0jk' are the same for 3D SG and 2D SG, the obtained constitutive relations will exactly the same. This conclusion is numerically demonstrated in section 3.4.1 using the example of a unidirectional fiber-reinforced composite.

Table 3.2.
2D SG: Volume integral constraints and surface integral constraints by components.

Volume integral	Surface integral
$\langle w_{2\|2} \rangle$	$\oint_{A_2} w_2 n_2 \mathrm{d}s$
$\langle w_{3\|3} \rangle$	$\oint_{A_3} w_3 n_3 \mathrm{d}s$
$\left\langle \frac{1}{2}(w_{2\|3} + w_{3\|2}) \right\rangle$	$\frac{1}{2} \oint_{A_3} w_2 n_3 \mathrm{d}s + \frac{1}{2} \oint_{A_2} w_3 n_2 \mathrm{d}s$
$\left\langle \frac{1}{2} w_{1\|3} \right\rangle$	$\frac{1}{2} \oint_{A_3} w_1 n_3 \mathrm{d}s$
$\left\langle \frac{1}{2} w_{1\|2} \right\rangle$	$\frac{1}{2} \oint_{A_2} w_1 n_2 \mathrm{d}s$

The constraints in Eq. (3.7) imply that the average strain can be calculated using the volume integral in Eq. (3.6), which is not valid when void part exists. To demonstrate this, first we treat the void part as filled with a dummy material. As shown in Eq. (3.20).

$$\begin{aligned} \bar{\epsilon}_{ij} &= \frac{1}{\Omega} \langle \epsilon_{ij} \rangle \\ &= \frac{1}{\Omega_m} \int_{\Omega_m} \epsilon_{ij}^m \, \mathrm{d}\Omega + \frac{1}{\Omega_v} \int_{\Omega_v} \epsilon_{ij}^v \, \mathrm{d}\Omega \\ &= \oint_{\partial\Omega_m} \frac{1}{2} (u_i n_j + u_j n_i) \, \mathrm{d}s + \oint_{\partial\Omega_v} \frac{1}{2} (u_i n_j + u_j n_i) \, \mathrm{d}s \end{aligned} \tag{3.20}$$

where Ω_m and ϵ_{ij}^m denote the volume and strain in the material part, while Ω_v and ϵ_{ij}^v denote the volume and strain in the void part. When the dummy material is removed, the Eq. (3.20) does not hold because the deformation of the void part cannot be calculated. However, when the void part is all inside the SG without intersecting the boundary surface, the first term in the last row of Eq. (3.20) can be written as

$$\oint_{\partial\Omega_m} \frac{1}{2}\left(u_i n_j + u_j n_i\right) \mathrm{d}s = \oint_{\partial\Omega} \frac{1}{2}\left(u_i n_j + u_j n_i\right) \mathrm{d}s - \oint_{\partial\Omega_v} \frac{1}{2}\left(u_i n_j + u_j n_i\right) \mathrm{d}s \quad (3.21)$$

Substitute Eq. (3.21) to Eq. (3.20), Eq. (3.8) is still valid for this case. It then can be extended to the case when PBCs are applied to the boundary surfaces with void intersected, in which Eq. (3.20) can still hold.

Lastly, to consider the finite thickness of textile composites, Espadas-Escalante proposed to use PBCs at boundary surfaces normal to the in-plane directions and SUBCs at the top and bottom surfaces and show its advantage compared with using PBCs on a UC. However, no verification is provided that the proposed mixed boundary condition can satisfy the Hill-Mandel condition [57]. The proof is given as follows.

The Hill-Mandel condition states that the volume average of the microscopic strain energy density over the UC should be equal to the macroscopic strain energy density that calculated by the macroscopic stress and strain. Consider a UC that is perfectly bonded, the Hill-Mandel condition can be expressed as

$$\langle\langle \sigma_{ij}\epsilon_{ij} \rangle\rangle - \bar{\sigma}_{ij}\bar{\epsilon}_{ij} = \frac{1}{\Omega}\oint_{\partial\Omega} n_k \left(\sigma_{ik} - \bar{\sigma}_{ik}\right)\left(u_i - y_j\bar{\epsilon}_{ij}\right) \mathrm{d}s = 0 \quad (3.22)$$

where the macro stress $\bar{\sigma}_{ij} = \frac{1}{\Omega}\int_\Omega \sigma_{ij}\mathrm{d}\Omega$ and the macro strain $\bar{\epsilon}_{ij} = \frac{1}{\Omega}\int_\Omega \epsilon_{ij}\mathrm{d}\Omega$. In addition, instead of using volume average the macro stress and strain can be expressed as integrals over the boundary surfaces of the UC,

$$\begin{aligned} \bar{\sigma}_{ij} &= \frac{1}{\Omega}\oint_{\partial\Omega} \sigma_{ik} y_j n_k \mathrm{d}s = \frac{1}{\Omega}\oint_{\partial\Omega} t_i^\circ y_i \mathrm{d}s \\ \bar{\epsilon}_{ij} &= \frac{1}{2\Omega}\oint_{\partial\Omega} \left(u_i^\circ n_j + u_j^\circ n_i\right) \mathrm{d}s \end{aligned} \quad (3.23)$$

where u_i° and t_i° are the displacements and tractions on the boundary surfaces.

For clarity the mixed boundary conditions prescribed in this case are summarized in Table 3.3. The six load cases are labeled as '11', '22', and so on, the meaning of which is self-explanatory. The superscript '$\circ$' in ϵ_{ij}° means that a macro strain component is applied to the UC. Correspondingly, u_i° means the displacement component at the boundary surfaces due to the applied macro strain. d_i denotes the length of the UC in the y_i direction.

Table 3.3.
Mixed boundary conditions

Load case	A_1	A_2	A_3
11	$u_1^{\circ+} - u_1^{\circ-} = d_1\epsilon_{11}^{\circ}$	$u_1^{\circ+} - u_1^{\circ-} = 0$	$\sigma_{i3}^{\circ} = 0$
	$u_2^{\circ+} - u_2^{\circ-} = 0$	$u_2^{\circ+} - u_2^{\circ-} = 0$	$i = 1, 3$
	$u_3^{\circ+} - u_3^{\circ-} = 0$	$u_3^{\circ+} - u_3^{\circ-} = 0$	
22	$u_1^{\circ+} - u_1^{\circ-} = 0$	$u_1^{\circ+} - u_1^{\circ-} = 0$	$\sigma_{i3}^{\circ} = 0$
	$u_2^{\circ+} - u_2^{\circ-} = 0$	$u_2^{\circ+} - u_2^{\circ-} = d_2\epsilon_{22}^{\circ}$	$i = 1, 3$
	$u_3^{\circ+} - u_3^{\circ-} = 0$	$u_3^{\circ+} - u_3^{\circ-} = 0$	
12	$u_1^{\circ+} - u_1^{\circ-} = 0$	$u_1^{\circ+} - u_1^{\circ-} = d_2\epsilon_{12}^{\circ}$	$\sigma_{i3}^{\circ} = 0$
	$u_2^{\circ+} - u_2^{\circ-} = d_1\epsilon_{12}^{\circ}$	$u_2^{\circ+} - u_2^{\circ-} = 0$	$i = 1, 3$
	$u_3^{\circ+} - u_3^{\circ-} = 0$	$u_3^{\circ+} - u_3^{\circ-} = 0$	
33	$u_i^{\circ+} - u_i^{\circ-} = 0$	$u_i^{\circ+} - u_i^{\circ-} = 0$	$\sigma_{33}^{\circ} = 1$
			$\sigma_{13}^{\circ} = \sigma_{23}^{\circ} = 0$
13	$u_i^{\circ+} - u_i^{\circ-} = 0$	$u_i^{\circ+} - u_i^{\circ-} = 0$	$\sigma_{13}^{\circ} = 1$
			$\sigma_{33}^{\circ} = \sigma_{23}^{\circ} = 0$
23	$u_i^{\circ+} - u_i^{\circ-} = 0$	$u_i^{\circ+} - u_i^{\circ-} = 0$	$\sigma_{23}^{\circ} = 1$
			$\sigma_{33}^{\circ} = \sigma_{13}^{\circ} = 0$

Before proceeding to prove the Hill-Mandel condition with the given boundary conditions in Table 3.3 for case MIX001, we have the following preliminary results:

1. On the boundary surfaces $A_i, i = 1, 3$, the following conditions stand

$$[n_k\left(\sigma_{ik} - \bar{\sigma}_{ik}\right)]^+ = -[n_k\left(\sigma_{ik} - \bar{\sigma}_{ik}\right)]^- \tag{3.24}$$

To prove this we note that $\bar{\sigma}_{ik}^+ = \bar{\sigma}_{ik}^-$ on $A_i, i = 1, 3$, because that they are volume averaged quantities and do not depend on the microscopic coordinates. On the other hand, on surface A_3 $\sigma_{ik}^+ = \sigma_{ik}^-$ which are given in the SUBCs applied on A_3. Furthermore, on surfaces A_1 and A_2 we have $[n_k\sigma_{ik}]^+ = -[n_k\sigma_{ik}]^-$ due to the fact that they are the reaction traction related to the PBCs applied on these surfaces.

2. For all of the load cases listed in Table 3.3, the following conditions stand

$$\bar{\epsilon}_{\alpha\beta} = \epsilon^{\circ}_{\alpha\beta} \qquad \alpha, \beta = 1, 2 \tag{3.25}$$

Without loss of generality here we only show the case of $\alpha, \beta = 1$ for load case 11. Other cases can be shown similarly. For this case, as listed in Table 3.3, $u_1^{\circ +} - u_1^{\circ -} = d_1 \epsilon^{\circ}_{11}$ on surface A_1. Consequently, in view of the second equation in Eq. (3.23), we have

$$\bar{\epsilon}_{11} = \frac{1}{2\Omega} \oint_{\partial\Omega} (u_1^{\circ} n_1 + u_1^{\circ} n_1) \mathrm{d}s = \frac{1}{\Omega} \int_{A_1^+, A_1^-} (u_1^{\circ +} - u_1^{\circ -}) \mathrm{d}s = \frac{1}{\Omega} \epsilon^{\circ}_{11} d_1 A_1 = \epsilon^{\circ}_{11} \tag{3.26}$$

where the terms with superscript $^+$ or $^-$ are integrated only on the corresponding surface with the same normal direction.

Generally $\bar{\epsilon}_{i3} \neq 0, i = 1, 3$ for all the load cases. This can be shown as the following

$$\begin{aligned}
\bar{\epsilon}_{\alpha 3} &= \frac{1}{2\Omega} \oint_{\partial\Omega} (u_\alpha^{\circ} n_3 + u_3^{\circ} n_\alpha) \, \mathrm{d}s \\
&= \frac{1}{2\Omega} \left[\int_{A_3^+, A_3^-} \left(u_\alpha^{+\circ} - u_\alpha^{-\circ}\right) \mathrm{d}s + \int_{A_\alpha^+, A_\alpha^-} \left(u_3^{+\circ} - u_3^{-\circ}\right) \mathrm{d}s \right] \\
&= \frac{1}{2\Omega} \int_{A_3^+, A_3^-} \left(u_\alpha^{+\circ} - u_\alpha^{-\circ}\right) \mathrm{d}s \neq 0
\end{aligned} \tag{3.27}$$

$$\bar{\epsilon}_{33} = \frac{1}{2\Omega} \oint_{\partial\Omega} (u_3^{\circ} n_3) \, \mathrm{d}s = \frac{1}{\Omega} \int_{A_3^+, A_3^-} \left(u_3^{+\circ} - u_3^{-\circ}\right) \mathrm{d}s \neq 0 \tag{3.28}$$

3. For all of the load cases, the following conditions stand

$$\bar{\sigma}_{i3} = \sigma^{\circ}_{i3} \tag{3.29}$$

In view of the first equation in Eq. (3.23) this can be shown by the following

$$\begin{aligned}
\bar{\sigma}_{i3} &= \frac{1}{\Omega} \oint_{\partial\Omega} \sigma_{ik} n_k y_3 \mathrm{d}s \\
&= \frac{1}{\Omega} \left[\int_{A_1^+, A_1^-} (\sigma_{i1}^+ - \sigma_{i1}^-) y_3 \mathrm{d}s + \int_{A_2^+, A_2^-} (\sigma_{i2}^+ - \sigma_{i2}^-) y_3 \mathrm{d}s \right. \\
&+ \frac{1}{\Omega} \left(\int_{A_3^+} \sigma_{i3}^+ y_3 \mathrm{d}s - \int_{A_3^-} \sigma_{i3}^- y_3 \mathrm{d}s \right) \\
&= \frac{1}{\Omega} \left(\int_{A_3^+} \sigma_{i3}^+ y_3 \mathrm{d}s - \int_{A_3^-} \sigma_{i3}^- y_3 \mathrm{d}s \right) \\
&= \frac{1}{\Omega} \sigma^{\circ}_{i3} d_3 A_3 \\
&= \sigma^{\circ}_{i3}
\end{aligned} \tag{3.30}$$

4. For all of the load cases, the following conditions stand

$$\bar{\sigma}_{3\alpha} = \frac{1}{A_\alpha}\int_{A_\alpha} \sigma_{3\alpha}\mathrm{d}s, \qquad \alpha = 1, 2 \tag{3.31}$$

In view of the first equation in Eq. (3.23) this can be shown by the following

$$\begin{aligned}
\bar{\sigma}_{31} &= \frac{1}{\Omega}\oint_{\partial\Omega} \sigma_{3k} n_k y_1 \mathrm{d}s \\
&= \frac{1}{\Omega}(\int_{A_1^+} \sigma_{31}^+ y_1 \mathrm{d}s - \int_{A_1^-} \sigma_{31}^- y_1 \mathrm{d}s) \\
&+ \frac{1}{\Omega}\left[\int_{A_2^+, A_2^-} (\sigma_{32}^+ - \sigma_{32}^-) y_1 \mathrm{d}s + \int_{A_3^+, A_3^-} (\sigma_{33}^+ - \sigma_{33}^-) y_1 \mathrm{d}s\right] \\
&= \frac{1}{\Omega}(\int_{A_1^+} \sigma_{31}^+ y_1 \mathrm{d}s - \int_{A_1^-} \sigma_{31}^- y_1 \mathrm{d}s) \\
&= \frac{1}{\Omega}\int_{A_1} \sigma_{31} d_1 \mathrm{d}s \\
&= \frac{1}{A_1}\int_{A_1} \sigma_{31} \mathrm{d}s
\end{aligned} \tag{3.32}$$

In the second row of Eq. (3.32), the first bracket equals to zero because of the PBCs applied on A_2, the third term equals to zero due to the applied SUBCs on A_3. In the same way, $\bar{\sigma}_{32} = \frac{1}{A_2}\int_{A_2} \sigma_{32}\mathrm{d}s$ can be proved.

Now it can be proved that the mixed boundary conditions listed in Table 3.3 satisfy the Hill-Mandel conditions. Based on Eq. (3.24), Eq. (3.22) can be written in as

$$\begin{aligned}
\langle\langle \sigma_{ij}\epsilon_{ij}\rangle\rangle - \bar{\sigma}_{ij}\bar{\epsilon}_{ij} =& \frac{1}{\Omega}\oint_{\partial\Omega} n_k \left(\sigma_{ik} - \bar{\sigma}_{ik}\right)\left(u_i - y_j\bar{\epsilon}_{ij}\right)\mathrm{d}\Omega \\
=& \frac{1}{\Omega}\int_{A_1} \left(\sigma_{i1} - \bar{\sigma}_{i1}\right)\left[\left(u_i - y_j\bar{\epsilon}_{ij}\right)^+ - \left(u_i - y_j\bar{\epsilon}_{ij}\right)^-\right]\mathrm{d}s \\
&+ \frac{1}{\Omega}\int_{A_2} \left(\sigma_{i2} - \bar{\sigma}_{i2}\right)\left[\left(u_i - y_j\bar{\epsilon}_{ij}\right)^+ - \left(u_i - y_j\bar{\epsilon}_{ij}\right)^-\right]\mathrm{d}s \\
&+ \frac{1}{\Omega}\int_{A_3} \left(\sigma_{i3} - \bar{\sigma}_{i3}\right)\left[\left(u_i - y_j\bar{\epsilon}_{ij}\right)^+ - \left(u_i - y_j\bar{\epsilon}_{ij}\right)^-\right]\mathrm{d}s
\end{aligned} \tag{3.33}$$

The first two expressions after the second equal sign are 0, because based on Eq. (3.25) and the applied PBCs on A_1 and A_2, when $i = 1$ and 2,

$$\left(u_i - y_j\bar{\epsilon}_{ij}\right)^+ - \left(u_i - y_j\bar{\epsilon}_{ij}\right)^- = 0 \tag{3.34}$$

When $i=3$,

$$\begin{aligned}&\frac{1}{\Omega}\int_{A_1}(\sigma_{31}-\bar{\sigma}_{31})\left[(u_3-y_1\bar{\epsilon}_{31})^+-(u_3-y_1\bar{\epsilon}_{31})^-\right]\mathrm{d}s\\=&\frac{1}{\Omega}d_1\bar{\epsilon}_{31}\int_{A_1}(\sigma_{31}-\bar{\sigma}_{31})\,\mathrm{d}s\end{aligned}\tag{3.35}$$

In the same way,

$$\begin{aligned}&\frac{1}{\Omega}\int_{A_2}(\sigma_{32}-\bar{\sigma}_{32})\left[(u_3-y_2\bar{\epsilon}_{32})^+-(u_3-y_2\bar{\epsilon}_{32})^-\right]\mathrm{d}s\\=&\frac{1}{\Omega}d_2\bar{\epsilon}_{32}\int_{A_2}(\sigma_{32}-\bar{\sigma}_{32})\,\mathrm{d}s\end{aligned}\tag{3.36}$$

Due to Eq. (3.33), Eq. (3.35), (3.36) are zero. The third expression in Eq. (3.33) also equals to 0 according to Eq. (3.29). Therefore Eq. (3.33) has been proved to be zero and thus the Hill-Mandel condition has been proved to be satisfied when the considered mixed boundary conditions are applied.

From Eq. (3.35) and Eq. (3.36), it can also be observed that if the third constraints on A_1 and A_2 in Table 3.3, i.e. $u_3^{\circ+}-u_3^{\circ-}=0$ are changed to $u_3^{\circ+}-u_3^{\circ-}=\epsilon_{\alpha 3}^{\circ}$, the Hill-Mandel condition will still be satisfied and the same effective properties and dehomogenization relations will be obtained. However, a different rigid body rotation will be observed.

3.3 Finite Element Implementation

3.3.1 Finite Element Formulation

To minimize the functional in Eq. (3.18) for general cases, we need to turn to numerical techniques such as the FEM. It is possible to formulate the FEM solution based on Eq. (3.18) directly. However, since the constraints of the last term do not affect the minimum value of J but help uniquely determine the fluctuating functions, in practice we can constrain the fluctuating functions at an arbitrary node to be zero and later use these constraints to recover the unique fluctuating functions. Discretize w using the finite elements as

$$w(x_i;y_j)=S(y_j)V(x_i)\tag{3.37}$$

where S represents the shape functions and V a column matrix of the nodal values of the fluctuating functions. Note that in this work, the 2D elements still have three degrees of freedom at each node.

Substituting Eq. (3.37) into Eq. (3.18), we obtain a discretized version of the functional J as

$$J = \frac{1}{2}\left(V^{\mathrm{T}}EV + 2V^{\mathrm{T}}D_{h\epsilon}\bar{\epsilon} + \bar{\epsilon}^{\mathrm{T}}D_{\epsilon\epsilon}\bar{\epsilon}\right) - V^{\mathrm{T}}D_{h\lambda}^{\mathrm{T}}\lambda \tag{3.38}$$

where

$$E = \left\langle (\Gamma_h S)^{\mathrm{T}} D\,(\Gamma_h S)\right\rangle \quad D_{h\epsilon} = \left\langle (\Gamma_h S)^{\mathrm{T}} D\right\rangle \quad D_{\epsilon\epsilon} = \langle D\rangle \quad D_{h\lambda} = \langle \Gamma_h S\rangle^{\mathrm{T}} \tag{3.39}$$

It is noted that the last term $\langle \eta\Gamma_c w\rangle$ in Eq. (3.18) is dropped, because this constraint is equivalent to remove the rigid body translation, therefore it can be easily applied by fixing a node. If PBCs on A_i are applicable, the PBCs can be imposed by enforcing nodal values of nodes on A_i^+ and on A_i^+- to be equal and reducing the DOFs of the SG analysis. Minimizing J in Eq. (3.38) gives us the following linear system

$$\begin{bmatrix} E & -D_{h\lambda} \\ -D_{h\lambda}^{\mathrm{T}} & 0 \end{bmatrix}\begin{bmatrix} V \\ \lambda \end{bmatrix} = \begin{bmatrix} -D_{h\epsilon}\bar{\epsilon} \\ 0 \end{bmatrix} \tag{3.40}$$

It is clear that V will linearly depend on $\bar{\epsilon}$, and the solution can be symbolically written as

$$V = V_0\bar{\epsilon} \tag{3.41}$$

With the solution in Eq. (3.41), we can calculate the strain energy storing in the SG as the first approximation as

$$U = \frac{1}{2}\bar{\epsilon}^{\mathrm{T}}\left(D_{\epsilon\epsilon} + V_0^{\mathrm{T}}D_{h\epsilon}\right)\bar{\epsilon} \equiv \frac{\Omega}{2}\bar{\epsilon}^{\mathrm{T}}\bar{D}\bar{\epsilon} \tag{3.42}$$

where $\bar{D}$ is the effective stiffness matrix to be used in the macroscopic structural analysis.

The local fields within the SG can also be obtained based on the global displacement $\bar{u}$ and global strain $\bar{\epsilon}$. Knowing $\bar{\epsilon}$, we can compute the fluctuating function as

$$w = SV_0\bar{\epsilon} \tag{3.43}$$

therefore from Eq. (3.3)

$$u = \bar{u} + SV_0\bar{\epsilon} \tag{3.44}$$

The local strain field can be obtained using Eq. (3.15) as

$$\epsilon = \bar{\epsilon} + \Gamma_h SV_0\bar{\epsilon} \tag{3.45}$$

The local stress field can be obtained directly using the Hooke's law as

$$\sigma = D\epsilon. \tag{3.46}$$

3.3.2 Locking in Finite Element Analysis

The MSG theory has been implemented into a code SwiftComp based on FEM. The standard integration technique used in the previous version of SwiftComp could introduce locking phenomenon in the constitutive model of SG, influence the accuracy of both the effective properties and the local fields, and reduce the convergence rate of the results in terms of mesh density.

In order to improve the accuracy of the SG constitutive modeling, different integration techniques are implemented according to the element types. The reduced integration techniques are used for the 20-noded brick element and the 8-noded quadrilateral element, and the B-bar method is implemented for the 8-noded brick element and the 4-noded quadrilateral element. It is noted that the application of B-bar method is slightly adapted for the 4-noded quadrilateral element in SwiftComp, compared with that applied to the usual plane-stress or plane strain 4-noded quadrilateral element. The reason is that in SwiftComp, each node of 2D SG still keeps three DOFs of fluctuating functions, as indicated in Eq. (3.14) and (3.37).

Finite elements are referred to 'lock' if they produce nonphysically over stiff response of deformation, rendering unusable results. Locking can occur for a number of reasons. In the 2D and 3D continuum elements that used in solid structural analysis, the most common cause is that the finite element shape functions are unable to properly approximate the strain field and thus the solution converges slowly as the mesh size is reduced [147].

The most common locking phenomena are shear locking and volumetric locking due to the strain component that is not correctly approximated. For example, shear locking happens when using the standard 4-noded quadrilateral elements to approximate the strain distribution of in-plane bending, since the bilinear shape functions of this element type cannot correctly interpolate the bending displacement field and will give rise to large, nonphysical shear stiffness in bent elements. Shear locking is thought to be relatively benign because it can be avoided by using higher order elements, and in some cases by refining the mesh sufficiently [147]. Incompatible element types have also been designed to avoid shear locking, in which an additional strain distribution mode is added to accurately approximate bending [148].

Volumetric locking arises in the analysis of (almost) incompressible materials, such as isotropic materials with Poisson's ratio approaching to 0.5. In the incompressible limit, the volumetric strain at any of the material points should be zero, which put the incompressibility constraints to the finite element. However, the finite element shape functions usually cannot vanish the volumetric strain at all the integration points in the element. The nonzero volumetric strain derived from the shape functions will result in unreasonable large virtual power, and thus make the element over stiff.

Volumetric locking is considered to be more severe than shear locking, because it cannot be avoided by refining the mesh, and it almost exists in all the commonly used standard fully integrated continuum element types at the incompressible limit [149]. Poor performance even appears when Poisson's ratio is as small as 0.45 in some element types. Nagtegaal et.al [150] evaluated the suitability of the commonly used finite elements for incompressible conditions and found that only the 6-noded triangular element and 10-noded tetrahedron could be used at the incompressible limit. Sloan and Randolph [151] demonstrated that higher order elements, compared with the first order elements, are less likely to produce volumetric locking.

Several kinds of methods have been developed to avoid volumetric locking, including reduced integration [147,147], selectively reduced integration [152] and B-bar method [153]. Reduced integration is to reduce the number of integration points one order less accurate than the standard full integration scheme. For example, in the case of 8-noded quadrilateral element, a 2×2 scheme will be used, reduced from the standard 3×3 integration scheme. Reduced integration technique works great for quadratic quadrilateral and brick elements, because it can completely resolves locking and even improves the accuracy of the elements [147]. However, for 4-noded quadrilateral elements or 8-noded brick elements, reduced integration can reduce the rank of the total stiffness tensor, and make the total stiffness matrix singular. This can result in spurious deformation mode that make the material deform without causing any stress. This phenomenon is known as 'hourglassing' [147]. It is also noteworthy that the linear triangular and tetrahedral elements cannot be reduced and are not suitable to be used modeling near incompressible materials.

To use 4-noded quadrilateral elements or 8-noded brick elements, selectively reduced integration or B-bar method can be used. Both of these two methods works by separating the virtual power into a volumetric part and a deviatoric part and treating them separately. The deviatoric part is integrated in the standard way, while the volumetric part is computed in an average sense to reduce the over estimated dilatation stiffness.

The selectively reduced integration works well for isotropic materials in the linear elasticity range. In this case the element stiffness matrix can be reduced to two components, one is related to the dilatational strain, and the other is related to the deviatoric strain. The selectively reduced integration method integrates the deviatoric part of the stiffness matrix using the full integration scheme, and integrate the volumetric strain related part of element stiffness using the reduced integration scheme. However, for orthotropic and anisotropic materials, or elasto-plastic materials, the extension of this method is ambiguous and computationally inconvenient.

In contrast, the B-bar method, proposed by Hughes [153], can be easily generalized to deal with orthotropic and anisotropic materials in finite strain problems. This method is chosen in this work. In B-bar method, the definition of the strain in the element is modified. Here, the B-bar method in small strain linear elasticity is illustrated.

The element stiffness matrix and the element internal force are represented as

$$K^e = \int_{\Omega^e} B^{\mathrm{T}} D B \, \mathrm{d}\Omega \tag{3.47}$$

$$f^e = \int_{\Omega^e} B^{\mathrm{T}} \sigma \, \mathrm{d}\Omega \tag{3.48}$$

where B is the strain-displacement matrix,

$$B = \lfloor B_1, B_2, \ldots, B_{n_{en}} \rfloor \tag{3.49}$$

and n_{en} is the number of element nodes. In 3D analysis, a submatix of B can be denoted as B_a, $1 \leq a \leq n_{en}$.

$$B_a = \begin{bmatrix} b_1 & 0 & 0 \\ 0 & b_2 & 0 \\ 0 & 0 & b_3 \\ 0 & b_3 & b_2 \\ b_3 & 0 & b_1 \\ b_2 & b_1 & 0 \end{bmatrix} \tag{3.50}$$

In Eq. (3.50),

$$b_i = \frac{\partial S_a}{\partial x_i} \tag{3.51}$$

where S_a is the shape function associated with node a, and x_i is the ith Cartesian coordinate.

To apply these standard expressions into nearly incompressible materials, the definition of B_a must be changed. The procedures start with separating B_a with a dilatational part B_a^{dil} and a deviatoric part B_a^{dev}.

$$B_a^{dil} = \frac{1}{3} \begin{bmatrix} b_1 & b_2 & b_3 \\ b_1 & b_2 & b_3 \\ b_1 & b_2 & b_3 \\ 0 & 0 & 0 \\ 0 & 0 & 0 \\ 0 & 0 & 0 \end{bmatrix} \tag{3.52}$$

The deviatoric part of B_a is then defined as

$$B_a^{dev} = B_a - B_a^{dil} \tag{3.53}$$

An improved form of B_a^{dil} must be chosen to achieve an effective formulation for nearly incompressible applications, denoted by $\bar{B}_a^{dil}$.

$$\bar{B}_a^{dil} = \frac{1}{3}\begin{bmatrix} \bar{b}_1 & \bar{b}_2 & \bar{b}_3 \\ \bar{b}_1 & \bar{b}_2 & \bar{b}_3 \\ \bar{b}_1 & \bar{b}_2 & \bar{b}_3 \\ 0 & 0 & 0 \\ 0 & 0 & 0 \\ 0 & 0 & 0 \end{bmatrix} \tag{3.54}$$

Now we use $\bar{B}_a$ to replace B_a to be used in Eq. (3.47),

$$\bar{B}_a = B_a^{dev} + \bar{B}_a^{dil} = B_a - B_a^{dil} + \bar{B}_a^{dil} \tag{3.55}$$

which explicitly gives

$$\bar{B}_a = \begin{bmatrix} b_5 & b_6 & b_8 \\ b_4 & b_7 & b_8 \\ b_4 & b_6 & b_9 \\ 0 & b_3 & b_2 \\ b_3 & 0 & b_1 \\ b_2 & b_1 & 0 \end{bmatrix} \tag{3.56}$$

where

$$\begin{aligned} b_4 &= \frac{\bar{b}_1 - b_1}{3} \\ b_5 &= b_1 + b_4 \\ b_6 &= \frac{\bar{b}_2 - b_2}{3} \\ b_7 &= b_2 + b_6 \\ b_8 &= \frac{\bar{b}_3 - b_3}{3} \\ b_9 &= b_3 + b_8 \end{aligned} \tag{3.57}$$

The B-Bar method then reduces to choosing appropriate $\bar{b}_i$. Hughes [153] presented many forms of $\bar{b}_i$. In this work, a specialization to the mean-dilation element of Nagtegaal [150] is used which takes the form shown below

$$\bar{b}_i = \frac{\int_{\Omega^e} b_i \, \mathrm{d}\Omega^e}{\int_{\Omega} \mathrm{d}\Omega} \tag{3.58}$$

This means that the dilation contribution is computed from the mean value of b_i, thereafter the name of mean-dilation element.

Traditionally, 2D elements are used for plane strain/stress cases and the B matrix should be modified as

$$B_a = \begin{bmatrix} b_1 & 0 & 0 \\ 0 & b_2 & 0 \\ b_2 & b_1 & 0 \end{bmatrix} \tag{3.59}$$

However, in this work 2D elements keep all the three DOFs. Corresponding to the 3D strains of the 2D elements in Eq. (3.17), the form of B_a is

$$B_a = \begin{bmatrix} 0 & 0 & 0 \\ 0 & b_2 & 0 \\ 0 & 0 & b_3 \\ 0 & b_3 & b_2 \\ b_3 & 0 & 0 \\ b_2 & 0 & 0 \end{bmatrix} \tag{3.60}$$

3.4 Validation and Application of Solid Model

The present theory is implemented in SwiftComp, a general-purpose multiscale constitutive modeling code. In this section, first of all the influence of different boundary conditions with respect to the apparent properties of fiber-reinforced composite is studied. Then to further illustrate the influence of the different constraints, the concentric cylinder assemblage (CCA) model is solved using the current method and compared with the results given by [154]. Woven composites are studied using the current theory. The effective properties of a plain-weave composite is first studied and compared with experiment results. Then a 3D orthogonal interlock composite is studied and the results are compared with 3D direct FE simulation to demonstrate the effectiveness of the theory in both homogenization and dehomogenization. A randomly distributed short fiber reinforced composite is studied when it is difficult to create periodic nodes on the corresponding boundary surfaces. Two examples of porous materials are used to demonstrate that this theory is also applicable to materials with voids.

3.4.1 Influence of Boundary Conditions to Apparent Properties

In order to understand the influence of the different boundary conditions, an example of a unidirectional fiber reinforced composite is used. The SG is made of an isotropic matrix material ($E = 3.45$ GPa, $\nu = 0.37$) and a transversely isotropic fiber ($E_L = 58.61$ GPa, $E_T = 14.49$ GPa, $G_{LT} = 5.38$ GPa, $\nu_{LT} = 0.250$, $\nu_{TT} = 0.247$) with volume fraction of fiber equal to 0.6. 3D SG and 2D SG are shown in Fig. 3.2. In order to study the influence of the boundary conditions to the apparent properties, homogenization is conducted with different constraints, including PBCs, KUBCs, SUBCs, and four combined constraints MIX011, MIX010, MIX001 and MIX100. The number of SGs in each direction is increased from 1 to 3, therefore the total number of SGs increased from 1 to 8 and then to 27. The obtained apparent properties are shown in Fig. 3.3, in which the vertical axis value r is the relative difference calculated by

$$r = (P - P_{\mathrm{PBCs}})/P_{\mathrm{PBCs}} \times 100(\%) \tag{3.61}$$

where P is a certain apparent property calculated using the considered boundary conditions, P_{PBCs} is the corresponding effective property obtained with PBCs. It should be noted that in Fig. 3.3, curves are used for better visualization of the apparent properties, which have no physical meaning as the horizontal axis is the number of SGs, only symbols correspond to real results.

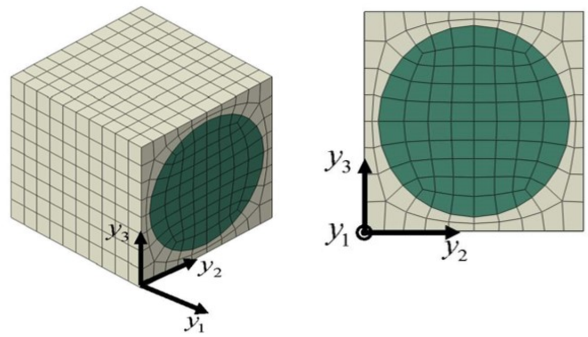

(a) 3D SG (b) 2D SG

Fig. 3.2. SG of the unidirectional fiber reinforced composite.

The SG of the unidirectional fiber-reinforced composite is transversely isotropic when PBCs, KUBCs, SUBCs, MIX011 and MIX100 are applied, in which the effective properties will remain transversely isotropic. In MIX010 model PBCs are applied to A_1, A_3 while in MIX001 model PBCs are applied to A_1, A_2. Therefore in these two cases the effective material will not be transversely isotropic. However, the E_2, G_{12} and ν_{12} from MIX010 are equal to the E_3, G_{13} and ν_{13} from MIX001, respectively. Therefore, E_3, G_{13} and ν_{13} are not included in Fig. 3.3.

It is well accepted that KUBCs model is most kinematically constrained and provides the upper bound for the apparent stiffness tensor, while the SUBCs model is equivalent to the minimum kinematical constraints and provides the lower bounds for the apparent stiffness tensor. Other boundary conditions such as PBCs and MUBCs provide apparent stiffness lying between [155]. It is obvious to find the results shown in Fig. 3.3 are consistent with this conclusion. As the number of SGs increasing, all the apparent properties P show an expected convergence to the effective properties predicted by PBCs. For SGs with periodicity in all three directions, denoted as 'PBC' in the Fig. 3.3, results remain the same no matter how many SGs used in the analysis. In addition, E_1, E_2, G_{12}, G_{13} obtained from combined constraints MIX011, MIX010, MIX001, and MIX100 lie between the bound values from using PBCs and

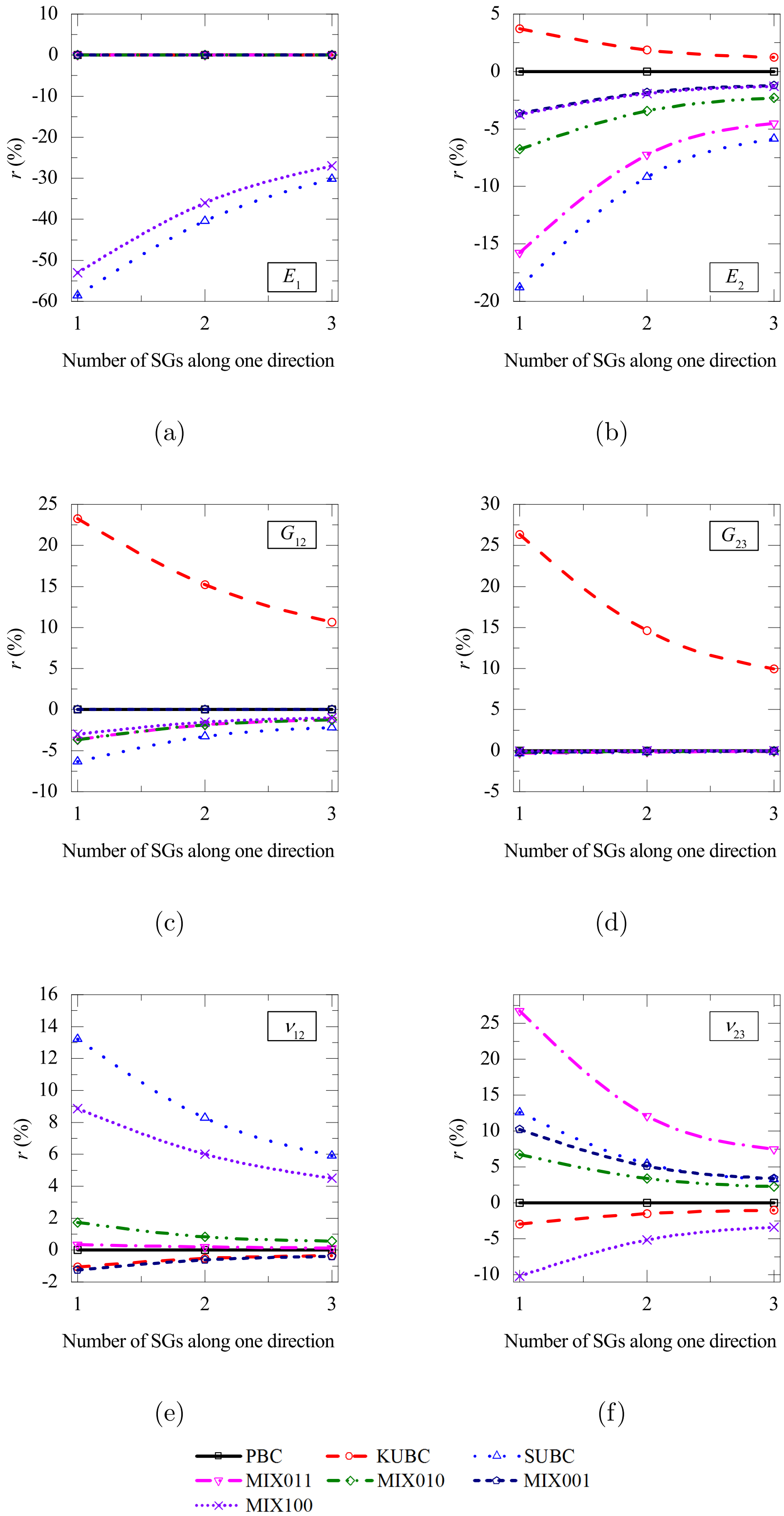

Fig. 3.3. Influence of the boundary conditions on the homogenized properties.

SUBCs. The reason is in the combined constraints PBCs are partially substituted by the volume integral constraints in Eq. (3.7) which are weaker constraints.

From Fig. 3.3(a), it can be observed that when strain based constraints are applied to A_1, including MIX011, MIX010 and MIX001, PBCs and KUBCs, the E_1 from all these models agree very well. When the PBCs are removed, i.e., in MIX100 and SUBCs, E_1 is much smaller compared with that from PBCs. Therefore, if PBCs are applied nonphysically, large error could be introduced into the model.

As shown in Fig. 3.3(a) and 3.3(b), E_1 from MIX100 is much smaller than that from PBCs, as well as E_2 from MIX010 compared with that from PBCs. The amplitude of r in the first case is much larger than that of the second case. This phenomenon can be explained using boundary layer that created by the boundary conditions. PBCs converge fastest in terms of volume element size, because PBCs introduce the thinnest boundary layer if the material is not periodic, and has no boundary layer for periodic materials. An RVE is a volume element that the influence of the boundary layer can be neglected with regarding to the homogenized behavior. The microstructure also influences the thickness of boundary layer. When the material is more homogeneous on the boundary surfaces, the apparent properties will converge faster with respect to the size of of the volume element [31]. In the SG of this example, fiber only intersects A_1, while on A_2 and A_3 the material is homogeneous. Therefore, compared the difference ratio r for E_1 in MIX100 model (in Fig. 3.3(a)) with r for E_2 from MIX010 model (in Fig. 3.3(b)), the amplitude of r in the first case is much larger than that of the second case.

In Fig. 3.3(b), PBCs are applied to A_2 in MIX001 and MIX100, therefore they predict a larger E_2 compared with the cases in MIX010 and MIX011, in which PBCs are not applied to A_2. MIX011 predicts a lower E_2 than MIX010 because less constraints are imposed on A_3.

As shown in Fig. 3.3(c), G_{12} is mainly related with the boundary conditions applied to A_1 and A_2. When PBCs are applied to these two pairs of surfaces such as in MIX001, the obtained G_{12} is the same as that from PBCs. When PBCs are missing on A_1 or A_2 in the other combined constraints, G_{12} is smaller. From Fig. 3.3(d), it seems G_{23} is less sensitive with respect to the boundary conditions except KUBC, which probably related to the symmetry and homogeneous material distribution on A_2 and A_3. In this example, it is observed significant error is created by using KUBCs when predicting the shear modulus G_{12} and G_{23}.

The Poisson's ratios from the combined constraints are not within the range between that from KUBCs and SUBCs because this cannot be concluded from the bounds of the apparent stiffness tensor. However, they also display a consistent convergence tendency as SGs increasing.

It is also noted that in this case the 3D SG features no heterogeneity in y_1 direction, therefore a 2D SG as shown in Fig. 3.2(b) can be used to produce exactly the same effective property values with 3D SG once the constraints in the two models are equivalent as discussed in section 3.2. For example, numerical test results show a perfect agreement between the constitutive relations obtained from 3D SG using MIX001 and that obtained from 2D SG with PBCs applied at the edges normal to y_2. The principle also applies to microstructures featuring 1D heterogeneity. Such capability of using 1D or 2D SGs to obtain 3D properties is not possible using the RVE analysis.

3.4.2 CCA Model

CCA model [154, 156] is a well-known analytic micromechanics model to obtain composite effective elastic properties in terms of the constituent properties and their volume fractions without considering the real microstructure of the composite. The current example use the geometry of the CCA model as shown in Fig. 3.4. In the model, the inner cylinder is graphite fiber with transversely isotropic properties ($E_L =$ 345 GPa, $E_T = 9.66$ GPa, $G_{LT} = 2.07$ GPa, $\nu_{LT} = 0.20$, $\nu_{TT} = 0.30$), while the annulus is epoxy with isotropic properties ($E = 3.45$ GPa, $\nu = 0.35$).

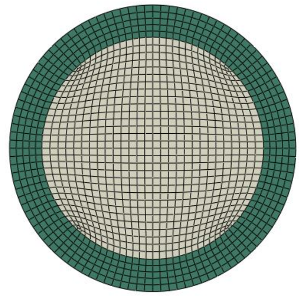

Fig. 3.4. A mesh of the CCA model with fiber volume fraction of 0.6.

However, when calculating the effective transverse properties E_T, G_{TT}, ν_{TT}, the implementation of two different boundary conditions resulted into two bounds. Upper bounds of G_{TT} and E_T are obtained from using the transverse shear displacement boundary condition, while the lower bounds of them are calculated from using the uniform traction boundary conditions.

The MSG analysis is carried out using the 2D SG as shown in Fig. 3.4 with only the volume integral constraints in Eq. (3.7) applied. It is noted based on the 2D SG configuration, the terms $\langle w_{i|1} \rangle$ in Eq. (3.7) are reduced, that is $\langle w_{i|1} \rangle = 0$ are automatically satisfied, while the remaining components of constraints are equivalent to the uniform traction boundary condition. As discussed in section 1.4.1, the 2D SG could be viewed as a 3D SG formed by sweeping the 2D SG along the fiber direction and with PBCs applied on the boundary surfaces normal to the fiber direction.

It can be shown in the fist column of Fig. 3.5 that the analytical exact solution of the axial effective properties E_L, G_{LT}, ν_{LT} can be reproduced exactly by the current method. This can be justified by the equivalence of the constraints imposed in the MSG analysis and the boundary conditions applied in the Hashin's formulation. In the work of Hashin [154], the axial effective properties E_L, G_{LT}, ν_{LT} are exact solution based on the basic assumption that the unidirectional fiber-reinforced composite is infinitely long thus deform in a plane strain state, which can be viewed as KUBCs are applied in the fiber direction. The PBCs in MSG and the KUBCs applied in Hill's analytic formulation are equivalent based on the uniformity in the fiber direction. In addition, due to the uniformity in the circumference direction of the two phase circular configuration, the applied strain ϵ_{1i}^0 will resulted in uniform tractions on the lateral surface, either zeros or a constants. As discussed, in MSG analysis of the 2D SG, the applied constraints are equivalent to uniform traction boundary conditions. Therefore for the CCA model, MSG and Hashin's analytical method actually are solving the same governing equations to obtain the axial effective properties E_L, G_{LT}, ν_{LT}, which will lead to the same results.

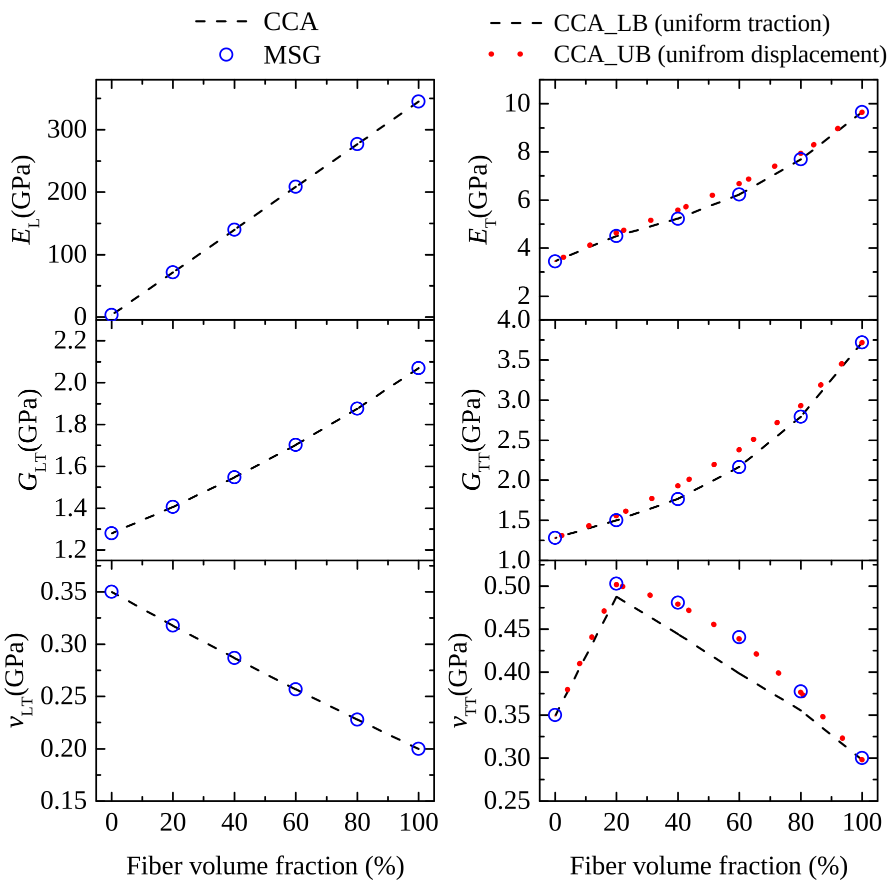

Fig. 3.5. Effective properties of CCA model of different fiber volume fraction.

As shown in the second column of Fig. 3.5, the effective E_T, G_{TT}, ν_{TT} from MSG analysis agree very well with the analytic lower bound [154], which is also due to the fact that uniform tractions are either resulted from the constraints applied in the MSG analysis or applied on the lateral surface directly as loading condition in Hashin's formulation.

This example demonstrates that the present theory can deal with material microstructures with arbitrary shape. For non-cuboid SGs, it is noted that additional boundary conditions could also be applied if necessary. For example, Glüge implemented PBCs to spherical RVE by enforcing the PBC relation to node pairs that have opposite normal direction on the spherical boundary surface. This same technique can be adapted in SG analysis by simply imposing w_i to be the same for each node pair that have opposite normal direction. Non-cuboid RVE has shown adavantegous in the published works. Glüge studied a macroscopically isotropic matrix-inclusion material of which the inclusions are randomly distributed. It is observed that with PBCs applied, cubic RVEs introduce spurious anisotropy to the homogenized properties and converge slower than using spherical RVEs in terms of RVE size. The influence of the RVE shape was also examined in the work of Firooz [157] based on unidirectional fiber-reinforced material. PBCs, KUBCs and SUBCs are considered for three packing patterns: the square packing (Fig. 3.2(b)), hexagonal packing and circular packing(Fig. 3.4), of which the fiber and the matrix are isotropic. It is observed that the circular RVE is most suitable to predict the overall isotropic material properties. Therefore MSG could have a great potential in more applications.

3.4.3 Finite Thickness Effects of Plain-weave Composites

In this section, a plain-weave composite is implemented to study the finite thickness effect. Since using the present theory, the layers within the unit cell are explicitly modelled, the physical interactions of the neighbouring layers are naturally considered. In the plain-weave composite example, the model geometry and material properties used are shown in Table 3.4 and Fig. 3.6. The effective properties of plain-weave composites are predicted and validated with experimental data from [50, 158]. The effective properties using PBCs on a single UC in the current model are compared in Table 3.6 with the available analytic model results of Scida [50], Donadon [159], and Priank [160]. Note the UC geometry (Fig. 3.6) are described using different models with the parameters given in Table 3.5, in which a_w and h are the width and the thickness of the UC, h_w and h_f are the maximum thickness of the yarns. The undulation of yarns are defined based on Cosine functions in Scida's work [50] across the width of the UC, while a piecewise function containing horizontal parts and trigonometry functions is developed by Donadon [159] and later implemented by Priank [160], in which the horizontal parts has a dimension of $\frac{1}{2}(a_w - u_w)$. However, direct implementation of these models in FE modeling resulted in larger yarn volume fraction compared with the test value, as well as poor element quality between yarns. Therefore in this work the UC geometry is adapted and the undulation of the yarn is described using circular arc with radius of r that begins at the lateral surface and ends at the center section of the UC. In all the geometry models, the shape of the yarns in both the warp and fill directions are the same. As shown in Table 3.6, the effective properties obtained from each model are not all within the test data range, which probably due to different description of the UC geometry. The effective properties are found to be sensitive to the UC geometry definition, therefore it is important to use accurate definition of the undulation and cross section of yarns, which, however is beyond this work.

Table 3.4.
Material properties of the plain-weave composites.

Materials	E_1 (GPa)	E_2 (GPa)	G_{12} (GPa)	G_{23} (GPa)	ν_{12}	ν_{23}
E-glass	73	73	30.4	30.4	0.20	-
Vinyl Derakane	3.4	3.4	1.49	1.49	0.35	-
Yarn	57.5	18.8	7.44	7.26	0.25	0.29

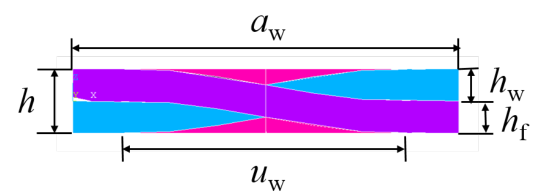

(a) Half of the SG section of models [50, 159, 160]

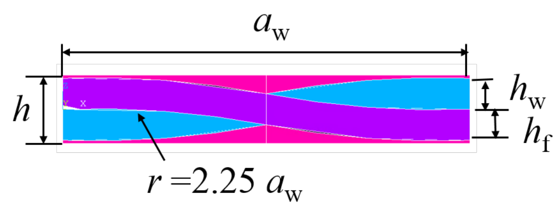

(b) Half of the SG section of the present model

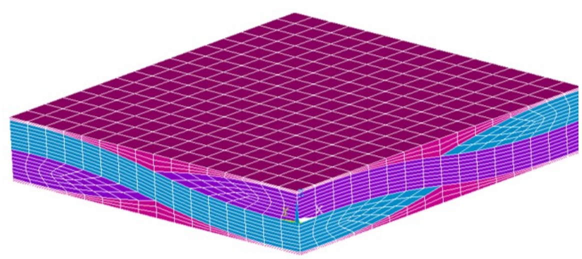

(c) 1/4 SG of the current model

Fig. 3.6. Geometry models of the plain-weave SG.

Table 3.5.
Geometric parameters of the models (mm).

Model	$2a_w$	$h_f = h_w$	h_t	u_w
Scida [50]	0.60	0.05	0.10	0.30
Donadon [159], Priyank [160]	0.60	0.05	0.10	0.20
Present model	0.60	0.0491	0.10	-

In order to consider the finite thickness effect, the effective properties of five plain-weave composite plates are calculated, which have 1, 2, 4, 8, 16 layers through the thickness, respectively. Since the periodicity of the microstructure is only in the in-plane directions, the combined constraints MIX001 are used. The difference ratios are calculated based on the results obtained from using PBCs (Eq. (3.61)) and plotted in Fig. 3.7. It can be shown that as the number of layers increases, the effective properties will converge to that from using PBCs. Consistent with the observation in the example in section 3.4.1. Compared with the results obtained from PBCs, all the effective modulus $E_1 = E_2$, E_3, $G_{12} = G_{13}$ and G_{23} obtained from MIX001 are smaller, while the Poisson's ratios are larger.

Table 3.6.
Effective material properties of the plain-weave composites.

	Test [50, 158]	Scida [50]	Donadon [159]	Priyank [160]	MSG PBC
Yarn vof	0.678	0.63	0.74	0.74	0.68
E_1 (GPa)	24.8±1.10	25.33	25.8	29.5	26.13
E_3 (GPa)	8.50±2.60	13.46	13.26	8.96	10.71
G_{12} (GPa)	6.50±0.80	5.19	5.12	6.29	5.22
G_{23} (GPa)	4.20±0.70	5.24	5.02	3.39	3.51
ν_{12}	0.12±0.01	0.12	0.15	0.14	0.14
ν_{23}	0.28±0.07	0.29	0.31	0.33	0.33

It is observed G_{12} is insensitive to the number of layers through the thickness, possibly because the PBCs are maintained on the four lateral surfaces normal to the in-plane directions, and the plain-weave textile composite has a symmetrical microstructure. The other effective properties are seen to be influenced by the thickness which is most significant when the number of layers of the plate changed from a single ply to two plies. For a single ply case, E_1, E_3 and G_{23} have a obvious difference from the results obtained from PBCs, corresponding to very large Poisson's ratio ν_{13}. E_3 is the most reduced modulus, followed by G_{23} and then E_1. This is understandable since when the plate has only one layer, there is no support from the neighbouring layers. When the PBCs are maintained on the lateral surfaces, E_3 is most influenced by the constraints applied on the top and bottom surfaces of the UC, which converges slower than E_1 and G_{23}. Although for this example, there is no test data for comparison regarding to the finite thickness effect, there is another experimental research on a plain-weave composite [52] showing the same trend. Table 3.7 listed the test data, in which h stands for the thickness of the UC, and CV denotes the coefficient of variation.

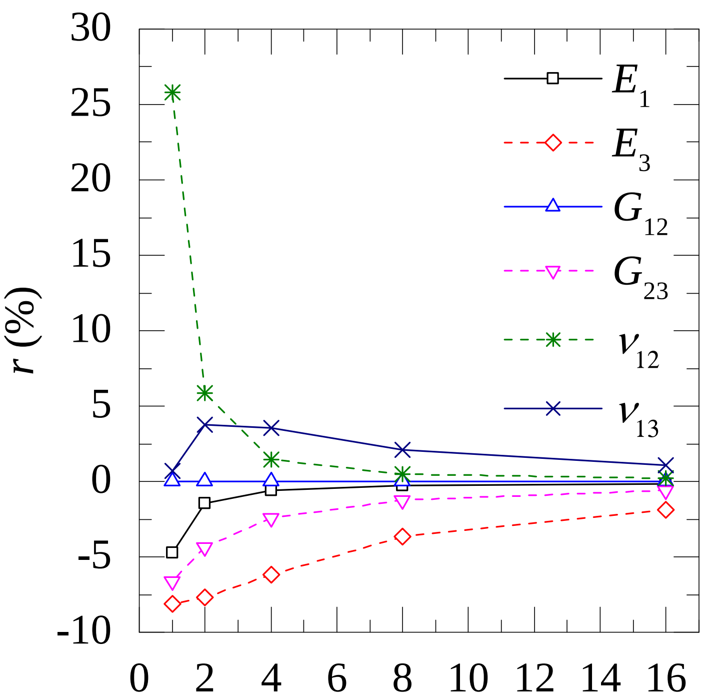

Fig. 3.7. Convergence of effective properties with respect to the number of layers through the thickness

Symmetric model where every second ply is shifted to half period in warp direction is also considered to account for the influence of phase shift of the adjacent layers.

Table 3.7.
Experimental Properties of Carbon/Epoxy Plain Weave Composites.

Number of plies	h/a_w	Fiber VOF	E_1 (GPa)	CV(%)	G_{12} (GPa)	ν_{12}
1	0.098	0.58	48.3	4.75	5.41	0.062
8	0.096	0.58	63.1	1.30	5.56	0.053

The results show a negligible difference in the effective properties for this composite model.

However, this result does not mean the inter-ply shifting is not important. Implementing this method, the inter-ply shifting of a four-ply balanced 2/2 twill woven composite has been studied in [161]. As shown in Fig. 3.8, four different inter-ply shift configurations are considered, including 'periodic' which has no shift between ply, 'symmetric' in which alternate plies are shifted by half of the unit cell size, 'step' in which alternate plies are shifted by a quarter of the unit cell size in the warp direction, and 'stairs' in which each ply is shifted by a quarter unit in the warp direction. Using MIX001 constraints at the SG in all the configurations, it can be found that the effective properties are influenced by the different inter-ply shift configurations.

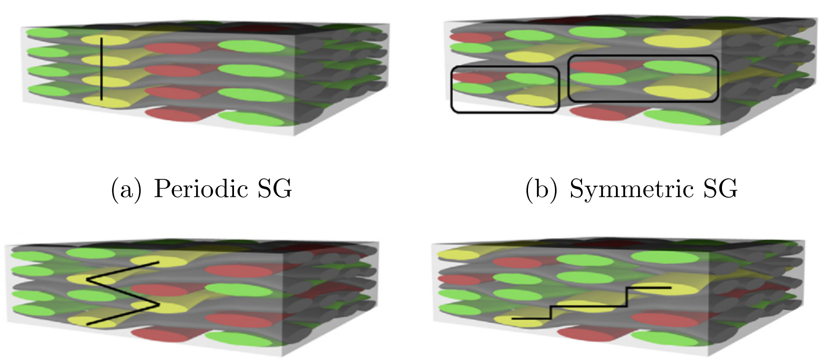

(a) Periodic SG

(b) Symmetric SG

(c) Step SG

(d) Stairs SG

Fig. 3.8. SGs for a four-ply balanced 2/2 twill woven composites with different inter-ply shifts. [161]

Table 3.8.
Difference of effective properties of the 2/2 twill woven composites under different inter-ply shifts compared with the periodic configuration (in %).

Configuration	$E_1 = E_2$	E_3	G_{12}	$G_{13} = G_{23}$	ν_{12}	$\nu_{13} = \nu_{23}$
Symmetric	4.86	-0.53	-0.38	2.56	-40.74	4.93
Step	2.53	-0.13	-0.15	1.47	-20.37	2.47
Stairs	4.95	-0.04	-0.18	1.99	-39.81	4.71

The results from [161] are re-analyzed in Table 3.8. Note in this table, the difference are calculated based on the periodic configuration. It can be seen that the influence of inter-ply shift to the E_3 and G_{12} is negligible. For the symmetric and stairs configuration, an increase of about 5% in $E_1 = E_2$ and a significant decrease of ν_{12} is observed due to the inter-ply shift. However, the influence of inter-ply shift for the step configuration is not as significant as the other configurations. Therefore, the inter-ply shift need to be taken into account for accurate analysis of textile composites.

3.4.4 3D Orthogonal Interlock Woven Composite

To demonstrate the potential usage of the proposed theory in practice, a realistic 3D orthogonal interlock composite structure is studied under two loading cases. The composite structure is constructed by repeating the microstructure shown at the left of Fig. 3.9 only in the in-plane direction, which is the SG. The SG can be constructed by stacking the microstructure at the right of Fig. 3.9 six times in the thickness direction, but at the top layer a horizontal portion of z-tow is added. Hence only in-plane periodicity is preserved, PBCs in the thickness direction on the top and bottom surfaces should not be used. The material properties of constituents are listed in Table 3.9.

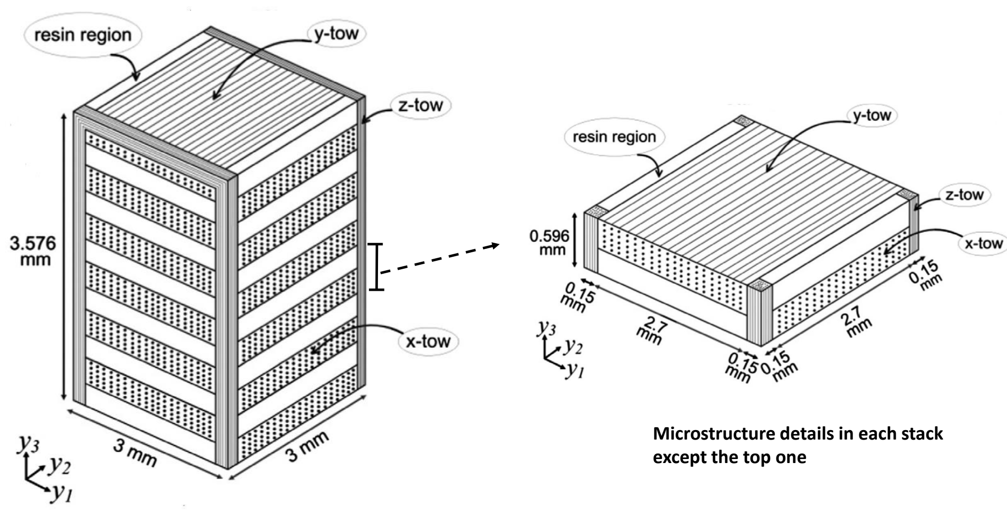

Fig. 3.9. SG of the orthogonal interlock composites (cited from Ref. [162])

Table 3.9.
Material properties of the orthogonal interlock composites.

Properties	X-tow	Y-tow	Z-tow	Resin region
E_1 (GPa)	122.55	7.13	4.96	3.40
E_2 (GPa)	7.13	122.55	4.96	3.40
E_3 (GPa)	7.13	7.13	148.70	3.40
G_{12} (GPa)	3.25	3.25	2.45	1.26
G_{31} (GPa)	3.25	2.53	3.21	1.26
G_{23} (GPa)	2.53	3.25	3.21	1.26
ν_{12}	0.263	0.015	0.476	0.35
ν_{31}	0.015	0.414	0.335	0.35
ν_{23}	0.414	0.263	0.011	0.35

To deal with this partial periodicity, Nasution [162] studied this composite structure by asymptotic expansion homogenization method, predicted the lamina constants

$(E_1, E_2, G_{12}, \nu_{12})$ of the composite structure and compared them with that obtained from homogenization implementing PBCs. Furthermore, local stress fields obtained from biaxial tensile loading are recovered but not compared with direct FEA results in [162]. According to [162], free traction must be ensured at the top and bottom surfaces as this is what was assumed in the derivation of [162]. Applying the present theory for this specific case, a good choice of constraints is MIX001, in which periodic constraints applied to the surfaces of SG normal to the micro y_1 and y_2 directions in addition to the necessary constraints in Eq. (3.7). In Table 3.10, the 3D effective properties (E_1, E_2, E_3, G_{23}, G_{13}, G_{12}, ν_{23}, ν_{13}, ν_{12}) predicted with this set of constraints are presented and compared with those calculated by applying PBCs to all three directions. Both sets of effective properties are calculated using the same mesh with global mesh size of 0.15 mm using SwiftComp. It is shown the major differences are in the properties (E_3, ν_{23} , ν_{13}) which are related to the y_3 direction, with the difference ratio smaller than 5%. This implies that the finite dimension effect is not significant for the effective properties of this type of material system.

Table 3.10.
Comparison of effective properties of woven composite.

Properties	MIX001	PBCs	Diff % (based on MIX001)
E_1 (GPa)	59.592	59.641	0.08
E_2 (GPa)	57.072	57.445	0.65
E_3 (GPa)	8.574	8.921	4.04
G_{12} (GPa)	2.974	2.980	0.20
G_{13} (GPa)	2.658	2.662	0.16
G_{23} (GPa)	2.652	2.657	0.15
ν_{12}	0.0336	0.0342	1.99
ν_{13}	0.3662	0.3523	-3.78
ν_{23}	0.3699	0.3549	-4.05

Next, local stresses are studied by dehomogenization and compared with the 3D FEA results. To perform dehomogenization, a 3D structural analysis using 3D elements with obtained effective material properties is carried out, from which the global strain $\bar{\epsilon}$ is obtained and then used in dehomogenization. Local stresses from dehomogenization using constraints MIX001 and PBCs are also compared to show the capability of the current theory. The first case has the same configuration as the biaxial tension loading case in [162]. The plate structure has a dimension of $75 \times 30 \times 3.576$ mm^3, which contains 25 SGs along y_1 and 5 SGs along y_2. The model configuration is shown in Fig. 3.10.

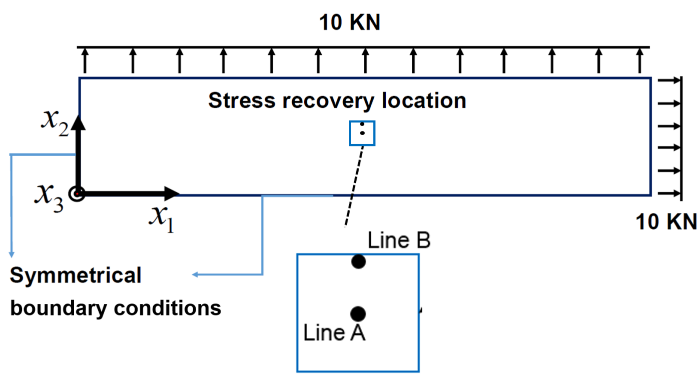

Fig. 3.10. Configuration of the 3D orthogonal interlock composite plate under biaxial tension.

Dehomogenization is performed at the SG located at the center of the structure. The stress distributions on the sampling paths Line A and Line B shown in Fig. 3.10 are investigated. The macro coordinates (x_1, x_2) of the two paths A and B are (37.5, 7.5) and (37.5, 8.925) respectively. From the bottom surface to top surface, at Line A the material constituents are [x-tow/y-tow]$_6$, while at Line B are [(resin/y-tow)$_5$/resin/$\frac{1}{2}$y-tow/$\frac{1}{2}$z-tow], where the number in the subscript denotes number of times the layup structure in ( ) repeated it self, $\frac{1}{2}$ denotes the thickness of this layer is half of the thickness of the microstructure shown in the right of Fig. 3.9. At Line A, the alternating x-tow and y-tow are the same transverse isotropic material with different in-plane tow directions, therefore the same material properties are seen in the thickness direction.

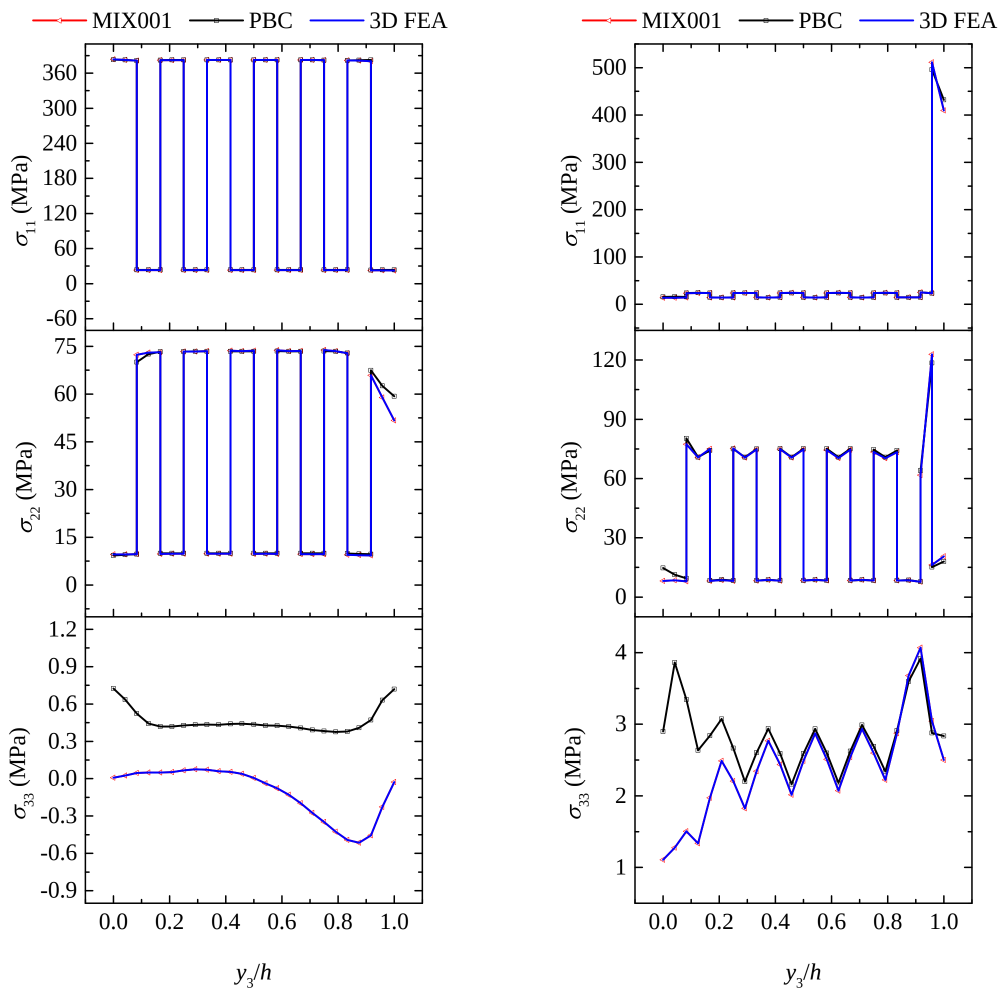

(a) Along line A

(b) Along line B

Fig. 3.11. Comparison of normal stress distributions through the normalized thickness under biaxial tension.

The stress components along the two paths through the thickness of the plate structure are compared in Fig. 3.11(a), showing only the significant components. It is observed that at Line A, σ_{11} and σ_{22} from all the three models agree very well, except at the top and bottom surfaces. However, σ_{33} from using PBCs and MIX001 are different both in pattern and magnitude. At Line A, σ_{33} is mostly under compression from the MSG model with MIX001 constraints, but is under tension from using PBCs. At Line B, a much larger σ_{33} from using PBCs is seen at the bottom surface, because that the PBCs constrain the stiff z-tow at the top surface and soft resin at bottom surface together which make the resin at the bottom bear loads at the same magnitude. The stress distribution at Line A and Line B have very different pattern due to the difference of the material arrangement along the paths.

The second case is under a uniform compression loading 1 MPa at the top and bottom surfaces in the thickness direction. The detailed settings of the second loading cases are shown in Fig. 3.12. Stresses at Line A (37.5, -7.5) and Line B (37.5, -6.075) are compared in Fig. 3.13. In this loading case, compare the results from using MIX001 and PBCs, σ_{11} and σ_{22} at Line A and Line B both display difference through the thickness. At Line B, the materials at the top and bottom surfaces are z-tow and resin respectively. Similar with the biaxial loading case, σ_{33} from using MIX001 and PBCs have significant differences. It is noted that when MIX001 is applied, the top and bottom surface have the same σ_{33} magnitude of -1.0 MPa the same as the applied pressure.

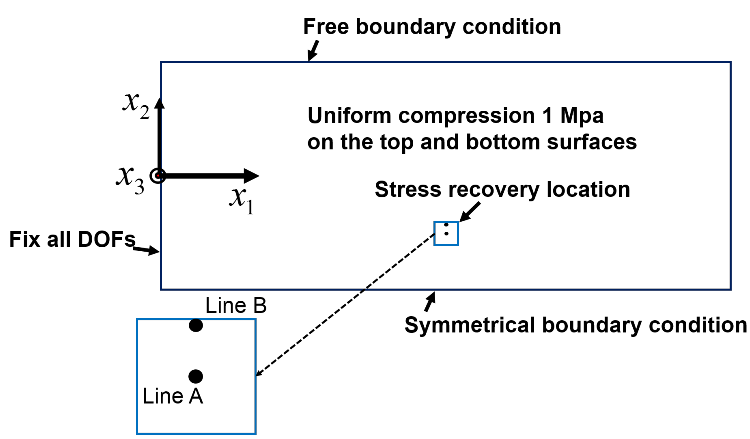

Fig. 3.12. Configuration of the 3D orthogonal interlock composite plate under compression.

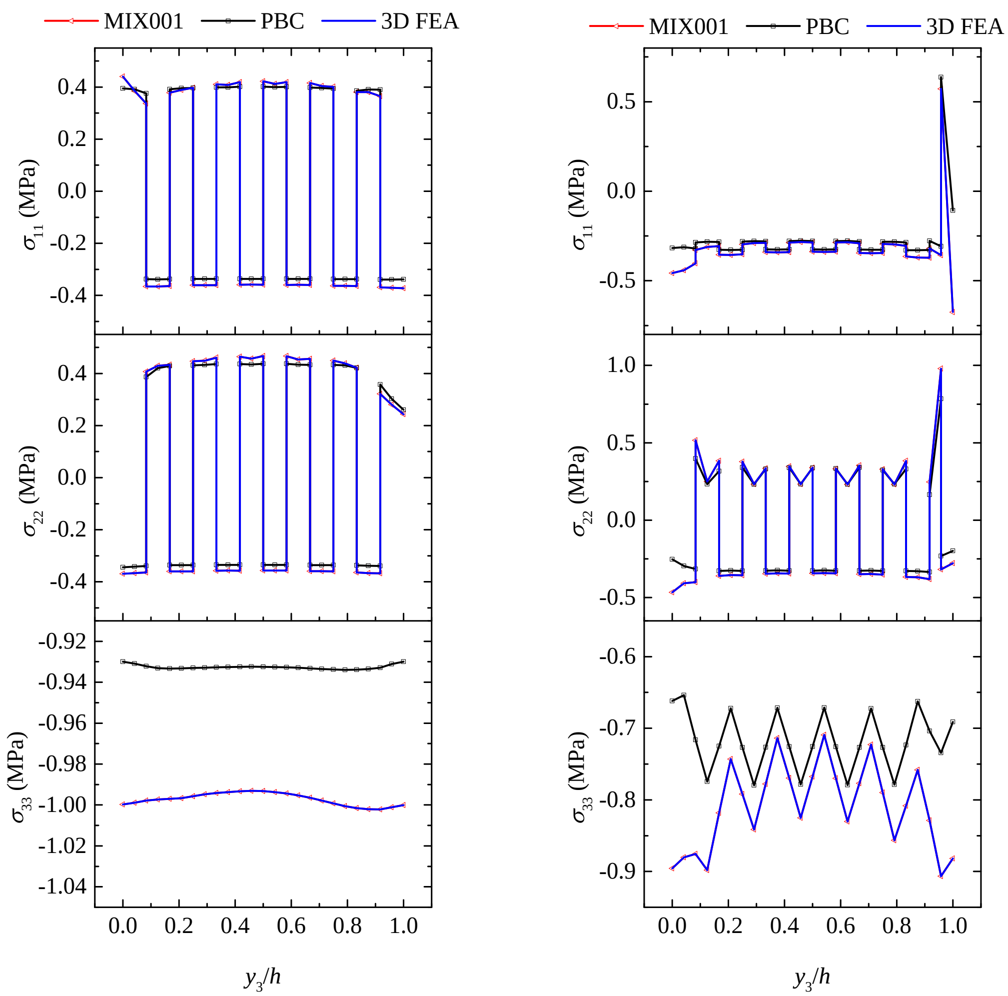

(a) Along line A (b) Along line B

Fig. 3.13. Comparison of normal stress distribution through the normalized thickness under compression.

It is shown that for such highly heterogeneous composite structure, the present theory with MIX001 constraints can achieve excellent agreement with 3D FEA. Particularly, σ_{33} at both paths predicted by MIX001 constraints show much better correspondence compared with those predicted by PBCs. However while the 3D FEA took 75 minutes with 20 CPUs, the homogenization and dehomogenization process of the current case cost only 80 seconds with only 1 CPU. The present theory is clearly more efficient without losing noticeable accuracy. Note this structure can also be analyzed as a plate with the corresponding constitutive relations obtained using a plate SG in SwiftComp, which is studied in [163]. The improvement brought by implementation of the B-bar method can also be shown using this example. The results in this example are obtained from using 8-noded brick elements with B-bar method as the integration technique. The 3D FEA implement the same element type, that is C3D8. Perfect agreement between the results from SwiftComp and ABAQUS is seen from the Figs. 3.11, 3.13. When the standard integration technique is used, the stress distribution can have this zig-zag shape because of the volumetric locking as shown in Fig. 3.14.

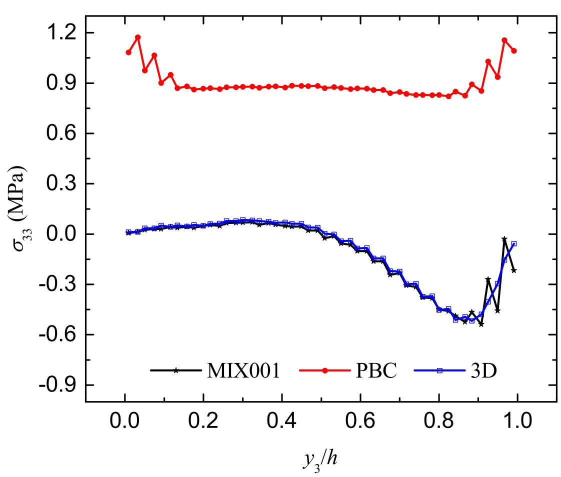

Fig. 3.14. σ_{33} along Line A subjected to biaxial tension.

3.4.5 Short Fiber Reinforced Composites

In the previous examples, MSG is applied to 3D heterogeneous structures with boundary effect originated from the ambiguous length scale separation. In this example, MSG is implemented in a randomly distributed short fiber reinforced composites that full PBCs on all the boundary surfaces of the RVE should be applied. The microstructure is from [164], as shown in Fig. 3.15. In the model, the fiber materials has $E_f = 450$ GPa, $\nu_f = 0.17$, while the matrix has $E_m = 45$ GPa, $\nu_m = 0.18$. The fiber volume ratio is 7.857%.

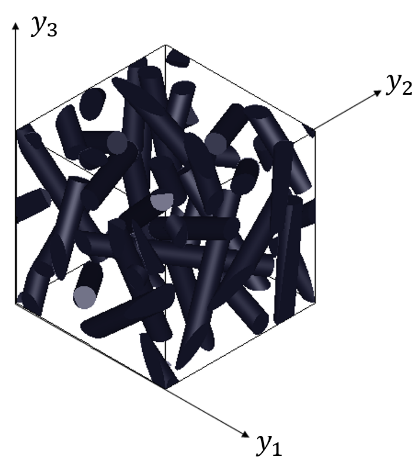

Fig. 3.15. SG of the short fiber reinforced composite.

The microstructure has been purposely created to be periodic in order to take advantage of using PBCs. However, it is very difficult to directly create periodic mesh for this complex microstructure while maintaining high element quality. If there is no strict restriction for periodic mesh, high quality mesh can be easily generated without special techniques, including some node pairs on the opposing boundary surfaces which can be exploited using the present theory. In the short fiber reinforced composite SG model, 356 out of 2255, 373 out of 2590, and 382 out of 2572 nodes on the y_1, y_2, and y_3 boundary surfaces respectively have corresponding nodes on the opposing boundary surfaces. The whole model contains 612,547 linear tetrahedral elements and

108,247 nodes. The effective properties are calculated using KUBCs, SUBCs and the volume integral constraints in Eq. (3.7) with the applicable PBCs, denoted as 'partial PBCs'. This model is also analyzed using the micromechanics plugin of ABAQUS, in which the PBCs are applied through surface-to-surface constraints: first 2D elements are generated on three boundary surfaces(surface-N) based on the 3D elements of the microstructure and moved to the position of the opposing surfaces(surface-P), therefore the node arrangement of the newly created 2D element surfaces(surface-N') is the same as surface-N. Then surface-N'are tied to surface-P, and PBCs are applied between the node pairs on surface-N and surface-N'. In Table 3.11, it is shown that the Young's moduli and shear moduli from using 'partial PBCs' lie between those obtained from using PBCs and SUBCs, but still close to those obtained from using PBCs. The local field predictions in Fig. 3.16 also show that the current method can give reasonable results while taking least effort to deal with the mesh and the boundary conditions.

Table 3.11.
Comparison of effective properties of a randomly distributed short fiber reinforced composite.

Properties	KUBCs	SUBCs	partial PBCs	PBCs(ABAQUS)
E_1 (GPa)	59.4	53.4	54.6	55.3
E_2 (GPa)	61.7	55.1	56.7	57.5
E_3 (GPa)	58.1	52.9	53.9	54.5
G_{12} (GPa)	25.6	23.0	23.6	23.9
G_{13} (GPa)	25.1	22.6	23.2	23.6
G_{23} (GPa)	25.2	22.7	23.3	23.7
ν_{12}	0.175	0.179	0.181	0.180
ν_{13}	0.182	0.184	0.188	0.189
ν_{23}	0.179	0.182	0.186	0.187

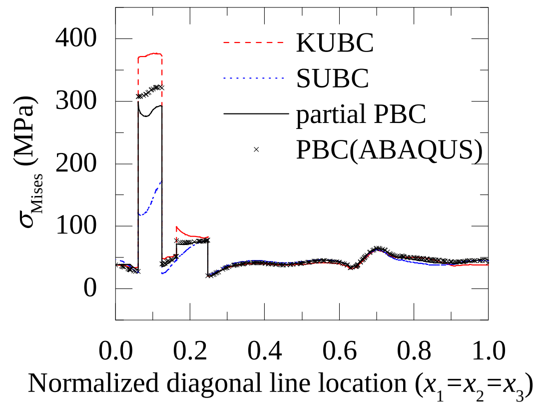

(a) Apply macro strain $\epsilon_{11} = 0.1\%$

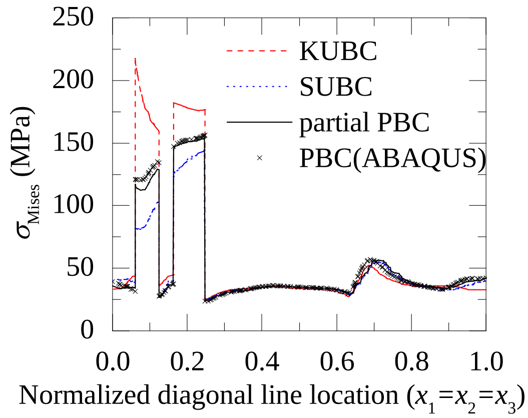

(b) Apply macro strain $2\epsilon_{12} = 0.1\%$

Fig. 3.16. Comparison of Mises stress distribution through the normalized diagonal line connecting point (0,0,0) and (l, l, l) with l denotes the dimension of the cubic SG.

Fig. 3.16 shows the Mises stress extracted at the diagonal line connecting point (0,0,0) and (l,l,l) under different macroscopic strains $\bar{\epsilon}_{11}$ and $2\bar{\epsilon}_{12}$, where l denoting the dimension of the cubic SG. In the Fig. 3.16, the horizontal axis is the location on the diagonal line and normalized by the length of the diagonal line. Subjected to the four different boundary conditions, it is observed that stress are concentrated at the material interfaces between the short fibers and matrix, especially at the ends of the short fiber. When the $2\bar{\epsilon}_{12}$ is applied, KUBCs predicts stress 'peaks' closing to the boundary surface, that is much higher than using the other boundary conditions. SUBCs model has the minimum kinematic constraint and the stress field at the interfaces are less concentrated. With the 'partial PBCs' applied, the maximum Mises stress along the diagonal line are between the results obtained from KUBCs and SUBCs, and close to the results from using PBCs exerted by surface-to-surface constraint. It is shown this method can give reasonable results while taking least effort to deal with the mesh and the boundary conditions of complicated microstructures. However, for better convergence it is recommended to include as many periodic node pairs as possible on the boundary surfaces, especially at the edges that define the SG geometry.

3.4.6 Porous Materials

For porous materials, the constraints in Eq. (3.8) should be implemented. Two examples are used to show the validity of this set of constraints.

The first example is a 3D SG with a spherical void of volume fraction 0.268 (Fig. 3.17) at the center. The material of the SG is orthotropic, and has $E_1 = 50.00$ GPa, $E_2 = E_3 = 15.20$ GPa, $G_{12} = G_{13} = 4.70$ GPa, $\nu_{12} = \nu_{13} = 0.254$, $\nu_{23} = 0.428$. The mesh size is 0.1 of the length of the cube. Using constraints of Eq. (3.8), the effective properties are $E_1 = 15.58$ GPa, $E_2 = E_3 = 7.15$ GPa, $G_{12} = G_{13} = 2.48$ GPa, $\nu_{12} = \nu_{13} = 0.316$, $\nu_{23} = 0.392$), which are exactly the same with the results obtained from using SUBC in RVE analysis with a very weak dummy material ($E_1 = 0.005$GPa, $\nu = 0.001$) filled in the void.

The second example is a SG of a heat exchange structure shown in Fig. 3.18. The materials used in the model are $E = 20.6$ GPa, $\nu = 0.3$ (Green) and $E = 20.7$ GPa, $\nu = 0.31$(yellow). Here we consider the structure is only periodic in the oy_1y_2 plane (denoted as oxy in the Fig. 3.18), therefore constraint setting MIX001 is used. The obtained effective properties are compared in Table 3.12. When a

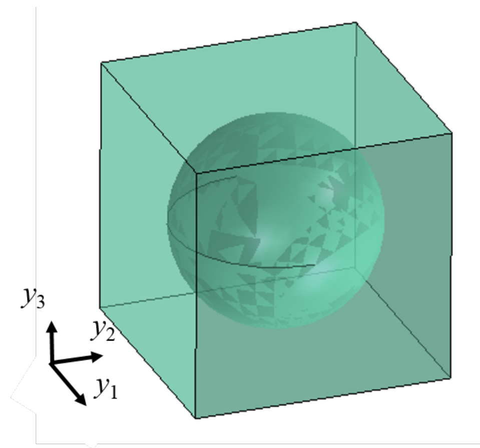

Fig. 3.17. SG of the material with a void

weak dummy material ($E_1 = 0.005$GPa, $\nu = 0.001$) is substituted to the void part, the effective properties obtained are the same as those shown in Table 3.12. From the comparison, it is clear that the mechanical properties E_3 and ν_{23} have apparent difference. Therefore if a macroscopic 3D model is used for simulation, size effect must be taken into account and applying PBCs is not appropriate in this case. In this example, the constraints MIX001 should be applied in the surface integral form Eq. (3.8), because of the existence of the void part as discussed in section 3.2.

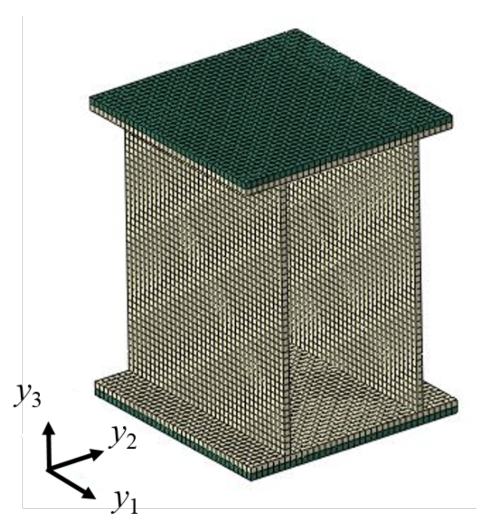

Fig. 3.18. SG of heat exchange structure

Table 3.12.
Comparison of effective properties.

Properties	MIX001	PBC	Diff % (based on MIX001)
E_1 (GPa)	2.857	2.857	-0.003
E_2 (GPa)	1.876	1.876	0.040
E_3 (GPa)	0.517	1.289	149.3
G_{12} (GPa)	0.695	0.695	0.005
G_{13} (GPa)	0.458	0.469	2.490
G_{23} (GPa)	0.001	0.001	7.069
ν_{12}	0.305	0.305	0.000
ν_{13}	0.310	0.310	-0.028
ν_{23}	-0.006	-0.0218	288.3

3.5 Summary

This chapter first developed a general micromechanics model for aperiodic 3D solids through extending MSG. The model is based on the concept of SG through minimizing the energy of the original heterogeneous materials. As no boundary conditions are involved except the constraints to ensure kinematics equivalency between the heterogeneous material and the equivalent homogeneous material, the theory can be applied to SG of arbitrary shape. In addition, this theory provides a general framework for homogenization and dehomogenization of heterogeneous materials. It can handle aperiodic materials, materials with partial periodicity, or material with complete periodicity. It can also handle porous materials if the voids have no intersection with the boundary surfaces which normal to the directions without periodicity. SG can use the lowest dimension to describe the heterogeneity. This theory has been implemented into the computer code SwiftComp using the finite element method. By using realistic numerical examples, it is demonstrated that the new theory shows good accuracy compared with the 3D direct FEA with meshing all the microstructural details.

4. MSG-BASED FREE-EDGE STRESS ANALYSIS

In most of the available methods for free-edge stress problems, a long strip of a laminate is chosen as the analysis domain. This is based on two reasons. First, by choosing a long strip, the boundary effects can be neglected at the two ends; second, the free-edge stresses are localized within a narrow boundary region. Therefore a long strip of composite laminate is enough to capture the free-edge stresses with the minimum computation cost. In this chapter, free-edge problem is solved by MSG beam analysis effectively using the cross section as the SG.

First the formulation of MSG beam analysis is presented, including the generalized Euler-Bernoulli beam (GEB) and the generalized Timoshenko beam (GTB) models [137, 165]. Although for free-edge stress analysis of composite laminates, the SG is the cross section of the beam-like structure, the provided method can be utilized for beam-like structures composed of periodically repeated SGs of spanwise heterogeneity. Therefore, this method can be implemented in more complicated periodic beam-like structures, not limited to laminates. Then the MSG beam cross section analysis is reformulated for the free-edge problem. The capability and the limitation of this method are explained. Last, the MSG GTB model is implemented into SwiftComp. The free-edge stress induced by shear forces is focused. Two cross sectional geometry are analyzed, including a traditionally studied rectangular cross section and a curved cross section. The results are compared with that obtained from 3D FEA. The improvement of the GTB model compared with the GEB model of MSG is also studied to show the applicability of the two models in free-edge stress analysis.

4.1 MSG for Heterogeneous Beam-like Structures

For a heterogeneous beam-like structures composed of periodically repeated SGs, MSG decomposes the original 3D problem into a linear 3D micro-mechanical analysis of SG and a nonlinear 1D macroscopic beam analysis based on VAM [146]. First the displacement and the strain field of the original structure are expressed in terms of those of the 1D beam model and fluctuating functions. Then the 3D variational statement governing the original structure is reduced into the 1D variational statement for the 1D beam analysis, which is called dimensional reduction. The dimensional reduction from the original 3D statement to the 1D beam statement can be done approximately based on VAM. According to the refinement order of the governing statement, the 1D beam model can be a GEB model in which the zeroth order approximation of energy statement is considered, or a GTB model in which a second-order approximation is considered. In the GTB model, the transverse shear deformation can be captured more accurately. Both beam models were initially developed by Hodges and Yu [137] for composite laminated beams. Then both models have been generated to beams with spanwise periodicity by Yu and Lee [165, 166]. Yu unified the multiscale constitutive modeling of composite structures in MSG, with the GEB model reformulated in the new framework of MSG [24, 133]. In this work, the GTB model is reformulated in the framework of MSG and implemented in the code SwiftComp.

4.1.1 Kinematics

For beam-like structures, we can use x_1 only as the macro coordinate to denote the reference line of the beam model. In the same way of the 3D heterogeneous materials in Chapter 3, we introduce the micro coordinates $y_i, i = 1, 2, 3$ to describe the SG. For a 3D SG, y_1, y_2, y_3 are needed, for a 2D SG y_2, y_3 are needed. Although in the free-edge problem, only the cross section of a laminate strip need to be considered, the more general 3D SG will be considered in the formulation of this section, which can be easily reduced for the 2D SG case for the free-edge problem.

As shown in Fig. 2.4, the original periodic heterogeneous beam-like structures can be described by a SG repeated itself along a reference line. The reference line $\boldsymbol{r}_o$ is denoted using the arc-length coordinate x_1. As shown in Fig. 4.1, local orthonormal reference triad $\boldsymbol{b}_i$ is introduced along the reference line so that $\boldsymbol{b}_i$ is tangent to x_i. By this definition $\boldsymbol{b}_1 = \frac{\partial \boldsymbol{r}_o}{\partial x_1}$, and $\boldsymbol{b}_i$ may depend on x_1 because of the presence of initial curvatures and twist. The location of any material point in the undeformed structure is

$$\boldsymbol{r}(x_1, y_\alpha) = \boldsymbol{r}_o(x_1) + \varepsilon y_\alpha \boldsymbol{b}_\alpha(x_k) \tag{4.1}$$

where $\alpha = 2, 3$.

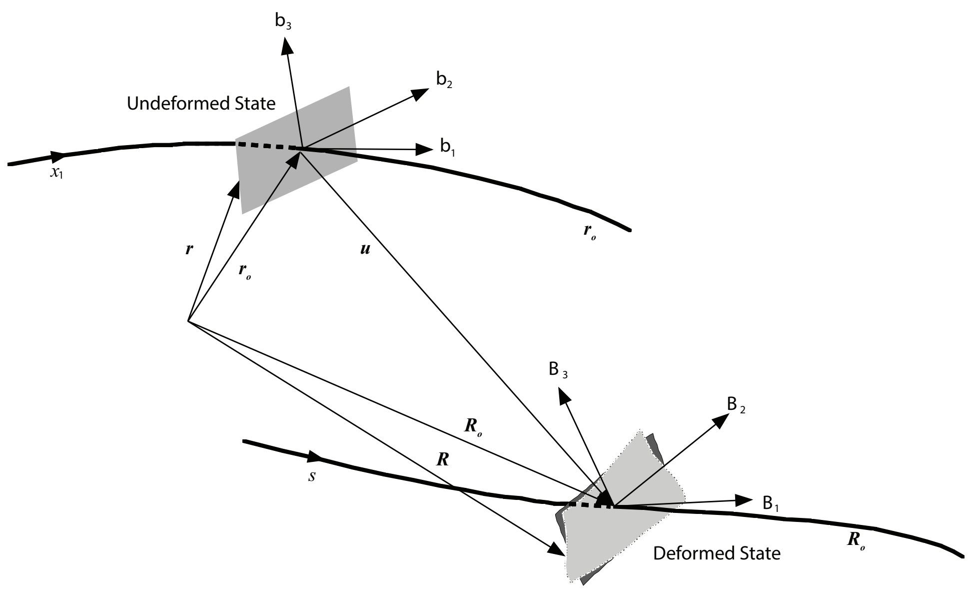

Fig. 4.1. Deformation of a typical beam structure [133].

When the beam-like structure deforms, it is convenient to define a new triad $\boldsymbol{B}_i$ to describe the deformed state, which can be related to $\boldsymbol{b}_i$ by a rotation tensor $\boldsymbol{C}^{Bb}$.

$$\boldsymbol{B}_i = \boldsymbol{C}^{Bb} \cdot \boldsymbol{b}_i \tag{4.2}$$

The position vector of an arbitrary point in the deformed state is denoted by $\boldsymbol{R}$ and can now be expressed as

$$\boldsymbol{R}(x_1, y_1, y_2, y_3) = \boldsymbol{R}_o(x_1) + \varepsilon y_\alpha \boldsymbol{B}_\alpha(x_1) + \varepsilon \tilde{w}_i(x_1, y_1, y_2, y_3)\boldsymbol{B}_i \tag{4.3}$$

where $\boldsymbol{R}_o$ denotes the position vector of the deformed beam model, and $\varepsilon\tilde{w}_i$ are fluctuating functions introduced to accommodate all possible deformations other than those described by $\boldsymbol{R}_o$ and $\boldsymbol{B}_i$.

It is noted that $\boldsymbol{B}_1$ is not tangent to x_1 if transverse shear deformations are considered. It is not convenient to reduce a 3D model to a 1D beam model when the transverse shear deformation is considered explicitly in the beam model. Therefore, another triad $\boldsymbol{T}_i$ associated with the deformed beam is introduced. As shown in the Fig. 4.2, $\boldsymbol{T}_1$ is tangent to the deformed beam reference line, the vectors $\boldsymbol{T}_\alpha$ are then determined by a rotation about $\boldsymbol{T}_1$. That is, in $\boldsymbol{B}_i$, the transverse shear strain $2\gamma_{1\alpha}$ corresponding to a GTB model could be expressed explicitly, while in $\boldsymbol{T}_i$, the transverse shear deformation is considered in the fluctuating functions. The difference in the orientation of $\boldsymbol{T}_i$ and $\boldsymbol{B}_i$ is due to the small rotations $2\gamma_{1\alpha}$ associated with the transverse shear deformation of the beam model. Based on the small strain assumption of $2\gamma_{1\alpha} \ll 1$, which is adequate for developing nonlinear beam theories, the relationship between these two sets of basis vectors can be expressed as:

$$\begin{Bmatrix} \boldsymbol{B}_1 \\ \boldsymbol{B}_2 \\ \boldsymbol{B}_3 \end{Bmatrix} = \begin{bmatrix} 1 & -2\gamma_{12} & -2\gamma_{13} \\ 2\gamma_{12} & 1 & 0 \\ 2\gamma_{13} & 0 & 1 \end{bmatrix} \begin{Bmatrix} \boldsymbol{T}_1 \\ \boldsymbol{T}_2 \\ \boldsymbol{T}_3 \end{Bmatrix} \tag{4.4}$$

In the $\boldsymbol{T}_i$ basis, the position vector of any particle in the deformed state can be expressed as:

$$\boldsymbol{R}(x_1, y_1, y_2, y_3) = \boldsymbol{R}_o(x_1) + \varepsilon y_\alpha \boldsymbol{T}_\alpha(x_1) + \varepsilon w_i(x_1, y_1, y_2, y_3)\boldsymbol{T}_i \tag{4.5}$$

where $w_i(x_1, x_2, x_3)$ are fluctuating functions used to describe deformations which are not covered by the deformation of the reference line $\boldsymbol{u} = \boldsymbol{R}_o(x_1) - \boldsymbol{r}_o(x_1)$ and $\boldsymbol{T}_i$. It should be emphasized that the fluctuating functions w_i in the $\boldsymbol{T}_i$ basis (Eq. (4.5)) and the fluctuating functions $\tilde{w}_i$ in the $\boldsymbol{B}_i$ basis (Eq. (4.3)) are not the same.

In order to conduct the dimensional reduction conveniently, the basis $\boldsymbol{T}_i$ is used. Since $\boldsymbol{R}$ now is expressed in terms of $(\boldsymbol{R}_o, \boldsymbol{T}_i, w_i)$ in Eq. (4.5), resulting in six times

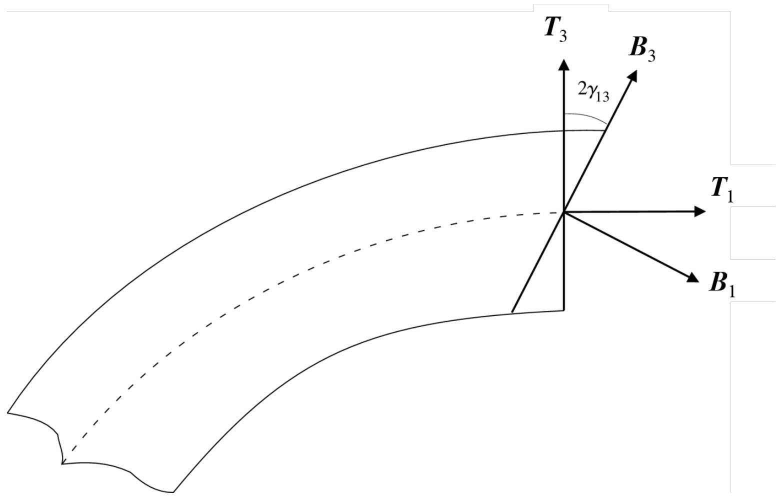

Fig. 4.2. Coordinate systems used for transverse shear formulation [137].

redundancy, six constraints must be introduced to ensure a unique mapping. First, to remove the rigid body translation, we can naturally define

$$\boldsymbol{R}_o = \langle\langle \boldsymbol{R} \rangle\rangle - \langle\langle \varepsilon y_\alpha \rangle\rangle \, \boldsymbol{T}_\alpha(x_1) \tag{4.6}$$

where $\langle\langle \cdot \rangle\rangle$ means volume averaging over the SG. If y_α is chosen such that $\langle\langle \varepsilon y_\alpha \rangle\rangle = 0$, $\boldsymbol{R}_o$ is defined as the average of the position vector of the original structure. Then Eq. (4.5) implies the following three constraints on the fluctuating functions:

$$\langle\langle w_i \rangle\rangle = 0 \tag{4.7}$$

In addition, the new orthonormal triad $\boldsymbol{T}_i$ is defined uniquely by the following three constraints

$$\boldsymbol{T}_2 \cdot \frac{\partial \boldsymbol{R}_o}{\partial x_1} = 0, \quad \boldsymbol{T}_3 \cdot \frac{\partial \boldsymbol{R}_o}{\partial x_1} = 0, \quad \boldsymbol{T}_3 \cdot \frac{\partial \boldsymbol{R}_o}{\partial x_2} - \boldsymbol{T}_2 \cdot \frac{\partial \boldsymbol{R}_o}{\partial x_3} = 0 \tag{4.8}$$

where the first two constraints implying that $\boldsymbol{T}_1$ is chosen to be tangent to the reference line of the deformed beam. It is noteworthy that this choice is not the same as the well-known Euler-Bernoulli assumption since the present formulation can describe all deformations of the cross section through the term $w_i \boldsymbol{T_i}$ in Eq. (4.5). The third equation defines the twist angle of the macroscopic beam model [137], and can be exerted to the model by using the following constraint on the fluctuating functions

$$\left\langle\left\langle w_{2|3} - w_{3|2} \right\rangle\right\rangle = 0 \tag{4.9}$$

The four constraints of Eq. (4.7) and Eq. (4.9) can be written as

$$\left\langle\left\langle w^{\mathrm{T}} \psi \right\rangle\right\rangle = 0 \tag{4.10}$$

where $w = \lfloor w_1 \quad w_2 \quad w_2 \rfloor^{\mathrm{T}}$ and

$$\psi = \begin{bmatrix} 1 & 0 & 0 & 0 \\ 0 & 1 & 0 & -\frac{\partial}{\partial y_3} \\ 0 & 0 & 1 & \frac{\partial}{\partial y_2} \end{bmatrix} \tag{4.11}$$

At last, for 3D SGs, PBCs on fluctuating functions need to be implemented on the periodic boundaries A_1, where A_1 denotes the boundaries normal to the x_1 axis.

$$w_i(x_1, -\frac{\omega}{2}, y_2, y_3) = w_i(x_1, \frac{\omega}{2}, y_2, y_3) \tag{4.12}$$

where ω is the length along y1 direction that occupied by the 3D SG.

Beam strain definition

In order to express the 3D strain field of the original structure using the 1D generalized strain measures of the beam, proper definitions of the 1D generalized strain measures of the beam are first defined. According to the geometrically-exact framework of Hodges [167], the 1D generalized strains of the beam model is given in the form of

$$\bar{\epsilon} = \lfloor \bar{\gamma}_{11} \quad \bar{\kappa}_1 \quad \bar{\kappa}_2 \quad \bar{\kappa}_3 \rfloor^{\mathrm{T}} \tag{4.13}$$

with $\bar{\gamma}_{11}$ denoting the extensional strain, $\bar{\kappa}_1$ the twist, $\bar{\kappa}_2$ and $\bar{\kappa}_3$ the bending curvatures. They are defined by

$$\frac{\partial \boldsymbol{R}_o}{\partial x_1} = (1 + \bar{\gamma}_{11})\boldsymbol{T}_1 \tag{4.14}$$

$$\frac{\partial \boldsymbol{T}_i}{\partial x_1} = (\bar{\kappa}_j + k_j)\boldsymbol{T}_j \times \boldsymbol{T}_i \equiv \bar{\boldsymbol{K}} \times \boldsymbol{T}_i \tag{4.15}$$

where k_1 is the initial twist curvature and k_α are the initial bending curvatures such that

$$\frac{\partial \boldsymbol{b}_i}{\partial x_1} = k_j\, \boldsymbol{b}_j \times \boldsymbol{b}_i \equiv \boldsymbol{k} \times \boldsymbol{b}_i \tag{4.16}$$

and $\bar{\boldsymbol{K}}$ is the curvature of the deformed reference line.

$$\bar{\boldsymbol{K}} = \lfloor \bar{\kappa}_1 + k_1 \quad \bar{\kappa}_2 + k_2 \quad \bar{\kappa}_3 + k_3 \rfloor^{\mathrm{T}} \tag{4.17}$$

Note due to the definition of the $\boldsymbol{T}_i$ triad, this definition of 1D beam strains has zero transverse shear strains, that is $2\gamma_{12} = 2\gamma_{13} = 0$, and thus inherently the resulted constitutive relation of the beam model is not related with the transverse shear strains.

In order to obtain a constitutive relation that consider the transverse shear strains explicitly using the GTB model, the set of 1D strains associated with the $\boldsymbol{B}_i$ basis are introduced, denoted as $\epsilon = \lfloor \gamma_{11} \quad \kappa_1 \quad \kappa_2 \quad \kappa_3 \rfloor^{\mathrm{T}}$ and $\gamma_s = \lfloor 2\gamma_{12} \quad 2\gamma_{13} \rfloor^{\mathrm{T}}$. They are defined as

$$\begin{aligned} &\gamma_{11}\boldsymbol{b}_1 + 2\gamma_{12}\boldsymbol{b}_2 + 2\gamma_{13}\boldsymbol{b}_3 = \boldsymbol{C}^{bB} \cdot \frac{\partial \boldsymbol{R}_o}{\partial x_1} - \frac{\partial \boldsymbol{r}_o}{\partial x_1} \\ &\frac{\partial \boldsymbol{B}_i}{\partial x_1} = (k_j + \kappa_j)\boldsymbol{B}_j \times \boldsymbol{B}_i \end{aligned} \tag{4.18}$$

The generalized classical strains $\bar{\epsilon}$ and the generalized Timoshenko strains (ϵ and γ_s) are related kinematically. The relationship between these two sets of strain measures is derived in [168] as

$$\bar{\epsilon} = \epsilon + H\, \gamma_s' + P\, \gamma_s \tag{4.19}$$

where $(\ )'$ denotes $\frac{\partial}{\partial x_1}$ and

$$H = \begin{bmatrix} 0 & 0 \\ 0 & 0 \\ 0 & -1 \\ 1 & 0 \end{bmatrix} \qquad P = \begin{bmatrix} 0 & 0 \\ k_2 & k_3 \\ -k_1 & 0 \\ 0 & -k_1 \end{bmatrix} \tag{4.20}$$

3D strain field

Jauman-Biot-Cauchy strain is used to describe the 3D strain field [169]. Using this strain definition, the situation that the beam is subjected to a small local rotation can be considered, that is the rotation of a material point of the original structure subtracting the rotation needed for bringing $\boldsymbol{b}_i$ to $\boldsymbol{B}_i$ is small.

$$\Gamma_{ij} = \frac{1}{2}\left(F_{ij} + F_{ji}\right) - \delta_{ij} \tag{4.21}$$

where δ_{ij} is the Kronecker symbol and F_{ij} is the mixed-basis component of the deformation gradient tensor. As shown in [24], the 3D strain field defined in Eq. (4.21) can be written in the following matrix form

$$\Gamma = \Gamma_h w + \Gamma_\epsilon \bar{\epsilon} + \varepsilon \Gamma_l w + \varepsilon \Gamma_R w \tag{4.22}$$

where $\Gamma = \lfloor \Gamma_{11} \;\; \Gamma_{22} \;\; \Gamma_{33} \;\; 2\Gamma_{23} \;\; 2\Gamma_{13} \;\; 2\Gamma_{12} \rfloor^{\mathrm{T}}$. Γ_h is an operator matrix which depends on the dimensionality of the SG. If the SG is 3D, we have

$$\Gamma_h = \begin{bmatrix} \frac{1}{\sqrt{g_1}}\frac{\partial}{\partial y_1} & 0 & 0 \\ 0 & \frac{\partial}{\partial y_2} & 0 \\ 0 & 0 & \frac{\partial}{\partial y_3} \\ 0 & \frac{\partial}{\partial y_3} & \frac{\partial}{\partial y_2} \\ \frac{\partial}{\partial y_3} & 0 & \frac{1}{\sqrt{g_1}}\frac{\partial}{\partial y_1} \\ \frac{\partial}{\partial y_2} & \frac{1}{\sqrt{g_1}}\frac{\partial}{\partial y_1} & 0 \end{bmatrix} \tag{4.23}$$

where $\sqrt{g_1} = 1 - \varepsilon y_2 k_3 + \varepsilon y_3 k_2$. If the SG is a lower-dimensional one, we just need to vanish the terms corresponding to the micro coordinates which are not used in describing the SG. For example, if the SG is 2D, we have

$$\Gamma_h = \begin{bmatrix} 0 & 0 & 0 \\ 0 & \frac{\partial}{\partial y_2} & 0 \\ 0 & 0 & \frac{\partial}{\partial y_3} \\ 0 & \frac{\partial}{\partial y_3} & \frac{\partial}{\partial y_2} \\ \frac{\partial}{\partial y_3} & 0 & 0 \\ \frac{\partial}{\partial y_2} & 0 & 0 \end{bmatrix} \tag{4.24}$$

Γ_ϵ is an operator matrix associated with the macroscopic beam strain and curvatures

$$\Gamma_\epsilon = \frac{1}{\sqrt{g_1}} \begin{bmatrix} 1 & 0 & \varepsilon y_3 & -\varepsilon y_2 \\ 0 & 0 & 0 & 0 \\ 0 & 0 & 0 & 0 \\ 0 & 0 & 0 & 0 \\ 0 & \varepsilon y_2 & 0 & 0 \\ 0 & -\varepsilon y_3 & 0 & 0 \end{bmatrix} \tag{4.25}$$

$\Gamma_l w$ denotes the part of 3D strain contributed from the fluctuating functions w that is one order higher in terms of ε.

$$\Gamma_l = \begin{bmatrix} \frac{1}{\sqrt{g_1}}\frac{\partial}{\partial x_1} & 0 & 0 \\ 0 & 0 & 0 \\ 0 & 0 & 0 \\ 0 & 0 & 0 \\ 0 & 0 & \frac{1}{\sqrt{g_1}}\frac{\partial}{\partial x_1} \\ 0 & \frac{1}{\sqrt{g_1}}\frac{\partial}{\partial x_1} & 0 \end{bmatrix} \tag{4.26}$$

Γ_R is an operator matrix existing only for those original structures featuring initial curvatures. For prismatic beams, Γ_R vanishes. Γ_R has the expression of

$$\Gamma_R = \frac{1}{\sqrt{g_1}} \begin{bmatrix} k_1\left(y_3\frac{\partial}{\partial y_2} - y_2\frac{\partial}{\partial y_3}\right) & -k_3 & k_2 \\ 0 & 0 & 0 \\ 0 & 0 & 0 \\ 0 & 0 & 0 \\ -k_2 & k_1 & k_1\left(y_3\frac{\partial}{\partial y_2} - y_2\frac{\partial}{\partial y_3}\right) \\ k_3 & k_1\left(y_3\frac{\partial}{\partial y_2} - y_2\frac{\partial}{\partial y_3}\right) & -k_1 \end{bmatrix} \tag{4.27}$$

It is noted a small parameter ε is added to the last two terms in Eq. (4.22), implicating these two terms are one order asymptotically smaller than the first two terms. The process of the asymptotic analysis is explained in details in [137].

4.1.2 Variational Statement

Considering a static problem of 3D beam-like structures made of linear elastic materials and subjected to deformation of small strain, the governing variational statement is the principle of virtual work,

$$\delta\mathcal{U} - \overline{\delta\mathcal{W}} = 0 \tag{4.28}$$

where $\mathcal{U}$ is the strain energy, and $\overline{\delta\mathcal{W}}$ is the virtual work of the original structure. The strain energy can be written as

$$\mathcal{U} \equiv \int_0^l \frac{1}{\omega} U \mathrm{d}x_1 \tag{4.29}$$

with

$$U = \frac{1}{2}\left\langle \Gamma^{\mathrm{T}} D \Gamma \right\rangle \tag{4.30}$$

where U is the strain energy of the SG. ω is the length along y_1 direction that occupied by a 3D SG, and $\omega = 1$ if a 2D SG is used. l is the total length of the beam. $\langle\cdot\rangle = \int \cdot \sqrt{g_1}\mathrm{d}\Omega$, which means a weighted integration over the SG. The matrix D is the 6×6 stiffness matrix of the elastic material properties.

Considering loads of tractions and body forces on a 3D continuum, the virtual work done can be calculated as

$$\begin{aligned} \overline{\delta\mathcal{W}} = &\int_0^l \frac{1}{\omega}\left(\langle \boldsymbol{p} \cdot \delta\boldsymbol{R} \rangle + \oint_{\partial\Omega} \boldsymbol{Q} \cdot \delta\boldsymbol{R}\sqrt{c}\, \mathrm{d}s \right)\, \mathrm{d}x_1 \\ &+ \langle \boldsymbol{Q} \cdot \delta\boldsymbol{R} \rangle\, |_{x_1=0} + \langle \boldsymbol{Q} \cdot \delta\boldsymbol{R} \rangle\, |_{x_1=l} \end{aligned} \tag{4.31}$$

where $\sqrt{c} = \sqrt{g_1 + \left(y_2 \frac{\mathrm{d}y_2}{\mathrm{d}s} + y_3 \frac{\mathrm{d}y_3}{\mathrm{d}s}\right)^2 k_1^2}$, $\mathrm{d}s$ is the differential arc length along the boundary curve, $\partial\Omega$ denotes the lateral surface of SG in the undeformed beam, $\boldsymbol{p} = p_i \boldsymbol{T}_i$ is the applied body force per unit undeformed volume, and $\boldsymbol{Q} = Q_i \boldsymbol{T}_i$ represents the tractions applied on the surfaces of the undeformed beam. If the displacements on the end surfaces are prescribed, then the last two terms of Eq. (4.31) will vanish. $\delta\boldsymbol{R}$ is the Lagrangian variation of the displacement field in Eq. (4.5),

$$\delta\boldsymbol{R} = \overline{\delta q}_i \boldsymbol{T}_i + \varepsilon y_\alpha \delta\boldsymbol{T}_\alpha + \varepsilon \delta w_i \boldsymbol{T}_i + \varepsilon w_j \delta\boldsymbol{T}_j \tag{4.32}$$

As derived in [137], the virtual work can be expressed as

$$\overline{\delta\mathcal{W}} = \overline{\delta\mathcal{W}}_{1D} + \overline{\delta\mathcal{W}}^{*} \tag{4.33}$$

where $\overline{\delta\mathcal{W}}_{1D}$ is the virtual work not related with the fluctuating functions w_i. The term $\overline{\delta\mathcal{W}}^{*}$ in Eq. (4.33) is the virtual work related with the fluctuating functions. Ignoring the end effect brought by loads or displacement boundary, and assuming the loads applied are independent of the fluctuating functions, $\overline{\delta\mathcal{W}}^{*}$ can be rewritten as

$$\overline{\delta\mathcal{W}}^{*} = \delta \int_0^l \frac{1}{\omega} \left(\langle p_i w_i \rangle + \oint_{\partial\Omega} Q_i w_i \sqrt{c}\ \mathrm{d}s \right) \mathrm{d}x_1 \equiv \delta \int_0^l \frac{1}{\omega} W^{*} \mathrm{d}x_1 \tag{4.34}$$

Substituting the strain energy in Eq. (4.29) and the virtual work in Eq. (4.33), the variational statement Eq. (4.28) can be rewritten as

$$\int_0^l \frac{1}{\omega} \delta \left[\frac{1}{2} \left\langle \Gamma^{\mathrm{T}} D \Gamma \right\rangle - \varepsilon \left(\langle p_i w_i \rangle + \oint_{\partial\Omega} Q_i w_i \sqrt{c}\ \mathrm{d}s \right) \right] \mathrm{d}x_1 = 0 \tag{4.35}$$

Note in Eq. (4.35), a small parameter ε is added to the virtual work term according to the VAM analysis, implying this term is asymptotically smaller than the strain energy term.

Now we have presented the original 3D problem of the beam-like structure as Eq. (4.28) in terms of 1D kinematics and 3D fluctuating functions w_i. Observing Eq. (4.35), we can conclude that w_i is governed by Eq. (4.36) as the Lagrangian variation δ is posed over the SG domain only.

$$\delta\Pi = \delta \left[\frac{1}{2} \left\langle \Gamma^{\mathrm{T}} D \Gamma \right\rangle - \varepsilon \left(\langle p_i w_i \rangle + \oint_{\partial\Omega} Q_i w_i \sqrt{c}\ \mathrm{d}s \right) \right] = 0 \tag{4.36}$$

where $\Pi \equiv U - W^{*}$.

4.1.3 Dimensional Reduction

Zeroth-order approximation

First we seek a solution of the variational statement Eq. (4.36) to the zeroth-order, that is any term associated with ε or higher orders of ε in Eq. (4.36) is neglected. Therefore Eq. (4.36) is simplified to

$$\delta U_0 = \delta \frac{1}{2} \left\langle \Gamma_0^{\mathrm{T}} D \Gamma_0 \right\rangle = 0 \tag{4.37}$$

where U_0 is the zeroth-order strain energy of a SG,

$$U_0 = \frac{1}{2} \left\langle \Gamma_0^{\mathrm{T}} D \Gamma_0 \right\rangle \tag{4.38}$$

and Γ_0 is the zeroth-order approximation of the 3D strain Γ

$$\Gamma_0 = \Gamma_h \; w + \Gamma_\epsilon \; \bar{\epsilon} \tag{4.39}$$

It is noted in the zeroth-order approximation in Eq. (4.37), the influence of the applied loads to the solution is neglected because it is of higher order. Using FEM to solve the variational statement in Eq. (4.37), the fluctuating functions w_i can be discretized as

$$w(x_1; y_i) = S(y_i) \, V(x_1) \tag{4.40}$$

with $S(y_i)$ representing the element shape functions depending on the element types which one uses. $V(x_1)$ is the nodal values of the fluctuating functions to solve over the SG. Substituting Eq. (4.40) into Eq. (4.38), we obtain the following discretized version of the strain energy functional:

$$U_0 = \frac{1}{2} \left(V^{\mathrm{T}} E V + 2 V^{\mathrm{T}} D_{h\epsilon} \bar{\epsilon} + \bar{\epsilon}^{\mathrm{T}} D_{\epsilon\epsilon} \bar{\epsilon} \right) \tag{4.41}$$

where

$$E = \left\langle \left(\Gamma_h S\right)^{\mathrm{T}} D \left(\Gamma_h S\right) \right\rangle, \quad D_{h\epsilon} = \left\langle \left(\Gamma_h S\right)^{\mathrm{T}} D \Gamma_\epsilon \right\rangle, \quad D_{\epsilon\epsilon} = \left\langle \Gamma_\epsilon^{\mathrm{T}} D \Gamma_\epsilon \right\rangle \tag{4.42}$$

By minimizing U_0 in Eq. (4.41) subject to the constraints of Eq. (4.10), the linear system of Eq. (4.43) can be obtained, and the zeroth-order values of V can be solved.

$$E V = -D_{h\epsilon} \bar{\epsilon} \tag{4.43}$$

V can be symbolically written as Eq. (4.44) since it linearly depends on $\bar{\epsilon}$. As pointed out by Yu in [137], the zeroth-order solution V_0 is independent of the constraints. $\bar{V}_0$ is referred as the fluctuating functions coefficients.

$$V = \hat{V}_0 \bar{\epsilon} = V_0 \tag{4.44}$$

Substituting Eq. (4.44) back into Eq. (4.41), the strain energy stored in the SG as the zeroth-order approximation is

$$U_0 = \frac{1}{2}\bar{\epsilon}^{\mathrm{T}}\left(V_0^{\mathrm{T}} D_{h\epsilon} + D_{\epsilon\epsilon}\right)\bar{\epsilon} \equiv \frac{\omega}{2}\bar{\epsilon}^{\mathrm{T}}\bar{D}\bar{\epsilon} \tag{4.45}$$

where $\bar{D}$ is the effective beam stiffness matrix to be used in the macroscopic structural model. It is noteworthy that for the GEB model, $\bar{D}$ could be a fully populated 4×4 stiffness matrix. Now the local displacement field can be obtained as

$$u_i(x_1, y_1, y_2, y_3) = \bar{u}_i(x_1) + \varepsilon y_\alpha\left[C_{\alpha i}^{Tb}(x_1) - \delta_{\alpha i}\right] + \varepsilon C_{ji}^{Tb} w_j(x_1, y_1, y_2, y_3) \tag{4.46}$$

where u_i is the local displacement, $\bar{u}_i$ is the macroscopic displacement, δ_{ij} is the Kronecker delta symbol. C_{ij}^{Tb} represents components of the direction cosine matrix of finite rotations from triad $\boldsymbol{b}_i$ to triad $\boldsymbol{T}_i$. To obtain C_{ij}^{Tb}, first C_{ij}^{Bb} are calculated directly from the 1D analysis, then C_{ij}^{Tb} is obtained through Eq. (4.4). For 3D SGs, $\bar{u}_i$ should be interpreted as

$$\bar{u}_i = \bar{u}_i(x_0) + x_1\bar{u}_{i,1} \tag{4.47}$$

where x_0 is the center of the SG and $\bar{u}_{i,1}$ is the gradient of macroscopic displacement $\bar{u}_i$ along x_1 evaluated at x_0. The local strain field can be obtained as

$$\Gamma = \left(\Gamma_h S V_0 + \Gamma_\epsilon\right)\bar{\epsilon}. \tag{4.48}$$

The local stress field can be obtained directly using the Hooke's law as

$$\sigma = D\Gamma. \tag{4.49}$$

Second-order approximation

In cases when a GEB model is not sufficiently accurate, higher order approximation of the variational statement is needed. First we can perturb the unknown fluctuating function as

$$V = V_0 + \varepsilon V_1 \tag{4.50}$$

where V_1 is asymptotically smaller than V_0, i.e., $V_1 \sim o(V_0)$. Substitute Eq. (4.50), Eq. (4.22) and Eq. (4.40) into Eq. (4.30) and keep the terms to the order of ε^2, the strain energy of the SG can be written as

$$\begin{aligned}
2U_1 = {} & \bar{\epsilon}^{\mathrm{T}}(\hat{V}_0^{\mathrm{T}} D_{h\epsilon} + D_{\epsilon\epsilon})\bar{\epsilon} + 2(V_0^{\mathrm{T}} D_{hR} V_0 + V_0^{\mathrm{T}} D_{hl} V_0' + V_0^{\mathrm{T}} D_{R\epsilon}\bar{\epsilon} + V_0'^{\mathrm{T}} D_{l\epsilon}\bar{\epsilon}) \\
& + V_1^{\mathrm{T}} E V_1 + 2V_1^{\mathrm{T}}(D_{hR} V_0 + D_{hR}^{\mathrm{T}} V_0 + D_{R\epsilon}\bar{\epsilon}) + 2V_1^{\mathrm{T}} D_{hl} V_0' + 2V_0^{\mathrm{T}} D_{hl} V_1' \\
& + 2V_1'^{\mathrm{T}} D_{l\epsilon}\bar{\epsilon} + V_0^{\mathrm{T}} D_{RR} V_0 + 2V_0^{\mathrm{T}} D_{Rl} V_0' + V_0'^{\mathrm{T}} D_{ll} V_0'
\end{aligned} \tag{4.51}$$

where

$$\begin{aligned}
D_{hR} &= \left\langle [\Gamma_h\, S]^{\mathrm{T}}\ D\ [\Gamma_R\, S] \right\rangle & D_{RR} &= \left\langle [\Gamma_R\, S]^{\mathrm{T}}\ D\ [\Gamma_R\, S] \right\rangle \\
D_{R\epsilon} &= \left\langle [\Gamma_R\, S]^{\mathrm{T}}\ D\, \Gamma_\epsilon \right\rangle & D_{hl} &= \left\langle [\Gamma_h\, S]^{\mathrm{T}}\ D\ [\Gamma_{l\, S}] \right\rangle \\
D_{ll} &= \left\langle [\Gamma_l\, S]^{\mathrm{T}}\ D\ [\Gamma_l\, S] \right\rangle & D_{l\epsilon} &= \left\langle [\Gamma_l\, S]^{\mathrm{T}}\ D\, \Gamma_\epsilon \right\rangle \\
D_{Rl} &= \left\langle [\Gamma_R\, S]^{\mathrm{T}}\ D\ [\Gamma_l\, S] \right\rangle
\end{aligned} \tag{4.52}$$

and the portion of the work from applied loads due to fluctuating functions becomes W^* in (4.34) so that

$$W^* = (V_0 + V_1)^{\mathrm{T}} L \tag{4.53}$$

where $L \equiv \left\langle S^{\mathrm{T}} p \right\rangle + \oint S^{\mathrm{T}} Q \sqrt{c}\ \mathrm{d}s$ with p as a column matrix containing p_i and Q as a column matrix containing Q_i. The variational statement of the refined beam model now can be represented as

$$\Pi_1 = U_1 - W^* \tag{4.54}$$

From Yu and Hodges [137], the second-order leading terms without the constant terms of Eq. (4.54) are

$$2\Pi_1^* = V_1^{\mathrm{T}} E\, V_1 + 2V_1^{\mathrm{T}} D_R \bar{\epsilon} + 2V_1^{\mathrm{T}} D_S \bar{\epsilon}' - 2V_1^{\mathrm{T}} L \tag{4.55}$$

where

$$\begin{aligned}
D_R &= \left(D_{hR} + D_{hR}^{\mathrm{T}}\right) \hat{V}_0 + D_{R\epsilon} \\
D_S &= \left(D_{hl} - D_{hl}^{\mathrm{T}}\right) \hat{V}_0 - D_{l\epsilon}
\end{aligned} \tag{4.56}$$

Minimizing Eq. (4.55) with the constraints of Eq. (4.10), the Euler-Lagrange equation of this problem is

$$E\,V = \left[D_c\left(\Psi^{\mathrm{T}} D_c\right)^{-1}\Psi^{\mathrm{T}} - \Delta\right]\left(D_R\,\bar{\epsilon} + D_S\,\bar{\epsilon}' - L\right) \tag{4.57}$$

where D_c and ψ are terms related with the constraints in Eq. (4.10). Substituting Eq. (4.40) into Eq. (4.10), the constraints can be expressed in a discretized form that

$$V^T D_c = 0 \tag{4.58}$$

with $D_c^T = \langle \Gamma_c\,S\rangle$. Ψ is the nodal values of the matrix ψ when expressed in the discretized form as

$$\psi = S\Psi \tag{4.59}$$

The periodic constraints in Eq. (4.12) can be applied by equating the nodal values of the fluctuating functions at A_1^- and A_1^+ through eliminating the corresponding nodal DOFs. Then the first-order approximation of the fluctuating function V_1 can be solved in a form of

$$V_1 = V_{1R}\bar{\epsilon} + V_{1S}\bar{\epsilon}' - V_L \tag{4.60}$$

Using Eq. (4.60), the second-order asymptotically correct energy can now be obtained from Eq. (4.54) as

$$2\Pi_1 = \bar{\epsilon}^{\mathrm{T}}\mathcal{A}\bar{\epsilon} + 2\bar{\epsilon}^{\mathrm{T}}\mathcal{B}\bar{\epsilon}' + \bar{\epsilon}'^{\mathrm{T}}\mathcal{C}\bar{\epsilon}' + 2\bar{\epsilon}^{\mathrm{T}}\mathcal{D}\bar{\epsilon}'' - 2\bar{\epsilon}^{\mathrm{T}}\mathcal{F}_\epsilon - 2\bar{\epsilon}'^{\mathrm{T}}\mathcal{F}_{\epsilon'} \tag{4.61}$$

where

$$\begin{aligned}
\mathcal{A} &= \hat{V}_0^{\mathrm{T}} D_{h\epsilon} + D_{\epsilon\epsilon} + \hat{V}_0^{\mathrm{T}}\left(D_{hR} + D_{hR}^{\mathrm{T}} + D_{RR}\right)\hat{V}_0 + 2\hat{V}_0^{\mathrm{T}} D_{R\epsilon} + V_{1R}^{\mathrm{T}} D_R \\
\mathcal{B} &= \hat{V}_0^{\mathrm{T}}\left(D_{hl} + D_{Rl}\right)\hat{V}_0 + D_{l\epsilon}^{\mathrm{T}}\hat{V}_0 + \left(\hat{V}_0^{\mathrm{T}} D_{hl} + D_{l\epsilon}^{\mathrm{T}}\right) V_{1R} + \frac{1}{2}(D_R^{\mathrm{T}} V_{1S} + V_{1R}^{\mathrm{T}}\bar{D}_S) \\
\mathcal{C} &= V_{1S}^{\mathrm{T}}\bar{D}_S + \hat{V}_0^{\mathrm{T}} D_{ll}\hat{V}_0 \\
\mathcal{D} &= (\hat{V}_0^{\mathrm{T}} D_{hl} + D_{l\epsilon}^{\mathrm{T}})V_{1S} \\
\mathcal{F}_\epsilon &= \hat{V}_0^{\mathrm{T}} L + (\hat{V}_0^{\mathrm{T}} D_{hl} + D_{l\epsilon}^{\mathrm{T}})V_L' + \frac{1}{2}(D_R^{\mathrm{T}} V_L + V_{1R}^{\mathrm{T}} L) \\
\mathcal{F}_{\epsilon'} &= \frac{1}{2}(\bar{D}_S^{\mathrm{T}} V_L + V_{1S}^{\mathrm{T}} L)
\end{aligned} \tag{4.62}$$

and $\bar{D}_S = \left(D_{hl} + D_{hl}^{\mathrm{T}}\right)\hat{V}_0 + D_{l\epsilon}$.

4.1.4 Transformation to Generalized Timoshenko Beam Model

The energy formulation of Eq. (4.61) is difficult to use in practice due to the appearance of the derivatives of $\bar{\epsilon}$. Using this form, additional boundary conditions without clear physical interpretations are required. Therefore, it is ideal to transform the form of Eq. (4.61) to a commonly used GTB model.

Two times the total potential potential energy of the SG, including the load related terms, of the generalized Timoshenko model can be written as

$$2\Pi_1 = \epsilon^{\mathrm{T}} X \epsilon + 2\epsilon^{\mathrm{T}} Y \gamma_s + \gamma_s^{\mathrm{T}} G \gamma_s - 2\epsilon^{\mathrm{T}} F_\epsilon - 2\gamma_s^{\mathrm{T}} F_\gamma \tag{4.63}$$

Considering the kinematic relations between the Euler-Bernoulli beam strain measures $\bar{\epsilon}$ and the Timoshenko beam strain measures ϵ and γ_s in Eq. (4.19), and the static equilibrium equations for $\bar{\epsilon}$, $\bar{\epsilon}'$ and $\bar{\epsilon}''$ in terms of ϵ and γ_s, the stiffness matrix of the GTB can be generalized. G, Y and X can be calculated in order using the following equations

$$G = \left(H^{\mathrm{T}} \mathcal{A}^{-1} (\mathcal{C} - \mathcal{B}^{\mathrm{T}} \mathcal{A}^{-1} \mathcal{B}) \mathcal{A}^{-1} H\right)^{-1} \tag{4.64}$$

$$Y = \mathcal{B}^{\mathrm{T}} \mathcal{A}^{-1} H G \tag{4.65}$$

$$X = \mathcal{A} + Y G^{-1} Y^{\mathrm{T}} \tag{4.66}$$

The derivation of this step is very lengthy and the details could be found in the appendix of [137]. It is noted that Eqs. (4.64), (4.65) and (4.66) are valid for prismatic beam only, the formulas for corrections due to initial curvature can also be found in [137]. It is noted that the loads $\mathcal{F}_\epsilon$ and $\mathcal{F}_{\epsilon'}$ from Eq. (4.61) are from $\boldsymbol{T}_i$ basis, which also should be transformed to F_ϵ and F_γ in the $\boldsymbol{B}_i$ basis in Eq. (4.63).

$$F_\epsilon = \alpha^{\mathrm{T}} \mathcal{F}_\epsilon + \alpha'^{\mathrm{T}} \mathcal{F}_{\epsilon'} \qquad F_\gamma = \beta^{\mathrm{T}} \mathcal{F}_\epsilon + \beta'^{\mathrm{T}} \mathcal{F}_{\epsilon'} \tag{4.67}$$

where α, α', β, and β' have been shown in detail in [137]. Based on the results given, we can write the potential energy of the GTB model in the following form explicitly

$$2\Pi = \begin{Bmatrix} \gamma_{11} \\ 2\gamma_{12} \\ 2\gamma_{13} \\ \kappa_1 \\ \kappa_2 \\ \kappa_3 \end{Bmatrix}^{\mathrm{T}} \begin{bmatrix} S_{11} & S_{12} & S_{13} & S_{14} & S_{15} & S_{16} \\ S_{12} & S_{22} & S_{23} & S_{24} & S_{25} & S_{26} \\ S_{13} & S_{23} & S_{33} & S_{34} & S_{35} & S_{36} \\ S_{14} & S_{24} & S_{34} & S_{44} & S_{45} & S_{46} \\ S_{15} & S_{25} & S_{35} & S_{45} & S_{55} & S_{56} \\ S_{16} & S_{26} & S_{36} & S_{46} & S_{56} & S_{66} \end{bmatrix} \begin{Bmatrix} \gamma_{11} \\ 2\gamma_{12} \\ 2\gamma_{13} \\ \kappa_1 \\ \kappa_2 \\ \kappa_3 \end{Bmatrix} - 2 \begin{Bmatrix} \gamma_{11} \\ 2\gamma_{12} \\ 2\gamma_{13} \\ \kappa_1 \\ \kappa_2 \\ \kappa_3 \end{Bmatrix}^{\mathrm{T}} \begin{Bmatrix} \mathcal{F}_1 \\ \mathcal{F}_2 \\ \mathcal{F}_3 \\ \mathcal{M}_1 \\ \mathcal{M}_2 \\ \mathcal{M}_3 \end{Bmatrix} \tag{4.68}$$

The 1D constitutive model in Eq. (4.68) can be used as input for a 1D beam analysis to calculate the global beam behavior including 1D displacements/rotations, 1D Timoshenko beam strain measures ϵ and γ_s and stress resultants along the reference line.

If the local fields of the original 3D structures are concerned, such as the displacement, strain and stress, values of the 1D quantities may subsequently be taken to recover the 3D quantities over the SG using the recovery relations. First, the 3D displacement u_i can be computed using Eq. (4.46). The 3D fluctuating functions of the SG can be calculated by

$$w(x_1, x_2, x_3) = S(\hat{V}_0 + V_{1R})\bar{\epsilon} + SV_{1S}\bar{\epsilon}' - SV_L \tag{4.69}$$

And the 3D strain field in terms of the 1D generalized Timoshenko strain measures are

$$\begin{aligned} \Gamma = & \left[(\Gamma_h + \Gamma_R)S(\hat{V}_0 + V_{1R}) + \Gamma_\epsilon\right](\epsilon + H\gamma_s' + P\gamma_s) \\ & + \left[(\Gamma_h + \Gamma_R)SV_{1S} + \Gamma_l S(\hat{V}_0 + V_{1R})\right](\epsilon' + H\gamma_s'' + P\gamma_s') \\ & + \Gamma_l SV_{1S}(\epsilon'' + H\gamma_s''' + P\gamma_s'') \\ & - (\Gamma_h + \Gamma_R)SV_L - \Gamma_l SV_L' \end{aligned} \tag{4.70}$$

In Eq. (4.70), the generalized Timoshenko strain measures can be derived from the 1D constitutive law if the stress resultants are given instead. Let S_R be the stiffness matrix in the form so that the constitutive law is arranged as

$$\epsilon_R = S_R^{-1} F_R + \mathcal{E} \tag{4.71}$$

where $\epsilon_R \equiv \lfloor\ \epsilon_{11}\ \ 2\gamma_{12}\ \ 2\gamma_{13}\ \ \kappa_1\ \ \kappa_2\ \ \kappa_3 \rfloor^{\mathrm{T}}$ and $F_R \equiv \lfloor\ F_1\ \ F_2\ \ F_3\ \ M_1\ \ M_2\ \ M_3 \rfloor^{\mathrm{T}}$. The term $\mathcal{E}$ represents the strains due to applied loads in the SG analysis and $\mathcal{E} \equiv S_R^{-1} \lfloor \mathcal{F}_1\ \ \mathcal{F}_2\ \ \mathcal{F}_3\ \ \mathcal{M}_1\ \ \mathcal{M}_2\ \ \mathcal{M}_3 \rfloor^{\mathrm{T}}$. Based on the 1D nonlinear equilibrium equations given in [137, 170], the first derivative of F_R is obtained by Yu et. al [137]

$$F_R' = -R_R F_R - \phi = -\begin{bmatrix} \widetilde{K} & O_3 \\ \widetilde{e}_1 + \widetilde{\gamma} & \widetilde{K} \end{bmatrix} F_R - \phi \tag{4.72}$$

where $\phi = \lfloor f_1\ f_2\ f_3\ m_1\ m_2\ m_3 \rfloor^{\mathrm{T}}$ contains the distributed 1D applied and inertial loads in the $\boldsymbol{B}_i$ basis. O_3 is a 3×3 matrix of zeros. The curvature vector of deformed GTB is denoted as $\boldsymbol{K} = \lfloor k_1 + \kappa_1\ k_2 + \kappa_2\ k_3 + \kappa_3 \rfloor^{\mathrm{T}}$, in which κ_1 is the twist curvature and κ_2, κ_3 are the bending curvatures. $\widetilde{K}$ is the antisymmetric tensor form of $\boldsymbol{K}$ as shown in Eq. (4.73). $\boldsymbol{e}_1 = \lfloor 1\ 0\ 0 \rfloor^{\mathrm{T}}$ and $\boldsymbol{\gamma} = \lfloor \gamma_{11}\ 2\gamma_{12}\ 2\gamma_{13} \rfloor^{\mathrm{T}}$. In the same fashion, $\widetilde{e}_1$ and $\widetilde{\gamma}$ are expressed in the antisymmetric tensor form.

$$\widetilde{K} = -\begin{bmatrix} 0 & -(k_3 + \kappa_3) & k_2 + \kappa_2 \\ k_3 + \kappa_3 & 0 & -(k_1 + \kappa_1) \\ -(k_2 + \kappa_2) & k_1 + \kappa_1 & 0 \end{bmatrix} \tag{4.73}$$

By differentiating Eq. (4.72) and applying recursive relationships, the higher order derivatives can be derived

$$\begin{aligned} F_R'' &= (R_R^2 - R_R')F_R + R_R\phi - \phi' \\ F_R''' &= (-R_R^3 + R_R R_R' + 2R_R' R_R - R_R'')F_R + (-R_R^2 + 2R_R')\phi + R_R\phi' - \phi'' \end{aligned} \tag{4.74}$$

Differentiating Eq. (4.71) results in

$$\begin{aligned} \epsilon_R' &= S_R^{-1} F_R' + \mathcal{E}' \\ \epsilon_R'' &= S_R^{-1} F_R'' + \mathcal{E}'' \\ \epsilon_R''' &= S_R^{-1} F_R''' + \mathcal{E}''' \end{aligned} \tag{4.75}$$

Now we can substitute Eqs. (4.72) and (4.74) into Eq. (4.75) to obtain derivatives of the generalized Timoshenko strain measures, then calculate the 3D strain field using Eq. (4.70). It should be emphasized that in the MSG GTB theory, the recovered 3D strain fields are obtained from both the loads $\mathcal{E}$ and stress resultants F_R in the 1D sense. At last, the 3D stress field can be calculated from the 3D strain field using the Hooke's law as shown in Eq. (4.49).

4.2 MSG Implementation for Free-edge Stress Analysis

Although MSG can be used to analyze the free-edge problem of initially twisted and curved laminates, here we only focus on straight laminates for illustrative purpose. Consider a general laminate of length l, width $2b$, thickness h and made of n layers of lamina of thickness h_0. The laminate is loaded at $x_1 = 0$ and $x_1 = l$. An example is shown in Fig. 4.3. The laminate is clamped at $x_1 = 0$ and subjected to extension force F_1°, shear forces F_2°, F_3°, bending moments M_2°, M_3° and torque M_1° at $x_1 = l$, of which the positive directions of the forces and moments are shown in Fig. 4.3. Without loss of generality, we choose the origin of orthonormal coordinate system $o - x_1y_2y_3$ in the $y_2 - y_3$ plane to be the geometry center of the cross section of the laminate. On both the free-edges and the top and bottom surfaces of the laminate traction-free conditions exist. The laminate is sufficiently long along the x_1 direction so that in the region away from the two ends the boundary effect can be neglected by virtue of the Saint-Venant principle. Nevertheless, the stress and strain fields are not necessarily independent of x_1 due to the loads applied. According to MSG, the cross section can be considered as the structure genome (SG) because one can use the cross section as the fundamental building block to build the laminate along the x_1 axis and the corresponding macroscopic structural model is a 1D beam model along x_1.

Without loss of generality, the applicability to solve free-edge problem implementing MSG beam cross sectional analysis is explained using the GEB model. According

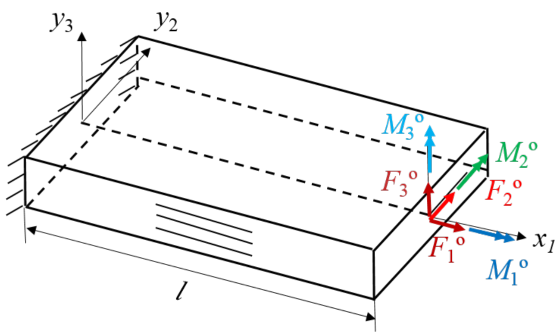

(a)

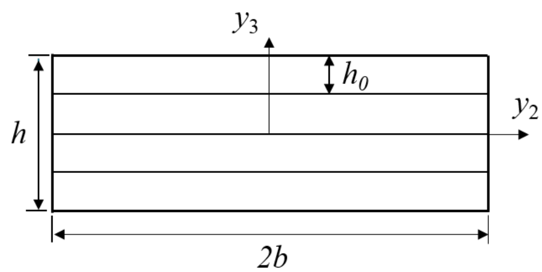

(b)

Fig. 4.3. The laminate geometry and coordinate system.

to MSG, we need to first express the displacements of the original 3D elasticity theory in terms of the displacements of the 1D beam model as

$$\begin{aligned} u_1(x_1, y_2, y_3) &= \bar{u}_1(x_1) - \varepsilon y_3 \bar{u}_{3,1} - \varepsilon y_2 \bar{u}_{2,1} + \varepsilon w_1(x_1, y_2, y_3) \\ u_2(x_1, y_2, y_3) &= \bar{u}_2(x_1) - \varepsilon y_3 \bar{\phi}(x_1) + \varepsilon w_2(x_1, y_2, y_3) \\ u_3(x_1, y_2, y_3) &= \bar{u}_3(x_1) + \varepsilon y_2 \bar{\phi}(x_1) + \varepsilon w_3(x_1, y_2, y_3) \end{aligned} \tag{4.76}$$

where $u_i(x_1, y_2, y_3)$ denote the displacements of the 3D elasticity theory, $\bar{u}_i(x_1)$ represent the beam displacements which are area average of the 3D displacements over the cross section, and $\bar{\phi}(x_1)$ describes the average twist of the cross section such that

$$\bar{\phi} = \langle u_{3|2} - u_{2|3} \rangle \tag{4.77}$$

where $\langle\cdot\rangle$ represents area integration over the cross section. $w_i(x_1, y_2, y_3)$ are the fluctuating functions to express the displacements which cannot be represented by the 1D kinematic variables ($\bar{u}_1, \bar{u}_2, \bar{u}_3$, and $\bar{\phi}$).

From Eq. (4.76), we can obtain the strains as

$$
\begin{aligned}
\Gamma_{11} &= \bar{\epsilon}_{11} + y_3\bar{\kappa}_2 - y_2\bar{\kappa}_3 + w_{1,1} \\
\Gamma_{22} &= w_{2|2} \\
\Gamma_{33} &= w_{3|3} \\
2\Gamma_{23} &= w_{2|3} + w_{3|2} \\
2\Gamma_{13} &= y_2\bar{\kappa}_1 + w_{1|3} + w_{3,1} \\
2\Gamma_{12} &= -y_3\bar{\kappa}_1 + w_{1|2} + w_{2,1}
\end{aligned}
$$

with $\bar{\epsilon}_{11} = \bar{u}_{1,1}, \bar{\kappa}_1 = \bar{\phi}_{,1}, \bar{\kappa}_2 = -\bar{u}_{3,11}, \bar{\kappa}_3 = \bar{u}_{2,11}$.

The original 3D problem is split into a 2D cross sectional analysis and a 1D analysis of the reference line, which can be treated as a beam analysis and can be solved analytically or numerically. To solve the generalized free-edge problem using MSG, the following three steps are required:

- Perform a homogenization analysis over the 2D cross section problem, from which the effective beam properties describing the behavior of the reference line will be obtained, along with the dehomogenization relations expressing the fluctuating functions w_i in terms of the beam strains ($\bar{\epsilon}$,$\bar{\kappa}_1$,$\bar{\kappa}_2$,$\bar{\kappa}_3$). For GTB model, beam strains also include transverse shear strains.

- Solve the 1D beam problem subjected to the generalized loads applied at the two ends to obtain beam strains.

- Perform a dehomogenization analysis to obtain local fields such as displacements, stresses and strains at the cross section of interest with the beam strains or cross section loads F_R (Eq. (4.71)) obtained in the previous step as the inputs.

From the numerical examples, it will be obvious to observe the power of this method. However, it is still worthwhile to discuss the limitation of this method in analyzing free-edge problem. Based on the plate model of MSG [24], the 3D strains can be expressed as:

$$
\begin{aligned}
u_1(x_1,x_2,y_3) &= \bar{u}_1(x_1,x_2) - \varepsilon y_3 \bar{u}_{3,1} + \varepsilon w_1(x_1,x_2,y_3) \\
u_2(x_1,x_2,y_3) &= \bar{u}_2(x_1,x_2) - \varepsilon y_3 \bar{u}_{3,2} + \varepsilon w_2(x_1,x_2,y_3) \\
u_3(x_1,x_2,y_3) &= \bar{u}_3(x_1,x_2) + \varepsilon w_3(x_1,x_2,y_3)
\end{aligned}
\tag{4.78}
$$

Here $u_i(x_1, x_2, y_3)$ are 3D displacements of the original laminate plate, while $\bar{u}_i(x_1, x_2)$ are plate displacements which are functions of x_1, x_2 only. We also introduce 3D unknown fluctuating functions $w_i(x_1, x_2, y_3)$ to describe the information of 3D displacements which cannot be described by the simpler Kirchhoff-Love plate kinematics.

$$
\begin{aligned}
\Gamma_{11} &= \epsilon_{11} + y_3\kappa_{11} + w_{1,1} \\
2\Gamma_{12} &= 2\epsilon_{12} + 2y_3\kappa_{12} + w_{1,2} + w_{2,1} \\
\Gamma_{22} &= \epsilon_{22} + y_3\kappa_{22} + w_{2,2} \\
2\Gamma_{13} &= w_{1|3} + w_{3,1} \\
2\Gamma_{23} &= w_{2|3} + w_{3,2} \\
\Gamma_{33} &= w_{3|3}
\end{aligned}
$$

with the linear plate strains defined as

$$
\epsilon_{\alpha\beta}(x_1,x_2) = \frac{1}{2}(\bar{u}_{\alpha,\beta} + \bar{u}_{\beta,\alpha}); \quad \kappa_{\alpha\beta}(x_1,x_2) = -\bar{u}_{3,\alpha\beta} \tag{4.79}
$$

Here α, β denotes subscript 1 or 2.

It can be seen that $\bar{\kappa}_2$ of beam has the same expression as κ_{11} of plate. There is no straight forward corresponding relations for the $\bar{\kappa}_1$, $\bar{\kappa}_3$ of beams and κ_{22} and twist curvature $\kappa_{12} = -\bar{u}_{3,12}$ of plates. In another word, this method cannot be applied to the case when the average deformation characteristics of the laminated cross section cannot be fully captured by the strains and curvatures of the beam reference line.

4.3 Numerical Examples

4.3.1 Laminate of Rectangular Cross Section under F_3° and M_2°

Firstly, a laminate with layup $[60/30/-45/45]$ subjected to shear loads is considered. The layup is denoted from the bottom suface to the top surface of the laminate. The laminar material properties are E_1=137.895 GPa, E_2=E_3=14.479 GPa, G_{12} =G_{13}=G_{23}=5.861 GPa, ν_{12} =ν_{13}=ν_{23}=0.21. The laminate has a total thickness of $h = 4$ mm, width $2b = 16$ mm, and length $l = 96$ mm. Each layer has a thickness of 1 mm. This laminate can be viewed as a short beam-like structure with the aspect ratio $l/2b = 6$. According to the modeling framework of MSG, first a homogenization analysis of the cross section is conducted and the stiffness matrix of the homogeneous beam can be obtained. The effective stiffness components in D are arranged in a form that shown in Eq. (4.68). It can be seen that the effective beam shear stiffness are at a similar order of the other diagonal terms. In addition, the couplings between shear and extension, bending are not negligible.

$$D = \begin{bmatrix} 1.80\times10^6 & 3.28\times10^5 & 0.0 & 1.70\times10^5 & -2.20\times10^5 & 0.0 \\ 3.28\times10^5 & 1.39\times10^6 & 0.0 & -6.77\times10^5 & -1.28\times10^5 & 0.0 \\ 0.0 & 0.0 & 1.49\times10^5 & 0.0 & 0.0 & -1.73\times10^4 \\ 1.70\times10^5 & -6.77\times10^5 & 0.0 & 4.26\times10^6 & -6.43\times10^5 & 0.0 \\ -2.20\times10^5 & -1.28\times10^5 & 0.0 & -6.43\times10^5 & 1.76\times10^6 & 0.0 \\ 0.0 & 0.0 & -1.72\times10^4 & 0.0 & 0.0 & 3.38\times10^7 \end{bmatrix} \tag{4.80}$$

The laminate is clamped at $x_1 = 0$ and subjected to $F_3^\circ = 100$ N and $M_2^\circ = 4.8$ N $\cdot$ m at the other end $x_1 = l$. The stress distributions at the center cross section $x_1 = 48$ mm in the mid-span are considered, where a pure shear force $F_3 = 100$ N exists because the internal moment from the applied F_3° and M_2° canceled each other at $x_1 = 48$mm.

For comparison and verification, a 3D FEA model with the identical cross section mesh has been created in ABAQUS. The loads are applied at the geometry center of the cross section. All the lateral faces are traction free. From Table 4.1, it can be seen the MSG analysis can be finished within 12 seconds by a single CPU while 3D FEA consumes significant computation resource and time. However, the stress predicted by MSG agrees very well with that from the direct 3D FEA.

Table 4.1.
Computation cost comparison of MSG and 3D FEA models

Mesh	MSG	3D FEA
Node number	6,077	3,472,013
Element number	1,960	834,960
Element type	S8R	C3D20R
Computation time	12 seconds	306 minutes
CPUs	1	12

The mesh of the beam cross section for MSG analysis is shown in Fig. 4.4. It is noted that the element size gradually reduces from the center to the free-edges of the laminate along the y_2 direction. This is because stress variation is supposed to be relatively small around the center of the cross section, while it is expected to be significant as approaching the boundary due to free-edge effect. Furthermore, within each composite layer, the element size also gradually reduces from the center to the layer interfaces along the y_3 direction, since relative large stress variation crossing the interface is expected due to abrupt change of material orientation.

The distributions of interlaminar stress $(\sigma_{13}, \sigma_{23}, \sigma_{33})$ along the interfaces and free-edges extracted at the paths shown in Figs. 4.4 are compared. The results of the first loading case are compared in Fig. 4.5, 4.6, 4.7 and 4.8. The highly localized nature of interlaminar stresses near the vicinity of free-edge could be seen clearly, where the magnitude of interlaminar stresses change rapidly by only moving slightly away from

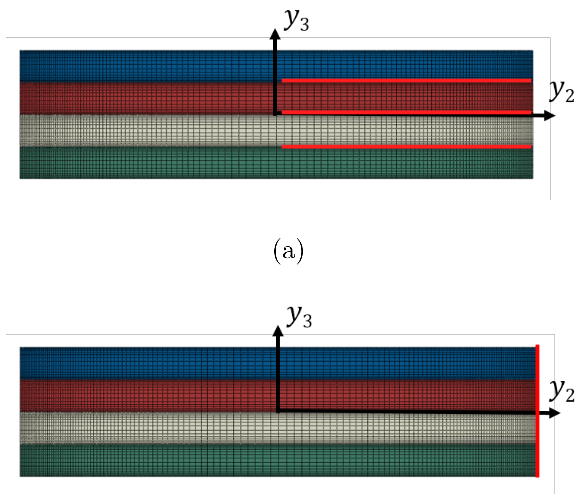

Fig. 4.4. Paths where the interlaminar stresses are extracted.

the free-edge. It is noteworthy that all the interlaminar stress components from MSG analysis agree very well with those of 3D FEA.

As shown in Fig. 4.5(a), among the three layer interfaces σ_{13} obtains its largest value at interface -45/45, while its smallest value at interface 60/30. As expected, σ_{13} almost stays constant at locations $y_2 < 0.5b$ with a magnitude close to the nominal value of $\frac{F_3}{h \cdot 2b} = 1.56$ MPa. However, as approaching the free-edges it quickly increases to a magnitude of multiple times. It is noted that around the free-edges σ_{13} grows much faster at interface -45/45 than at 30/-45 and 60/30. In addition, slight drop in σ_{13} is observed in the immediate vicinity of the free-edge at interface 60/30. With respect to σ_{23}, different layer interfaces show up different variation along the y_2 direction, as revealed in Fig. 4.5(b). At interfaces 30/-45 stays around zero along the entire interface, while at interface 60/30 and -45/45 σ_{23} is observed to keep constant at locations $y_2 < 0.5b$ but change quickly near the free-edge. As expected, at the free-edge σ_{23} is zero at all the three interfaces. σ_{13} and σ_{23} at the interfaces shown in Fig. 4.5(a) and (b) are symmetrical with the vertical axis. Fig. 4.6 shows the variation of σ_{33} along the layer interfaces. For the vast majority of the interface it

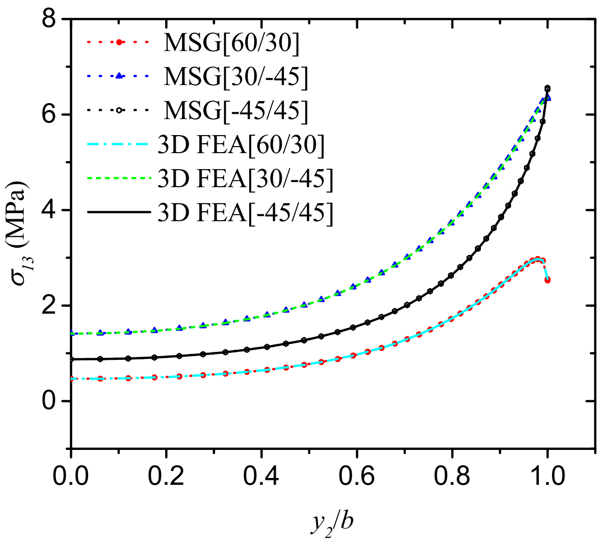

(a)

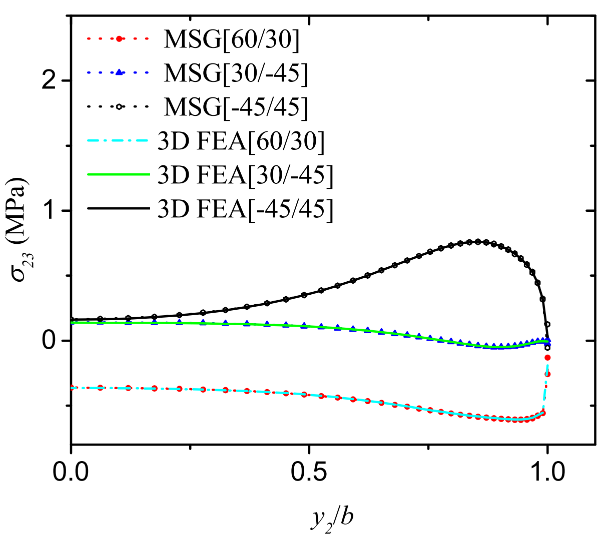

(b)

Fig. 4.5. Interlaminar shear stress distributions along the width of the laminate under $F_3 = 100$ N.

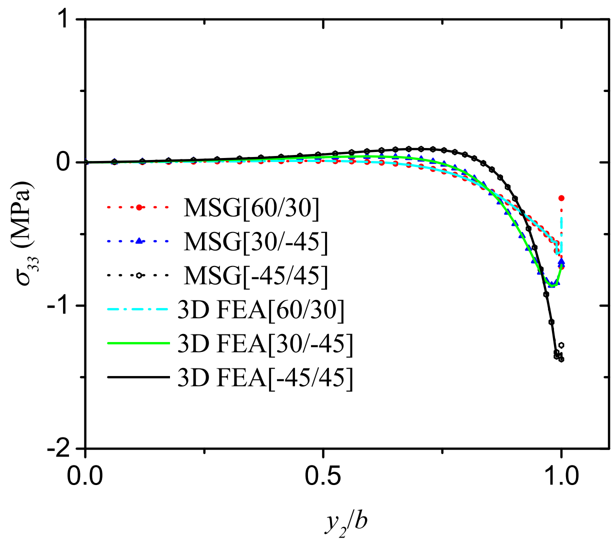

Fig. 4.6. Interlaminar normal stress distribution along the width of the laminate under $F_3 = 100$ N.

stays zero while near the free-edges it quickly increases in magnitude and turns to be compressive in sign. Noticing that at interfaces 60/30 and -45/45 σ_{33} turns around suddenly in the immediate vicinity of the free-edge to increase instead of decreasing. It is clear as revealed in Fig. 4.6 that, for composite beam, the zero transverse normal stress assumption in classical beam theories only stands at locations away from the free-edge.

For σ_{13} along the free-edge, an approximate parabolic shape is observed with zeros at the two ends as shown in Fig. 4.7(a), which is similar to the case of a homogeneous beam cross section. Interlaminar normal stress σ_{33} along free-edge is plotted in Fig. 4.8. Near the free-edge $y_3 = b$, the laminate is mostly under compressive σ_{33} except in a small portion of the bottom layer tensile σ_{33} is observed instead. Within each layer σ_{33} varies significantly from interface to interface, however the maximum σ_{33} does not emerge exactly at the layer interface.

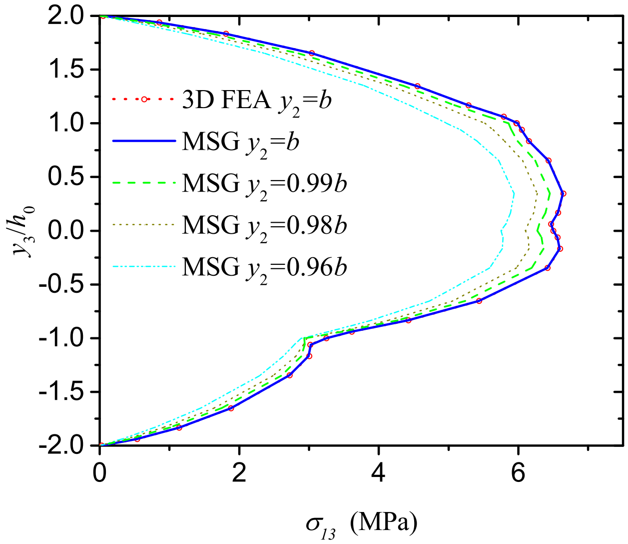

Fig. 4.7. Interlaminar shear stress distributions through the thickness along the free-edge of the laminate under $F_3 = 100$ N.

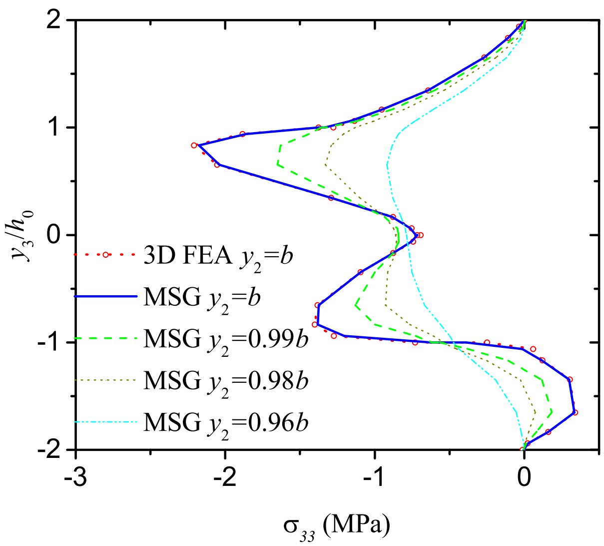

Fig. 4.8. Interlaminar normal stress distributions through the thickness along the free-edge of the laminate under $F_3 = 100$ N.

4.3.2 Laminate of Rectangular Cross Section under F_3°

Using the same laminate, the interlaminar stress are considered under another loading case, that is the laminate is clamped at $x_1 = 0$ and subjected to $F_3^\circ = 100$ N at the other end $x_1 = l$. Under this loading case, at the center cross section $x_1 = 48$ mm both shear force and bending moment exist internally, with $F_3 = 100$ m, and $M_2 = -4.8$ N·m.

Fig. 4.9 shows that σ_{13} are around zero along most part of the interface except near the free-edge. Around the free-edge it quickly increases in magnitude at interfaces 60/30 at $y_3 = -h_0$ and -45/45 at $y_3 = h_0$, where it turns into compressive in sign at $y_3 = -h_0$ and into tensile in sign at $y_3 = h_0$. σ_{13} stays almost identically zero along the entire interface -45/45. With respect to σ_{23}, Fig. 4.10 shows that its magnitude at interface 60/30 is multiple times of that at the other two interfaces. At interface 60/30 it gradually increases in magnitude from zero and then suddenly drops around the free-edge. Its variation at interfaces 30/-45 and -45/45 is more complex as it first increases then decreases and again increases near the free-edge. Fig. 4.11 reveals that σ_{33} is nonzero only around the free-edge where it is positive at interface -45/45 while negative at the other two interfaces. Under the bending moment $M_2 = 4.8\text{N} \cdot \text{m}$ the top portion of the cross section would subject to an axial tensile deformation, hence it would tend to shrink in the thickness direction. However, the ability to shrink of the top portion is constrained by the bottom portion, which in turn leads to a tensile interlaminar normal stress σ_{33} at interface -45/45. Similar explanation applies to the compressive interlaminar normal stress at interface 60/30.

Fig. 4.12 shows the shear stress σ_{13} at the free-edge. It is observed that σ_{13} is positive within all layers except the bottom one where it is negative. As shown in Fig. 4.13 interlaminar normal stress is observed to be much smaller within the top and bottom layers than the middle two layers. The only tensile σ_{33} occurs at the interface -45/45.

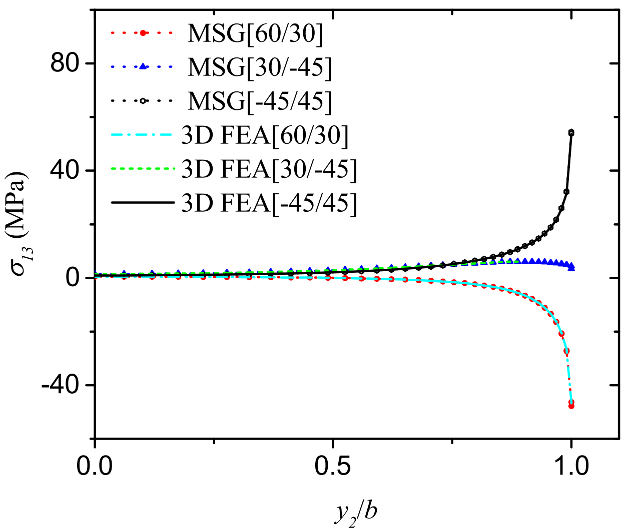

Fig. 4.9. Interlaminar shear stress σ_{13} distribution along the width of the laminate under $F_3 = 100$ N and $M_2 = -4.8$ N $\cdot$ m.

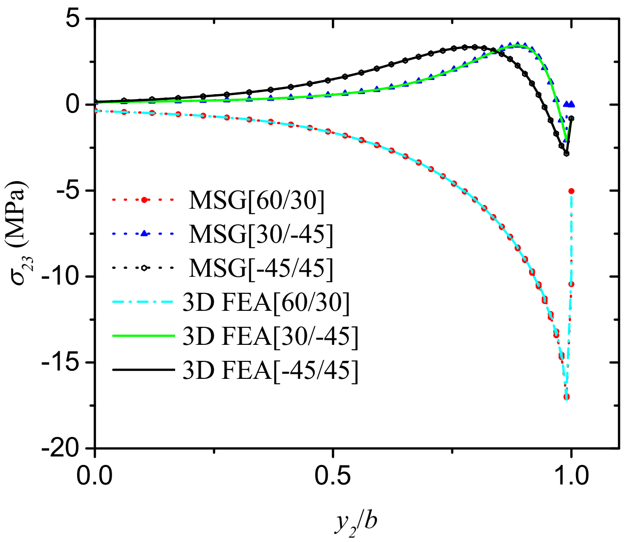

Fig. 4.10. Interlaminar shear stress σ_{23} distribution along the width of the laminate under $F_3 = 100$ N and $M_2 = -4.8$ N $\cdot$ m.

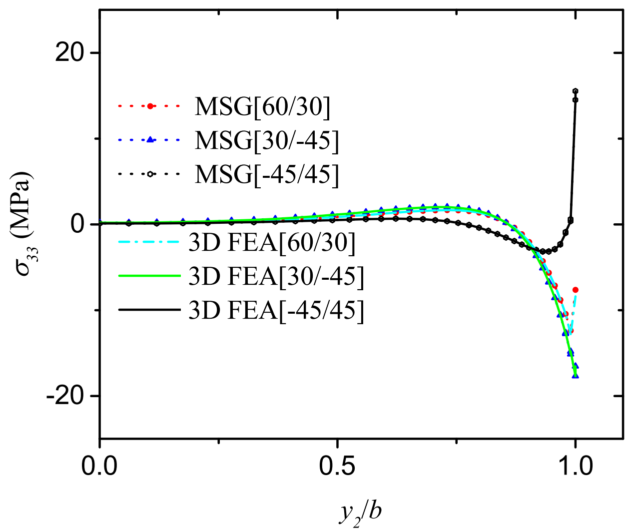

Fig. 4.11. Interlaminar normal stress distributions along the width of the laminate under $F_3 = 100$ N and $M_2 = -4.8$ N $\cdot$ m.

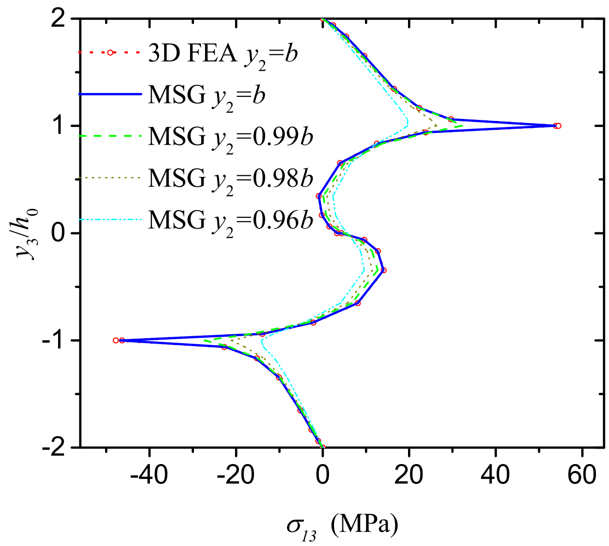

Fig. 4.12. Interlaminar shear stress distributions through the thickness along the free-edge of the laminate under $F_3 = 100$ N and $M_2 = -4.8$ N $\cdot$ m.

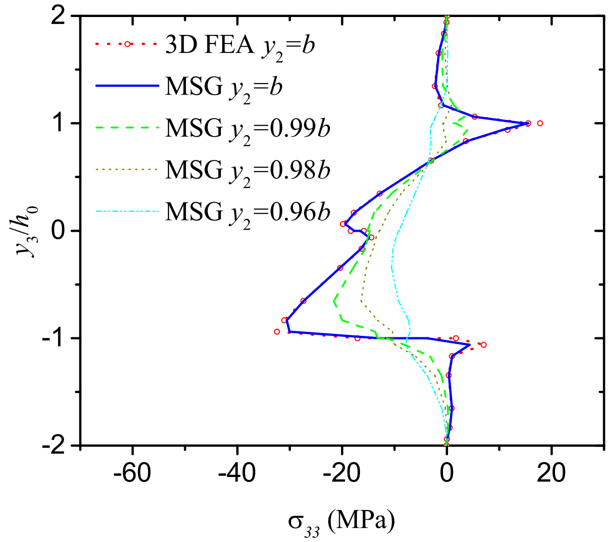

Fig. 4.13. Interlaminar normal stress distributions through the thickness along the free-edge of the laminate under $F_3 = 100$ N and $M_2 = -4.8$ N $\cdot$ m.

From Fig. 4.5, 4.6, 4.9, 4.10 and 4.11, it can be seen that the maximum magnitude of the interlaminar stress from the second loading case is considerably larger than that from the first loading case, implying that the internal bending moment contributes the major part to the interlaminar stress compared with the internal shear force.

4.3.3 Laminate of Curved Cross Section under F_3°

MSG can be implemented for free-edge analysis of arbitrary beam cross sections. In this example, a laminate beam with curved cross section is studied by the GTB model. The GEB model is also used to see the improvement brought by the GTB model. The geometry and layup information of this curved cross section beam is shown in Fig. 4.14. The beam is made of 4 layers of laminae with a stacking sequence of [-45/45/90/0]. Each layer of lamina has the same thickness of 1 mm, and the lamina material properties are E_1=132 GPa, E_2=E_3=10.8 GPa, G_{12} =G_{13}=5.650 GPa, G_{23}= 3.38 GPa, ν_{12} =ν_{13}=0.24, ν_{23}=0.59. The laminae arcs have a 60 degree central angle.

The arc length of the outer surface of 0 deg lamina is 18.1 mm, corresponding to a chord length of 17.3 mm in y_2 direction. The total length of the curved beam is 120 mm, which established a short beam with a length/width ratio of about 7. The coordinate origin of the curved cross section is chosen at the center of circle. The curved beam is clamped at $x_1 = 0$ mm, and imposed a shear force of $F_3^\circ = -100$ N at the center of circle of the other end $x_1 = 120$ mm.

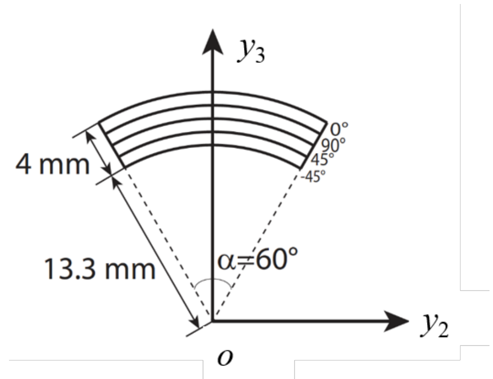

Fig. 4.14. Cross section geometry of curved beam laminate.

From the homogenization, the effective beam properties for the GTB model can be calculated as shown in Eq. (4.81).

$$D = \begin{bmatrix} 3.18\times10^6 & 9.42\times10^4 & 0.0 & -1.49\times10^6 & 4.94\times10^7 & 0.0 \\ 9.42\times10^4 & 6.74\times10^5 & 0.0 & -9.38\times10^6 & 1.50\times10^6 & 0.0 \\ 0.0 & 0.0 & 1.57\times10^5 & 0.0 & 0.0 & 1.17\times10^5 \\ -1.49\times10^6 & -9.38\times10^6 & 0.0 & 1.33\times10^8 & -2.33\times10^7 & 0.0 \\ 4.94\times10^7 & 1.50\times10^6 & 0.0 & -2.33\times10^7 & 7.71\times10^8 & 0.0 \\ 0.0 & 0.0 & 1.17\times10^5 & 0.0 & 0.0 & 7.16\times10^7 \end{bmatrix} \tag{4.81}$$

First a convergence study of MSG analysis is conducted using three different mesh configurations as listed in Table 4.2. The $r_{\min}$ and $t_{\min}$ represent the minimum element size along the radial direction and tangential direction respectively. The computation time consumed for both homogenization and dehomogenization by SwiftComp are also listed in Table 4.2. Fig. 4.15 shows the configuration of Mesh 2, with 2240 8-noded second-order quadrilateral elements (MSG S8R) on the cross section. Note that to capture the significant variation of stress/strain around the layer interface and the free-edge, refined meshes are adopted there. The results of interlaminar stress σ_{13} along radial direction on interface -45/45 are presented in Fig. 4.16, where the horizontal axis θ/θ_0 is the normalized central angle. Good agreement are shown among different meshes, even in the vicinity of the free-edge. This indicates that for MSG GTB model a relative coarse mesh is already capable of capturing the larger stress gradient due to free-edge effect. Considering the performance and efficiency, Mesh 2 is used in the 3D FEA model as the cross-sectional mesh. Table 4.3 compares the model size and computation cost of the MSG models and FEA models. It is shown that the number of elements of MSG models are orders of magnitude smaller than those of 3D FEA models. The implementation of 2D elements in the MSG models reduces the computation cost greatly.

Table 4.2.
Mesh configurations of curved beam cross section.

Mesh	Mesh 1	Mesh 2	Mesh 3
$r_{\min}$(mm)	0.06	0.06	0.038
$t_{\min}$(mm)	0.12	0.09	0.073
Node number	4489	6937	12281
Element number	1440	2240	4000
Computation time [GEB](s)	1.265	1.751	3.335
Computation time [GTB](s)	1.682	2.532	4.814

Using the mesh configuration in the MSG cross sectional analysis and 3D FEA as shown in Table 4.3, the interlaminar stress distribution σ_{13} along interface 45/90 of curved beam laminate from the two methods are extracted and compared in Fig. 4.17. At the free-edge ($\theta/\theta_0 = -1$) the interlaminar shear stress σ_{13} from MSG S8R and 3D

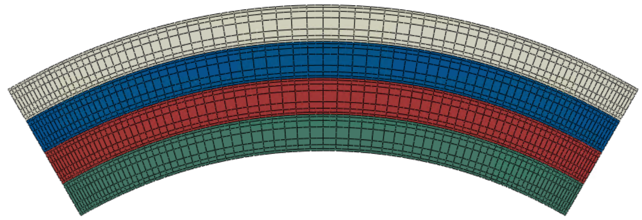

Fig. 4.15. A typical mesh (Mesh 2) of the 2D cross section of the curved beam laminate.

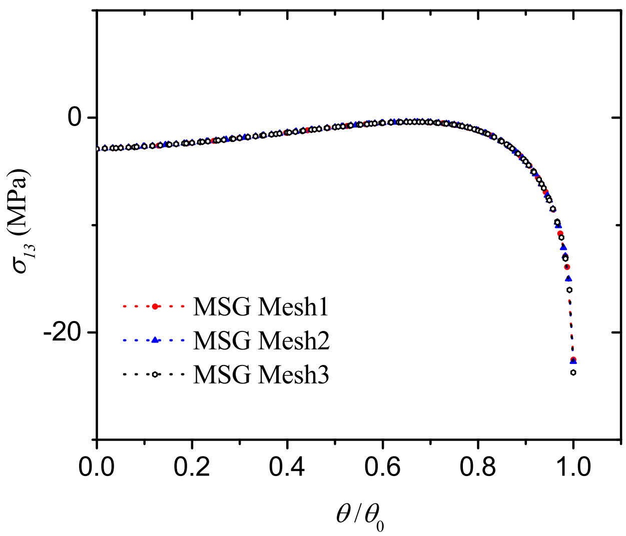

Fig. 4.16. Convergence study of interlaminar shear stress distribution along interface -45/45 of curved beam laminate under F_3°.

FEA C3D20R models are very close. It is noteworthy that, compared to the 3D FEA C3D8 model, σ_{13} at the free-edge from the model with MSG first-order element S4 is more close to the results from the models with second-order elements. This indicates that with the same cross section mesh configuration, MSG predicts more accurate interlaminar stress at the free-edge compared with 3D FEA, which means MSG can achieve a faster convergence. This is due to the semi-analytic nature of MSG that

Table 4.3.
Mesh configurations of curved beam cross section

Mesh	MSG S4	MSG S8R	3D FEA C3D8	3D FEA C3D20R
Node number	2349	6937	1,059,400	4,185,638
Element number	2240	2240	1,008,000	1,008,000
Computation time (s)	1.073	2.532	13,193	46,643

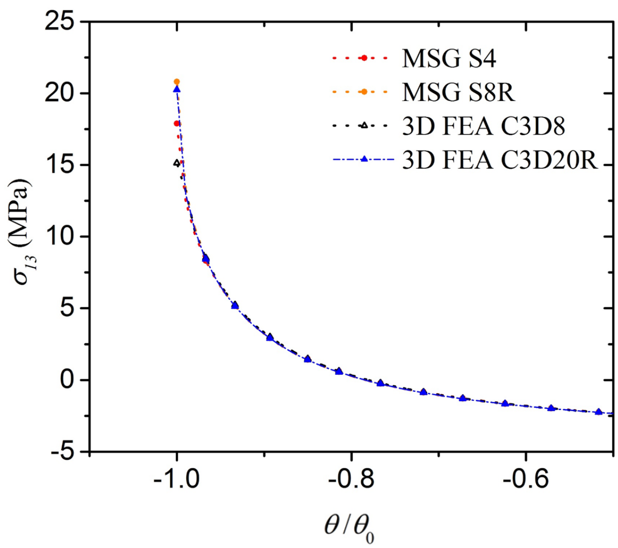

Fig. 4.17. Convergence study of σ_{13} distribution along interface 45/90 of curved beam laminate under F_3°.

the original problem is decoupled to an analytic geometrical nonlinear beam model and a cross-sectional analysis that is solved using FEM.

The contour plots of the interlaminar stresses are shown in Fig. 4.18. Stress concentration for interlaminar shear stress component σ_{13} exists at interface -45/45 around the free-edge. Similarly, relative large stress concentration for σ_{23} is shown at interface 45/90 near the free-edge. For both stress components, positive value is observed at one end while negative value at the other end with comparable magnitude, see Fig. 4.18(a) and 4.18(b). Fig. 4.18(c) shows that the interlaminar normal stress

σ_{33} distribution is almost symmetric about the $y_1 - y_3$ plane. Stress concentration exists at interface -45/45 near the free-edge.

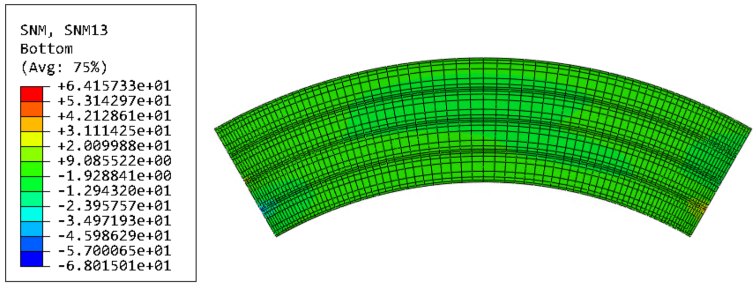

(a) σ_{13}

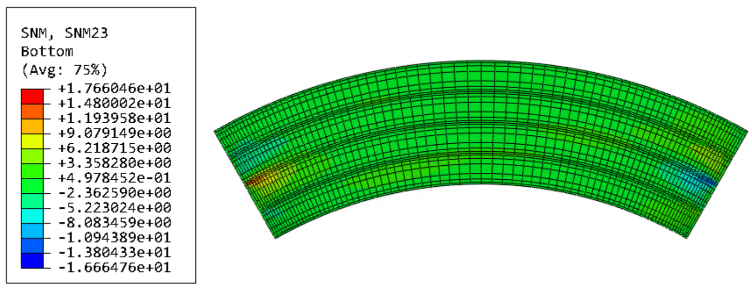

(b) σ_{23}

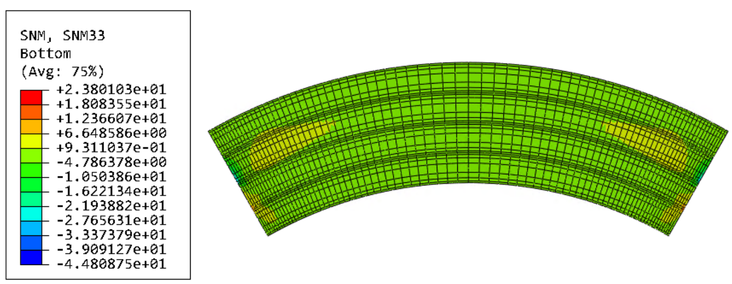

(c) σ_{33}

Fig. 4.18. Interlaminar stress contour plots of MSG under F_3°.

Interlaminar stress distribution from MSG and 3D FEA at the interfaces along the tangential directions are compared in Figs. 4.19, 4.20 and 4.21. In the figures, only the data paths at the right half portion of the interface are extracted to display the details more clearly. Results at the other half have similar characteristics. The stresses are extracted in the cylindrical coordinate system instead of the Cartesian coordinate system used in the simulation, so that all the interlaminar stress components are along or normal to the interlaminar surfaces. For all the interlaminar shear and normal stress components, high stress gradient and stress concentration can be observed near the free-edge, whereas the stresses almost vanish when away from the free-edge area. The stress variation at interfaces -45/45 and 45/90 is much more drastic compared with that at interface 90/0. Plots from MSG GTB model match very well with the 3D FEA model, even at the free-edge.

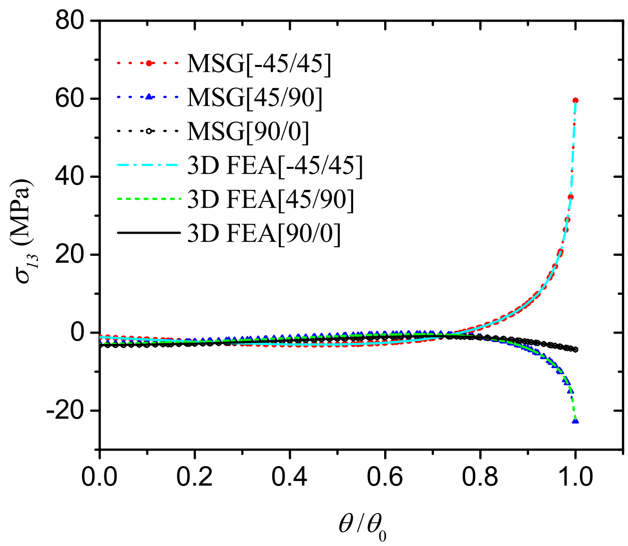

Fig. 4.19. Interlaminar shear stress σ_{13} distribution along the width of curved beam under F_3°.

Interlamiar shear and normal stresses along the free-edge are plotted in Fig. 4.22 and 4.23. It is clearly shown that high stress gradient exits around the layer interface due to abrupt change of material orientation crossing it. Fig. 4.22 shows that σ_{13} is nearly zero for the two top layers while positive for the two bottom layers. With respect to σ_{33} as shown in Fig. 4.23, it is approximately zero for the -45 deg and 0 deg layers, compressive for the 90 deg layer, and tensile for the 45 deg layer.

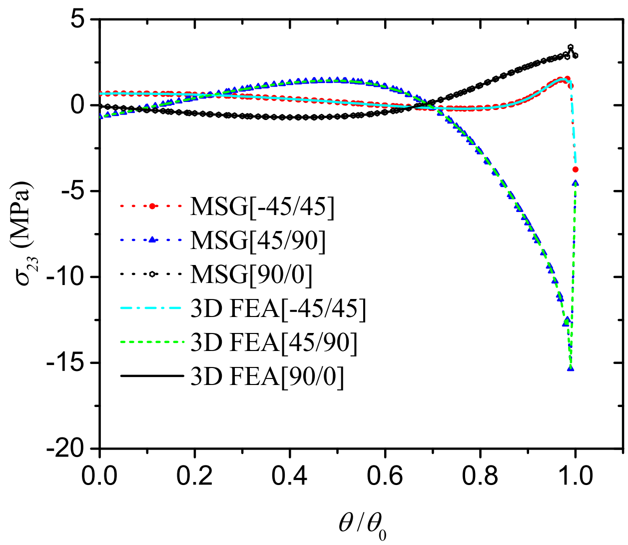

Fig. 4.20. Interlaminar shear stress σ_{23} distribution along the width of curved beam under F_3°.

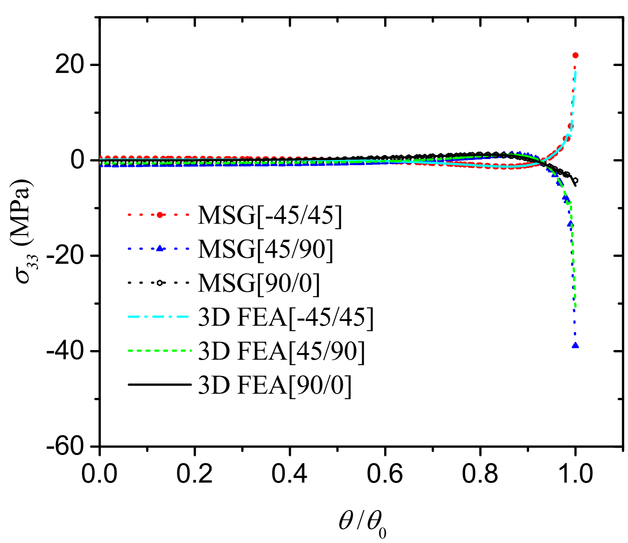

Fig. 4.21. Interlaminar normal stress distribution along the width of curved beam under F_3°.

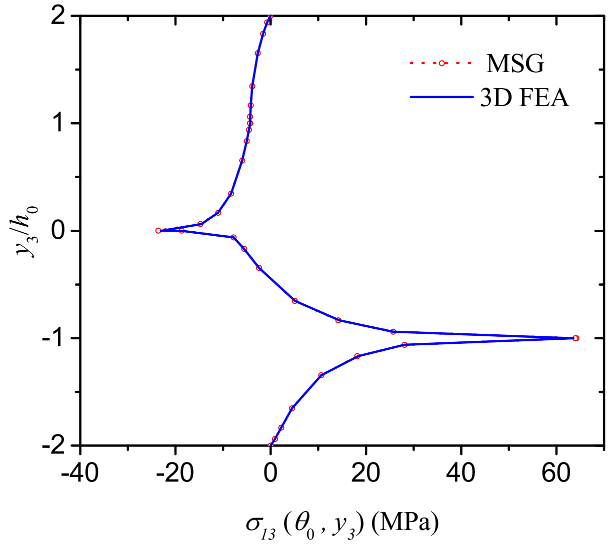

Fig. 4.22. σ_{13} distribution at the free-edge of curved beam under F_3°.

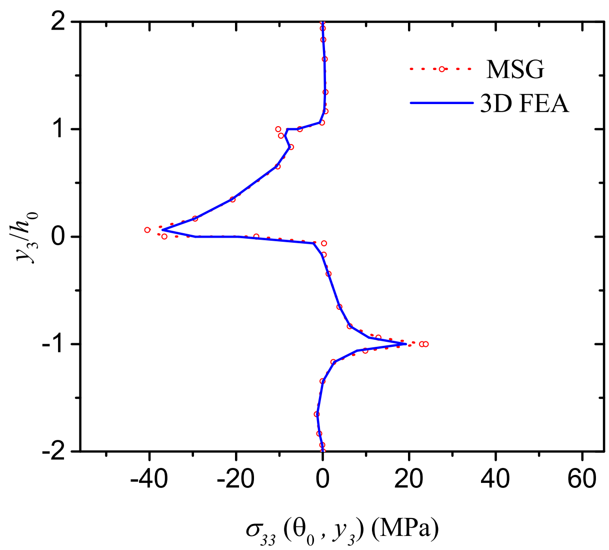

Fig. 4.23. σ_{13} distribution at the free-edge of curved beam under F_3°.

For comparison purpose, a GEB model is also implemented for the free-edge stress analysis. The recovered stresses are compared with those from the GTB model and the 3D FEA, as shown in Fig. 4.24 and Fig. 4.25 . It is clear from both comparison plots that the stresses from the GTB model agree very well with that from 3D FEA at all regions of the cross section. In contrast, obvious deviation around the center region is seen for the MSG GEB model. However, overall the free-edge stresses from the GEB model is not far away from the result of 3D FEA in this case because shear force is not the key factor introducing the free-edge stresses under load F_3 compared with the bending moment. In the region away from the free-edge, σ_{13} recovered from the GEB model is not accurate, since in the GEB model the internal shear force cannot be taken into account, only the internal bending moment is considered.

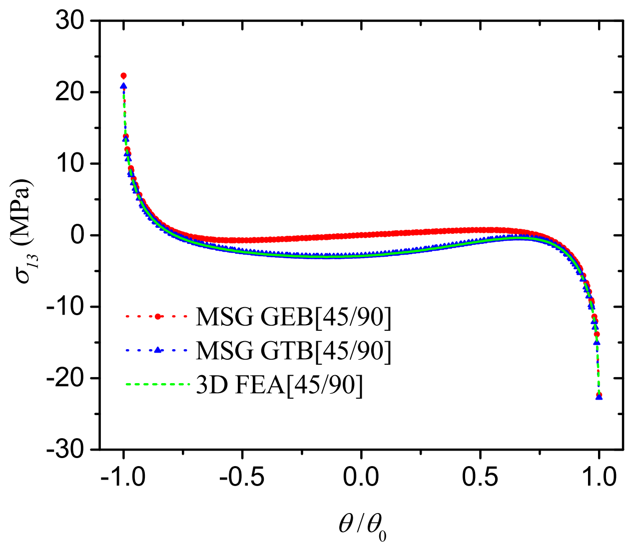

Fig. 4.24. σ_{13} distribution of a curved beam under F_3° at the interface 45/90.

4.3.4 Laminate of Curved Cross Section under F_2°

The GEB theory seems good enough to predict the free-edge stresses under shear force F_3, however this conclusion cannot be generalized to all the load cases when shear loads exist. The generalized Timoshenko beam model of MSG takes into account of the shear loads in its formulations, therefore it can accurately calculate the free-edge stresses. In this section, we use the same laminate of curved cross section model but

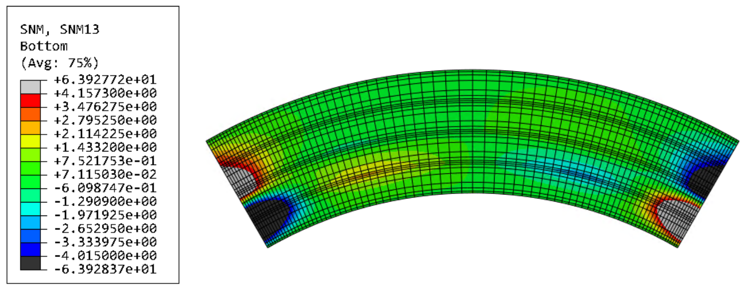

(a) GEB

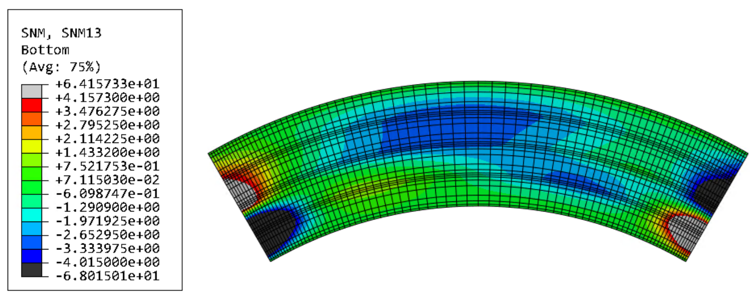

(b) GTB

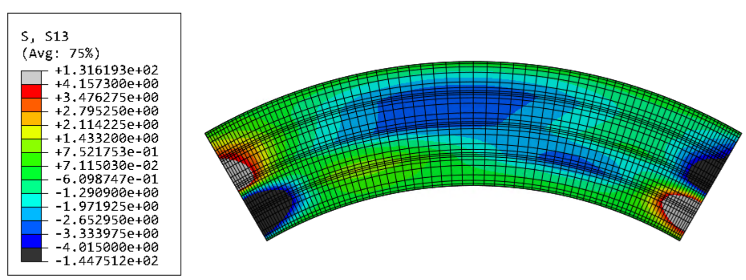

(c) 3D FEA

Fig. 4.25. σ_{13} contour plots of a curved beam under F_3°.

consider the load case $F_2^\circ = 100$ N. Figs. 4.26, 4.27, and 4.28 show the interlaminar shear stress σ_{13} along the width of different layer interfaces from the GTB model and the GEB model, as well as 3D FEA. It is observed that the GTB model can calculate all the stress components accurately while the GEB model produced errors compared with the 3D FEA results. This can also be observed from the contour plots in Fig. 4.25.

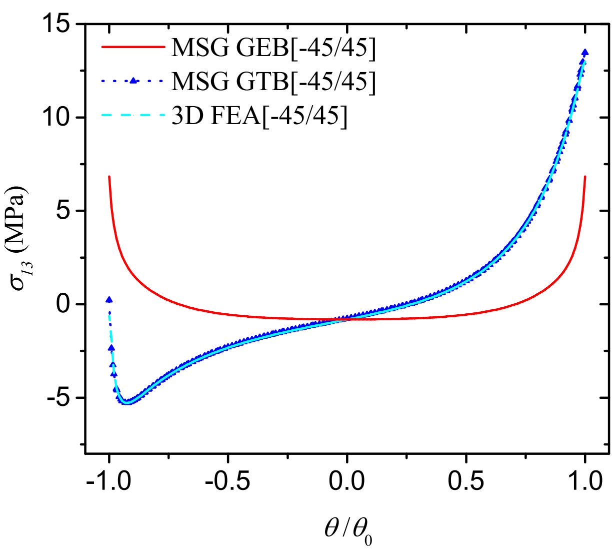

Fig. 4.26. σ_{13} distribution along the width of a curved beam under F_2° at the interface -45/45.

To be specific, as shown in Fig. 4.26 σ_{13} at interface -45/45 predicted by the GEB model is symmetric about the center ($\theta/\theta_0 = 0.0$) which is drastically in contrast to the prediction of the GTB model and 3D FEA. The results from GEB model significantly deviate from that of the GTB and 3D FEA, especially around the free-edge. Negative σ_{13} is predicted near the left free-edge from the GTB model and 3D FEA, while GEB model gives positive values. At interface 45/90 σ_{13} prediction from the GEB model about zero along the entire interface except near the free-edge, while the prediction from the GTB model and 3D FEA gradually increases from negative to positive from the left free-edge to the right free-edge, see Fig. 4.27. The

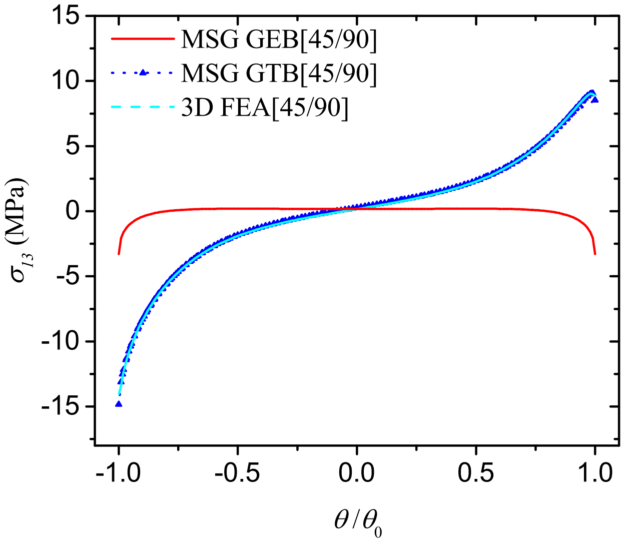

Fig. 4.27. σ_{13} distribution along the width of a curved beam under F_2° at the interface 45/90.

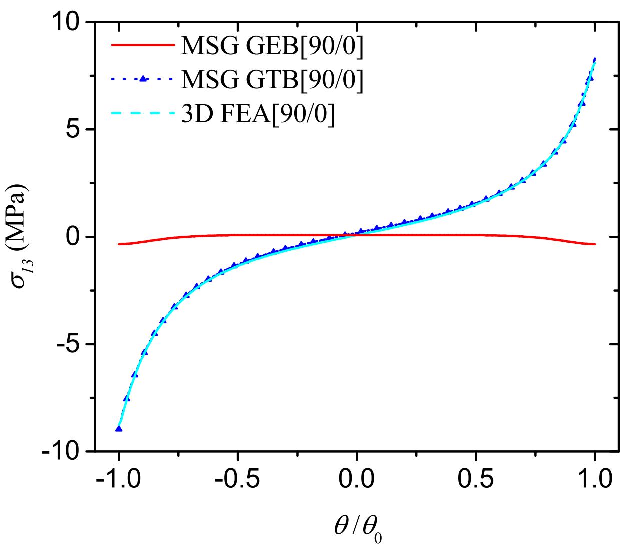

Fig. 4.28. σ_{13} distribution along the width of a curved beam under F_2° at the interface 90/0.

magnitude of GEB prediction is multiple times smaller than that of the other two models, especially around the free-edge. The prediction of σ_{13} at interface 90/0, as shown in Fig. 4.28, from the GEB model is nearly zero, while the GTB model and 3D FEA predict significant variation from the left to the right free-edge.

Contour plots of shear stress σ_{23} and normal stress σ_{33} are shown in Figs. 4.29 and 4.30, compared the results from the GEB model, the GTB model, as well as 3D FEA. Significant stress concentration is predicted at layer interfaces around the free-edge by the GTB model and 3D FEA. However, the stress concentration predicted by the GEB model is relatively small. To see this more clearly, the interlaminar stress σ_{23} and σ_{33} are extracted along interface 45/90, as shown in Figs. 4.31 and 4.32. It is clear that the GEB prediction fails to capture the high stress concentration near the free-edge, as well as the stress σ_{33} at the center section, while very good predictions are given by the GTB model.

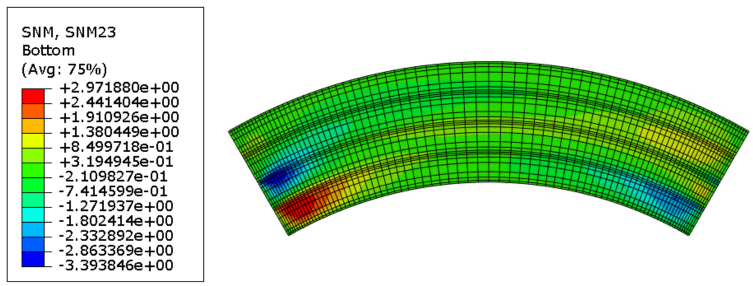

(a) GTB

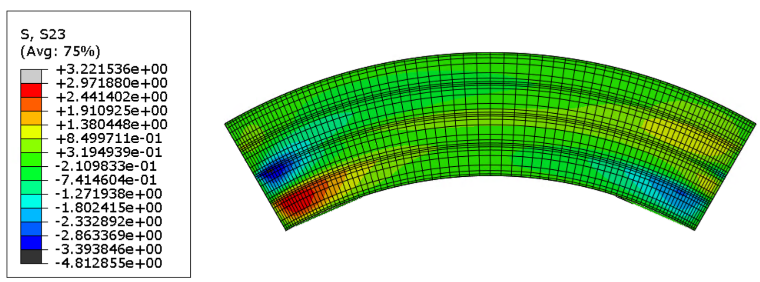

(b) 3D FEA

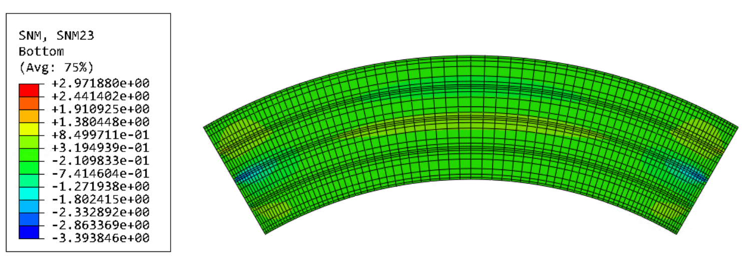

(c) GEB

Fig. 4.29. σ_{23} contour plots under shear force F_2°.

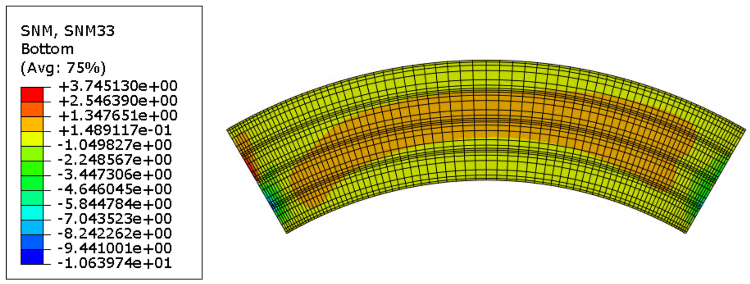

(a) GTB

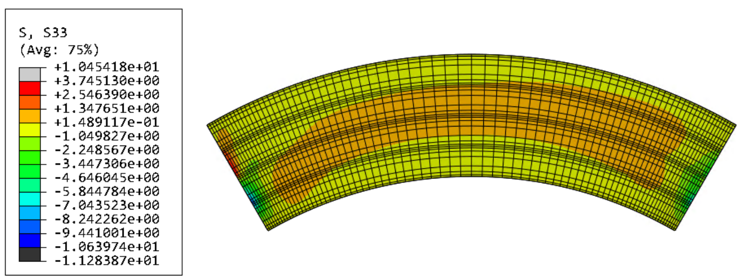

(b) 3D FEA

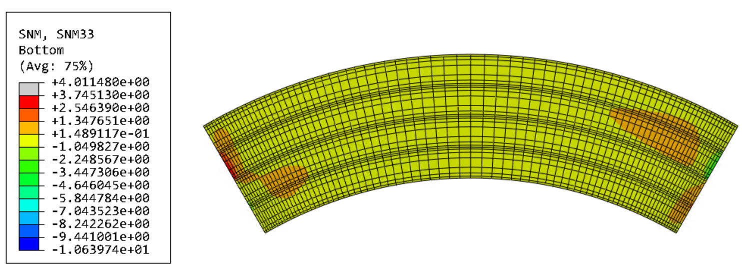

(c) GEB

Fig. 4.30. σ_{33} contour plots under shear force F_2°.

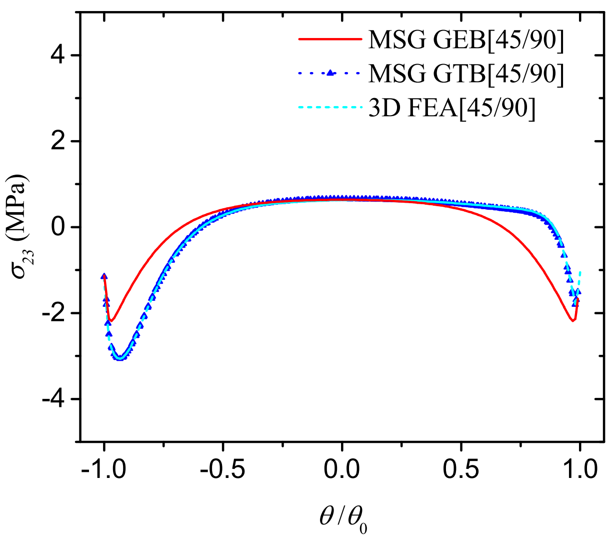

Fig. 4.31. σ_{23} distribution at the interface 45/90 of a curved beam under shear force F_2°.

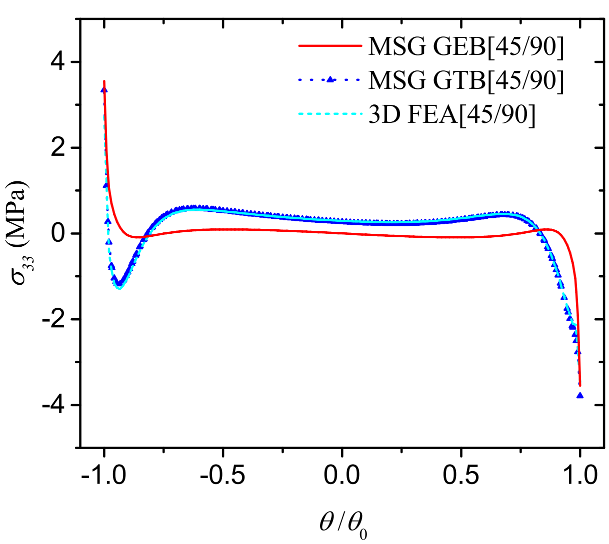

Fig. 4.32. σ_{33} distribution at the interface 45/90 of a curved beam under shear force F_2°.

4.4 Summary

The present work demonstrated that the MSG cross sectional analysis can be used to solve general free-edge stress problems of composite laminates. MSG can handle long laminates with arbitrary cross sections and layups subjected to combined mechanical loads including extension, shear forces, bending moments, and torque, and it does not require the laminate subjected to constant loads along the x_1 direction as what has been usually assumed in existing approaches based on Q3D models. Compared with approaches based on 2D plate models, in the formulation of MSG no ad hoc assumptions on displacement or stress are used. In addition, there is no restriction on the geometry of the cross section of the laminate.

It is found that SwiftComp provides an effective tool for general free-edge stress analysis for composite laminates which can achieve the accuracy of the much more expensive 3D FEA at the efficiency of simple 2D cross-sectional analyses. The functionality to deal with 3D SG implementing the GTB model is implemented in SwiftComp, which provided higher accuracy compared with the GEB model in the free-edge stress analysis. When the same cross section mesh is implemented in the MSG and 3D FEA model, MSG can converge faster with regard to the mesh density due to its semi-analytic nature.

From the numerical examples of free-edge analysis, it can also be concluded that the internal bending moment plays a more important role than the internal shear force in the surge of the interlaminar stress at the free-edges. However, the shear force still should not be ignored in the free-edge analysis.

5. FAILURE ANALYSIS OF COMPOSITE BEAM-LIKE STRUCTURES

5.1 Introduction

The heterogeneity of the composite structures can be shown at two levels: at the material level such as composite laminates, and at the structural level such as sandwich beams. Heterogeneous materials show complicated failure features in contrast to homogeneous materials. The constituents of the heterogeneous structures have different failure modes which can interact with each other to form more complex failure modes due to the interface properties, volume fraction and loading conditions. The most simple example is unidirectional fiber-reinforced composite lamina. The main failure modes are fiber breakage/microbulkling, fiber pulling out, matrix cracking, interfacial debonding and delamination, etc. Heterogeneous materials can have hierarchical structures. For example, woven composites can be viewed as a layup structure with each layer composed of UCs, and each UC are comprised of yarns and matrix. For woven composites, delamination and kink band formation in compression, tow rupture and pullout in tension, and combinations of these in bending also need to be considered. The progressive failure process of composite structures usually results in a great potential for damage tolerance [171]. If heterogeneity at the structural level is considered, many more failure modes can be introduced which are resulted from the multiscale features involved. For example, stiffened sandwich structures may have complicated failure mechanisms such as skin-stiffener separation and local bulking. It is difficult to include all the failure modes in a model, therefore it is important to conduct failure analysis at the length scale interested.

In this chapter we will study failure initiation of heterogeneous beam-like structures based on the stress analysis of MSG outlined in Chapter 4. To begin with, for completeness failure theories for orthotropic materials are briefly introduced. Following that is the prediction of the failure strength of the beam-like structures in terms of the maximum forces and moments, which corresponds to the prediction of the failure strength of heterogeneous materials in terms of maximum stresses. At last, a numerical example of a composite grid-stiffened cylinder beam-like structures is given to show its effectiveness of this method.

5.2 Failure Criteria of Composite Materials

In the initial failure analysis of materials, different failure criteria are used to determine the failure index and failure envelop. The material is safe when the failure index $f < 1$ within the failure envelop.

There are many failure criteria in the literature for composite materials, of which the most widely used are maximum normal stress/strain criterion and maximum shear stress/strain criterion that apply to individual stress components, Tsai-Hill criterion and Tsai-Wu criterion that take into account the influence of different stress components, and Hashin criterion that can indicate the failure modes of composites. To demonstrate the capability of MSG stress analysis in failure strength prediction of beam-like structures, without loss of generality, in next section we will take the maximum stress criterion and Tsai-Wu criterion as examples. The two failure criterion are introduced briefly as follows for completeness.

The maximum stress failure criterion is a combination of the maximum normal stress criterion and maximum shear stress criterion. It assumes that material failure happens when the absolute value of a stress component exceed its corresponding strength. This criterion differentiates the normal failure modes of tensile and compressive loading and the shear failure modes. To be specific, the material will fail if any of the following conditions stands

$$f = \frac{\sigma_{11}}{X_1} = 1 \qquad f = \frac{\sigma_{22}}{X_2} = 1 \qquad f = \frac{\sigma_{33}}{X_3} = 1 \tag{5.1}$$

when the normal stresses are tensile, and

$$f = \frac{|\sigma_{11}|}{X_1'} = 1 \qquad f = \frac{|\sigma_{22}|}{X_2'} = 1 \qquad f = \frac{|\sigma_{33}|}{X_3'} = 1 \tag{5.2}$$

when the normal stresses are compressive. In addition, the material fail in the shear modes if any of the following conditions holds

$$f = \frac{|\sigma_{23}|}{R_{23}} \qquad f = \frac{|\sigma_{13}|}{R_{13}} \qquad f = \frac{|\sigma_{12}|}{R_{12}} \tag{5.3}$$

Note that here σ_{ij} are stress components in the local material coordinate system. For orthotropic materials, since the strengths of different stress component at different directions are not the same, the principal stress concept is not implemented in the failure criterion. The tensile strengths are denoted as X_1, X_2, X_3, while the corresponding compressive strengths are X_1', X_2', and X_3'. Furthermore, R_{23}, R_{13}, and R_{12} denote the shear strengths on the three principal symmetry planes of the material. It should be emphasized that failure criteria are based on stress/strain components on the local material coordinate systems. Consequently, attention should be paid when the material coordinate system is not aligned with the global coordinate systems. In this case, the stress/strain components should be transformed to the local material coordinates before applying these failure criteria. However, it is incorrect to transform the strength values (X_1, X_2, X_3, etc.) from the material coordinate system to the global coordinate system. The correctness of the transforming of stress/strain is based on its tensorial nature. The strengths are not components of a tensor, but represent different physical states of the material [171].

The Tsai-Wu failure criterion is a generalization of the Tsai-Hill criterion that differentiates the tensile and compressive strengths. The Tsai-Wu failure surface is characterized by a polynomial function of the stress components that includes both linear and quadratic terms. To be specific, the material will fail if

$$\begin{aligned} f =& F_1\sigma_{11} + F_2\sigma_{22} + F_3\sigma_{33} + F_{11}\sigma_{11}^2 + F_{22}\sigma_{22}^2 + F_{33}\sigma_{33}^2 + 2F_{12}\sigma_{11}\sigma_{22} \\ &+ 2F_{13}\sigma_{11}\sigma_{33} + 2F_{23}\sigma_{22}\sigma_{33} + F_{44}\sigma_{23}^2 + F_{55}\sigma_{13}^2 + F_{66}\sigma_{12}^2 = 1 \end{aligned} \tag{5.4}$$

where F_i and F_{ij} are material parameters that depend on the various material strengths, i.e.

$$F_1 = \frac{1}{X_1} - \frac{1}{X_1'} \qquad F_2 = \frac{1}{X_2} - \frac{1}{X_2'} \qquad F_3 = \frac{1}{X_3} - \frac{1}{X_3'} \tag{5.5}$$

$$F_{11} = \frac{1}{X_1 X_1'} \qquad F_{22} = \frac{1}{X_2 X_2'} \qquad F_{33} = \frac{1}{X_3 X_3'} \tag{5.6}$$

$$F_{44} = \frac{1}{R_{23}^2} \qquad F_{55} = \frac{1}{R_{13}^2} \qquad F_{66} = \frac{1}{R_{12}^2} \tag{5.7}$$

and

$$2F_{12} = \frac{1}{X_3 X_3'} - \frac{1}{X_1 X_1'} - \frac{1}{X_2 X_2'} \tag{5.8}$$

$$2F_{13} = \frac{1}{X_2 X_2'} - \frac{1}{X_1 X_1'} - \frac{1}{X_3 X_3'} \tag{5.9}$$

$$2F_{23} = \frac{1}{X_1 X_1'} - \frac{1}{X_2 X_2'} - \frac{1}{X_3 X_3'} \tag{5.10}$$

5.3 Initial Failure Analysis of Composite Beam-like Structures

As shown in Chapter 4, the composite beam-like structures analysis can be separated into a macroscopic beam analysis and a constitutive modeling on the SG at the microscale. From the SG analysis the effective stiffness matrix of the beam and the dehomogenization relation can be obtained. For the GEB model, they are from Eq. (4.45) and Eq. (4.44). For the GTB model, they are obtained from Eq. (4.63) and Eq. (4.60). In the linear elastic regime, the 3D local strain Γ in the microstructure are linearly related with the macroscopic beam strain and curvatures $\bar{\epsilon}$ through Eq. (4.48) and Eq. (4.70) for GEB and GTB respectively. In addition, the 3D local stress σ can be obtained using Eq. (4.49).

From the macroscopic beam analysis, the internal load F_R can be calculated, as well as the beam strain and curvatures $\bar{\epsilon}$ using Eq. (4.71). For GEB model, $F_R = \lfloor\, F_1 \;\; M_1 \;\; M_2 \;\; M_3 \rfloor^{\mathrm{T}}$. For GTB model, shear forces F_2 and F_3 are also included, and thus $F_R \equiv \lfloor\, F_1 \;\; F_2 \;\; F_3 \;\; M_1 \;\; M_2 \;\; M_3 \rfloor^{\mathrm{T}}$. Note that the strain $\mathcal{E}$ introduced by the applied load is not considered.

Therefore, based on the SG constitutive modeling, the following linear relation between F_R and σ can be written as

$$\sigma = f_{F\sigma} F_R \tag{5.11}$$

The initial failure analysis then can be carried out at the microstructure with various failure criterion of materials. Under a given F_R, the failure index can be obtained in the microstructure.

In composite structures, the initial failure load P_{cr} is defined as the load under which the maximum failure index in the structure reaches 1. From the linear relation of Eq. (5.11), for any load P on a structure, when $f \neq 1$, the load P can be increased or decreased by a ratio of α so that when $P_{cr} = \alpha P$ the maximum failure index equals to 1. Corresponding to any F_R, a P_{cr} can be calculated. It is obvious that P_{cr} of all the possible F_R can define a volume of six dimensionality for a GTB model, within which the GTB structure is safe. When a single component F_i in F_R is considered, the P_{cr} could be viewed as the strength of the beam in the same fashion of the strength for materials. When two load components (F_i, M_j) are considered, the failure envelop of these two components can be obtained.

To calculate the P_{cr} corresponding to a certain load F_R, first the failure index field in the SG under F_R can be calculated, followed by a step to determine the α corresponding to this load condition. For a failure criterion which is linear with respect to the stress field, such as the max stress failure criterion,

$$f(\alpha\sigma_{ij}) = \alpha f(\sigma_{ij}) \tag{5.12}$$

Since material is defined to fail at $f = 1$,

$$\alpha = \frac{1}{f} \tag{5.13}$$

Inside the microstructure, the most dangerous point has the maximum f and the smallest strength ratio, denoted as α_{min}, therefore

$$F_{cr} = \alpha_{min} F_R \tag{5.14}$$

If the failure criterion in the microstructure used is not linear, the strength ratio α need to be redefined. The procedure to calculate α in Tsai-Wu failure criterion is illustrated in [171] in detail. Here the results are listed for completeness. First Tsai-Wu failure criterion can be rewritten in the following form.

$$f(\alpha\sigma_{ij}) = \alpha^2 a + \alpha b = 1 \tag{5.15}$$

where

$$a = F_{11}\sigma_{11}^2 + F_{22}\sigma_{22}^2 + F_{33}\sigma_{33}^2 + 2F_{12}\sigma_{11}\sigma_{22} + 2F_{13}\sigma_{11}\sigma_{33} \tag{5.16}$$

$$+ 2F_{23}\sigma_{22}\sigma_{33} + F_{44}\sigma_{23}^2 + F_{55}\sigma_{13}^2 + F_{66}\sigma_{12}^2 \tag{5.17}$$

and

$$b = F_1\sigma_{11} + F_2\sigma_{22} + F_3\sigma_{33} \tag{5.18}$$

where a, b are computed based on the local 3D stress state of the microstructure when macroscopically the beam has a internal load F_R. Then, α can be solved as

$$\alpha = \frac{-b \pm \sqrt{b^2 + 4a}}{2a} \tag{5.19}$$

Only the positive solution is meaningful and should be kept. If the calculated α is negative, implying the material will not fail, then $\alpha = +\infty$. In this case F_{cr} can be estimated using Eq. (5.14).

Since F_R can be an arbitrary load condition, this procedure can be applied to calculate the strength and failure envelop of any combination of two load components. The procedure of a MSG failure analysis of composite beam-like structures then can be described as the following

1. Identify the smallest building block of the beam-like structure as the SG.
2. Perform a homogenization analysis over the SG, from which the effective beam properties will be obtained, along with the dehomogenization relations that can be used to recover the local fields.
3. Solve the 1D beam problem subject to loads.

4. At the location of interest, perform a dehomogenization analysis to obtain the local fields such as stresses and strains with the internal loads or beam strains and curvatures obtained in the previous step as the inputs.

5. Predict the failure index, then the initial failure load and failure envelop based on various failure theories, such as the maximum stress and the Tsai-Wu criteria, with the local fields recovered from the dehomogenization as the inputs.

It is noted that to predict the strengths or failure envelop of the beam structure, an arbitrary magnitude of F_i or (F_i, M_j) can be used in step 4, therefore step 3 is not necessary if only require the strengths and the failure envelop.

5.4 Numerical Example

Without loss of generality, a composite grid-stiffened (CGS) cylinder (from [172]) is studied to evaluate the accuracy of the failure analysis based on the generalized Timoshenko beam (GTB) model in this section. As shown in the Fig. 5.1, the CGS cylinder is made of a laminate shell and stiffeners. The shell laminate has a thickness of 0.09 in and layup sequence of $[45/45/90/0/45]_S$ with a ply thickness of 0.009 in. The shell is stiffened by three types of stiffeners: helical, longitudinal and circumferential, in which the helical angle is 45 degree and the number of stiffeners circumferentially is 12. The width and depth of all stiffeners is 0.18 in. The material of the cylinder is the same as the laminate in the fiber direction. The same finite element mesh size and element type is used in the 3D SG as the detailed FEA. The material used in the stiffeners and shell is E-glass 21xK43 Gevetex/LY556/HT907/DY063 epoxy [173]. The material properties are given in Table 5.1, where the subscripts 1, 2, and 3 indicate the principal material coordinates. X_1, X_1', X_2 and X_2' are the tensile and compressive strengths in the corresponding directions and R_{23}, R_{12}, R_{13} are the shear strengths.

For this specific CGS cylinder, the beam stiffness matrix is shown in Eq. (5.20). It is seen that the shear-bending is captured by the GTB model, which is not available

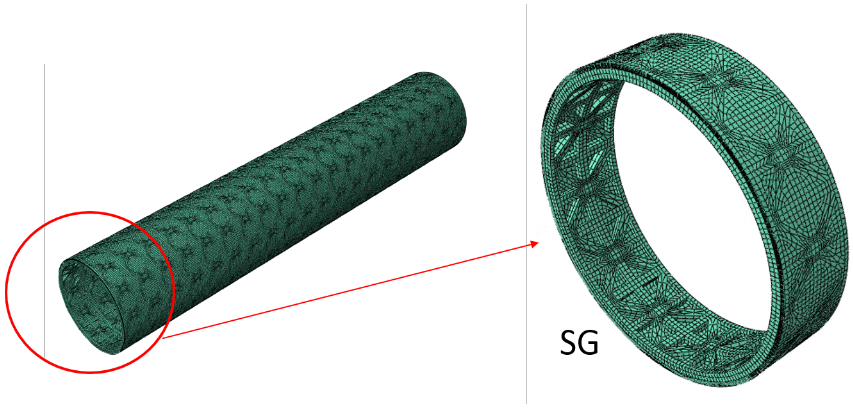

Fig. 5.1. The CGS cylinder and the corresponding SG [172]

Table 5.1.
Material properties of E-glass 21xK43 Gevetex/ LY556/HT907/DY063 epoxy.

Mechanical properties	Values	Strength properties	Values
E_1	6.610×10^6 psi	X_1	1.856×10^5 psi
$E_2 = E_3$	2.350×10^6 psi	X_1'	1.160×10^5 psi
$G_{12} = G_{13}$	8.460×10^5 psi	$X_2 = X_3$	5.802×10^3 psi
G_{23}	8.460×10^5 psi	$X_2' = X_3'$	2.103×10^4 psi
$\nu_{12} = \nu_{13}$	0.278	R_{23}	1.059×10^4 psi
ν_{23}	0.389	$R_{12} = R_{13}$	1.059×10^4 psi

in the GEB model. Using the effective beam stiffness matrix, macroscopic beam strains can be calculated under different external loads, which, in turn, can be used to dehomogenize the corresponding local stress fields. Strengths of the CGS cylinder are given in Table 5.2 for the maximum stress criterion and Table 5.3 for the Tsai-Wu criterion. Direction 1 of the CGS cylinder is in its axial direction, while directions 2 and 3 denote its radial directions. In Tables 5.2 and 5.3 the symbols '+' and '-' mean that the corresponding loads are in the positive and the negative coordinate directions, respectively. Due to symmetry of the structure the predicted strengths under bending moments M_2 and M_3 are identical, no matter it is applied in the positive or negative coordinate direction. The same conclusion applies to the transverse forces. Different strengths are predicted for torques in positive and negative coordinate directions, and also for tensile and compressive axial forces, due to the unsymmetrical layup sequence of the laminates and different tensile and compressive material strengths as shown in Table 5.1. For this CGS cylinder, the compressive axial strength is almost four times of the tensile strength according to both failure criteria, while the maximum allowable torque in the clockwise direction is 40% bigger than that in the counterclockwise direction. In addition, the strengths predicted by both failure criteria are close to each other.

$$D = \begin{bmatrix} 1.19\times10^7 & 0.0 & 0.0 & -8.14\times10^5 & 0.0 & 0.0 \\ 0.0 & 2.15\times10^6 & 0.0 & 0.0 & 3.98\times10^5 & 0.0 \\ 0.0 & 0.0 & 2.15\times10^6 & 0.0 & 0.0 & 3.98\times10^5 \\ -8.14\times10^5 & 0.0 & 0.0 & 3.76\times10^7 & 0.0 & 0.0 \\ 0.0 & 3.98\times10^5 & 0.0 & 0.0 & 5.13\times10^7 & 0.0 \\ 0.0 & 0.0 & 3.98\times10^5 & 0.0 & 0.0 & 5.13\times10^7 \end{bmatrix} \tag{5.20}$$

Table 5.2.
Strengths of CGS cylinder: Max stress failure criterion.

Direction	F_1 (lb)	$F_2 = F_3$ (lb)	M_1(lb·in)	$M_2 = M_3$ (lb·in)
+	1.498E+04	8.782E+03	5.144E+04	2.281E+04
-	5.430E+04	8.782E+03	7.073E+04	2.281E+04

Table 5.3.
Strengths of CGS cylinder: Tsai-Wu failure criterion.

Direction	F_1 (lb)	$F_2 = F_3$ (lb)	M_1(lb·in)	$M_2 = M_3$ (lb·in)
+	1.483E+04	8.392E+03	4.917E+04	2.258E+04
-	5.690E+04	8.392E+03	6.530E+04	2.258E+04

Two loading cases are used for the comparison between the initial failure analysis of the MSG model and the detailed 3D FEA model. The first loading case is an axial tensile force $F_1 = 10,000$ lb and a twisting moment $M_1 = 20,000$ lb·in. In the second case the CGS cylinder is subjected to a combination of axial tensile force $F_1 = 10,000$ lb and bending moment $M_2 = 20,000$ lb·in. The failure index contours from MSG analysis and detailed 3D FEA are compared in Fig. 5.2(a) and 5.2(b) for loading case 1 and 2, respectively, with the maximum stress failure criterion. It is clear that the predicted index contour from MSG are very close to that of 3D FEA, especially for loading case 2 with applied axial force and bending moment. The failure index contour shows that the cylinder has already failed for loading case 2 while remains safe under loading case 1. The critical paths where the failure index achieves maximum are shown as solid black lines in Fig. 5.2(a) and 5.2(b). Along these two critical lines the failure index are extracted from both MSG and 3D FEA models and plotted in Fig. 5.3. Predictions from both maximum stress and Tsai-Wu criteria are included. In the plots the horizontal axis is the local path coordinate starting from the inner cylindrical surface and ending at the outer cylindrical surface. For both loading cases and both failure criteria, the failure index predictions from MSG overlap with that from the detailed 3D FEA model along the entire critical path line.

For heterogeneous beam-like structures, failure envelopes of different combination of internal loads are especially useful. Hence, the failure envelopes for the two loading cases are also calculated, as shown in Fig. 5.4. The dehomogenization relation from MSG analysis is solely determined by the SG selected. Consequently, for a given SG, the microscale fields such as stress and strain can be uniquely calculated by the macro strains, which in turn depend on the sectional forces and moments. Therefore, failure criteria from MSG analysis for beam-like structures can be established based on the internal forces and moments. As expected, Fig. 5.4 shows that loading case 1 is within the predicted failure envelope while loading case 2 is outside. It is interesting to note that for the CGS cylinder structure the failure envelope in the F_1-M_2 plane is a parallelogram for both maximum stress and Tsai-Wu criteria, which is similar to the

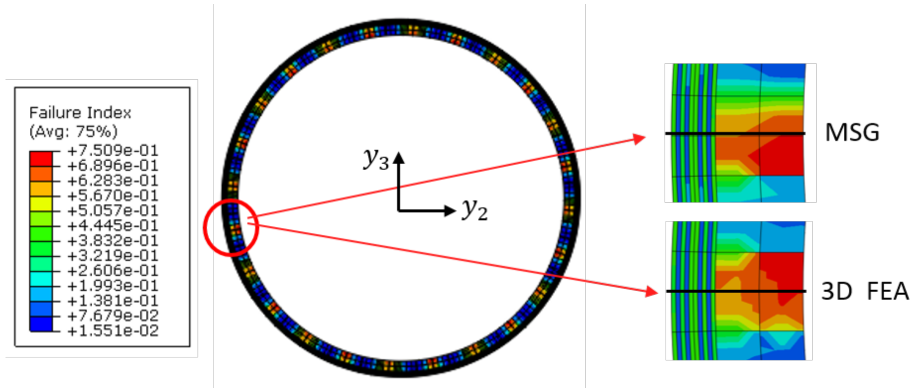

(a) Loading case 1 with axial force F_1 and torque M_1.

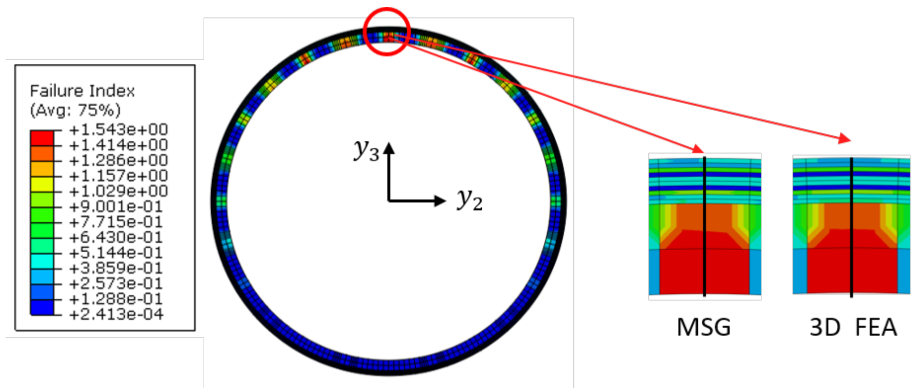

(b) Loading case 2 with axial force F_1 and bending moment M_2.

Fig. 5.2. Failure index contour plots from MSG and detailed 3D FEA analyses.

failure envelopes in the σ_1-σ_2 plane for homogeneous materials. In the loading cases with external axial force and twisting moment, the predicted failure envelope has a more irregular shape. It is noted that the predicted F_1-M_1 envelopes for maximum stress and Tsai-Wu criteria on the half plane with tensile axial force F_1 are closer than that on the other half plane (see Fig. 5.4(a)).

5.5 Summary

Based on the capability of MSG to predict local fields with high precision, new forms of failure criteria is presented in this chapter for heterogeneous beam-like struc-

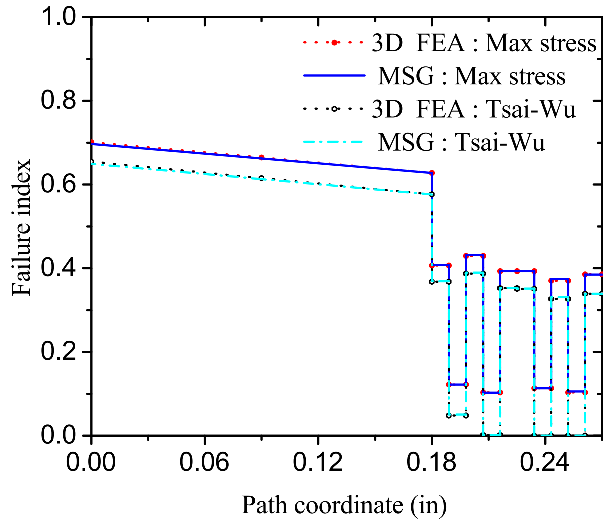

(a) Loading case 1 with axial force F_1 and torque M_1.

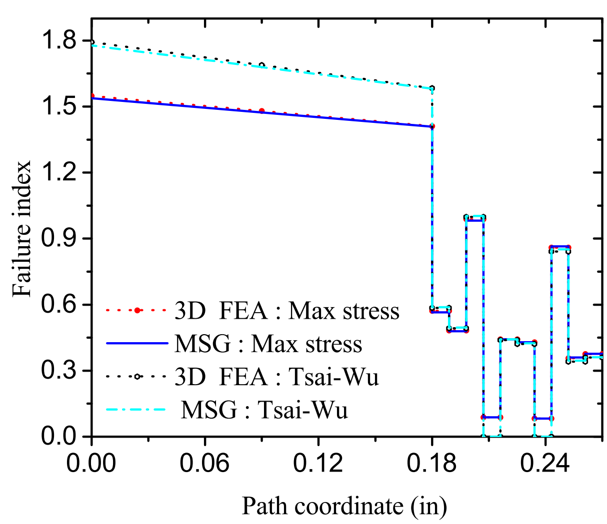

(b) Loading case 2 with axial force F_1 and bending moment M_2.

Fig. 5.3. Failure index along the critical radial path line.

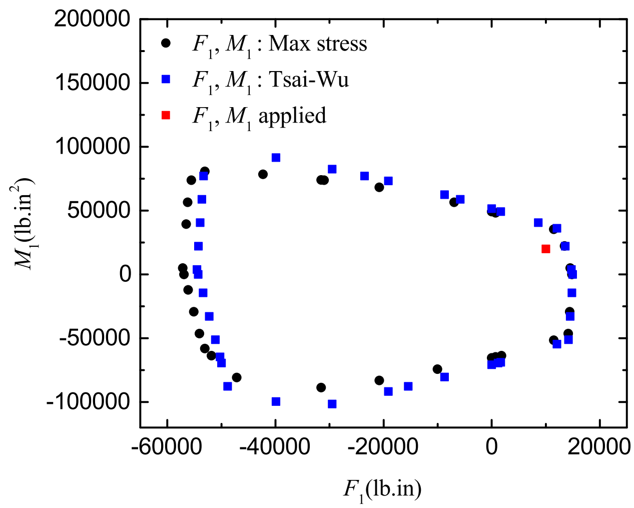

(a) Loading cases with axial force F_1 and torque M_1.

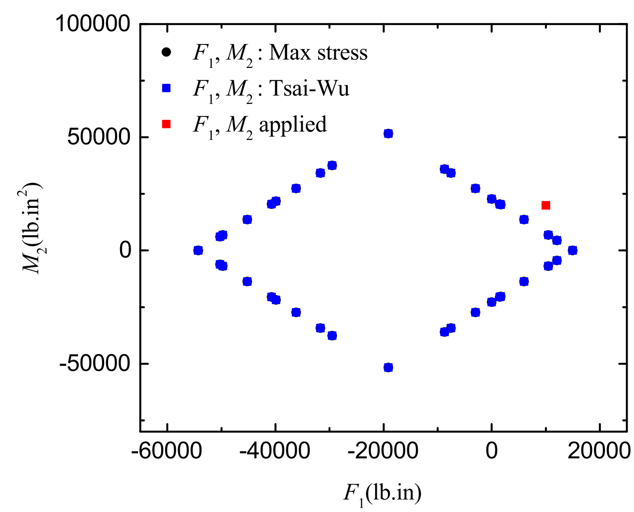

(b) Loading cases with axial force F_1 and bending moment M_2.

Fig. 5.4. Failure envelope predictions.

tures. Within the framework of MSG, for a given SG the newly developed forms of failure criteria are based on sectional forces and moments. Traditional widely used failure criteria, such as maximum stress and Tsai-Wu that rely on local stress/strain states, can be easily recast to the form of sectional forces and moments. Failure envelopes that are important in engineering applications can be readily calculated on different sectional forces and/or moment planes. Comparison with failure strength predictions from detailed 3D FEA shows that the new formulations from MSG are capable of obtaining high precision. An advantage of the MSG procedure over 3D FEA is its minimum computational cost, thus greatest efficiency, and directly linking microstructural details with global beam behaviors.

6. CONCLUSIONS AND FUTURE WORK

6.1 Conclusions

Multiscale methods are usually developed following a bottom-up scenario based on the assumption that length scales are well separated. In contrast to following a bottom-up scenario, MSG is a top-down theory that develop the macroscopic structural model and the micromechanics model simultaneously. In this work, by extending MSG and its companion code SwiftComp, two problems arise from the ambiguous scale separation in multiscale simulation are tackled.

First, the theory of MSG is extended for aperiodic heterogeneous solid structures when the microscopic periodicity is not preserved in all the three directions. A volume integral constraint is introduced to ensure the kinematics equivalence between the original heterogeneous material and the equivalent homogenized material based on the principle of minimum information loss and variational asymptotic method. As this theory does not require boundary conditions, one is free to choose the analysis domain of arbitrary shape that is not necessarily to be a cuboid. This theory can also handle periodic materials by enforcing the periodicity of the fluctuating functions, or use a combined constraints of PBCs and the volume integral constraint if the material is not fully periodic in three directions. For periodic structures, the effective properties obtained using the combined constraints will converge consistently to those obtained from using fully periodic constraints. The mathematical smallest building block of the heterogeneous structure, namely SG can still utilize the lowest dimension to describe the heterogeneity as for fully periodic materials.

RVE analysis and SG constitutive modeling are related and compared in this work. It is found that the volume integral constraint itself is equivalent to SUBCs in RVE analysis. When additional periodicity constraints are applied, the combined constraints are equivalent to the mixed boundary condition of SUBCs and PBCs in RVE analysis. The mixed constraints for RVE analysis are proved to satisfy the Hill-Mandel condition, although MSG can satisfy the Hill-Mandel condition automatically. In MSG, it is easier to apply the periodicity constraints since the macroscopic strains are not present in the constraints as they are in the RVE analysis. In addition, the recovery of the local fields involving no BVP solving process and thus more efficient.

This theory is enabled based on the FE method in SwiftComp, with an added option to use B-bar integration techniques in first order quadrilateral elements or brick elements to reduce volumetric locking, and enabled reduced integration techniques for second order 2D and 3D elements.

A few examples are analyzed with the extended MSG theory and compared with analytical solution, RVE analysis and 3D FEA results. Using CCA model, MSG predicted the exact effective properties when they exist and predicted the lower bound given by the analytic solution. Textile composites of finite thickness are also analyzed. It is shown that the proposed theory can naturally capture the influence of the finite thickness effect and inter-ply shifting to the effective properties and the local fields. In contrast, apparent error can be introduced if PBCs are applied in this case. In addition, with a example of a randomly distributed short fiber reinforced composite, it is demonstrated that MSG can conveniently analyze complicated microstructures that is difficult to generate periodic mesh, and obtain acceptable results.

Second, MSG is enabled to deal with Timoshenko beam-like structures with span-wise heterogeneity, which provide higher accuracy than the previous available Euler-Bernoulli beam model. Its reduced form, the MSG beam cross sectional analysis, is found to be able to analyze generalized free-edge problems with arbitrary layups and subjected to general loads. In this method, the only assumption applied is that the laminate is long enough so that the Saint-Venant principle can be adopted. There is no limitation on the cross section of the laminate since no ad hoc assumption is involved with the microstructure geometry. This method solve the free-edge problem from a multiscale simulation point of view, which is completely different from the massive available research works which design special quasi-3D models or using plate models based on ad hoc assumptions of local field distribution in the laminates. In contrast to the Q3D model, the deformation state is not necessarily to be x-independent. From the numerical results, the accuracy improvement using Timoshenko beam model is clearly shown compared with EulerBernoulli beam model, especially when transverse shear is significant in the deformation of the composite laminates.

At last, a strength analysis of a heterogeneous beam-like structure with spanwise heterogeneity is performed with MSG. The problem is separated to a failure analysis on the reference line of the beam at the macroscale and a constitutive modeling on the SG at the microscale. From the SG analysis, the relation between the internal loads of the beam and the local fields at the microscale can be obtained. In the linear elastic regime, the failure index of the beam-like structure linearly depends on the internal loads of the beam. Therefore, the initial failure analysis can be related with only the internal loads of the beam for a given heterogeneous beam. It can be used as a guidance in the microstructural design of beam-like structures. By an example of composite grid-stiffened cylinder beam-like structures, it is shown that the stress and failure index local fields agree very well with that from direct 3D FEA, which ensures the confidence of using the strength criterion obtained from the MSG analysis.

6.2 Future Work

The current work was successful in generalizing MSG for aperiodic solid and free-edge problems, which are two important problems in heterogeneous structural analysis. The next step in this research direction is to extend it to porous materials, beams of variable cross section and microstructures such as rotor blade, and plate with variable thickness and microstructures. For porous material, the proposed volume integral constraints does not hold due to the existence of the void part on the SG boundaries. Therefore, special techniques must be developed. For beams with variable cross sections and microstructures and plates with variable thickness, periodicity does not exist in any direction, which leads to significant complexity in the microstructural analysis. A possible research direction is to find a systematic way to identify proper SGs and constraints so that the solution error can be estimated and also bounded within an acceptable range. In addition, a multiscale free-edge analysis considering the progressive failure of fiber and matrix can also be done in the future.

REFERENCES

REFERENCES

[1] R. Hill, "Elastic properties of reinforced solids: some theoretical principles," *Journal of the Mechanics and Physics of Solids*, vol. 11, no. 5, pp. 357–372, 1963.

[2] ——, "A self-consistent mechanics of composite materials," *Journal of the Mechanics and Physics of Solids*, vol. 13, no. 4, pp. 213–222, 1965.

[3] R. B. Pipes and N. J. Pagano, "Interlaminar stresses in composite laminates-an approximate elasticity solution," *Journal of Applied Mechanics*, vol. 41, no. 3, pp. 668–672, 1974.

[4] W. S. Chan and O. O. Ochoa, "An integrated finite element model of edge-delamination analysis for laminates due to tension, bending, and torsion loads," in *28th AIAA/ASME/AHS Structures, Structural Dynamics, and Material Conference, Monterey, CA, April*, 1987, p. 2735.

[5] P. Kanouté, D. P. Boso, J. L. Chaboche, and B. A. Schrefler, "Multiscale methods for composites: a review," *Archives of Computational Methods in Engineering*, vol. 16, no. 1, pp. 31–75, 2009.

[6] T. Belytschko and J. H. Song, "Coarse-graining of multiscale crack propagation," *International Journal for Numerical Methods in Engineering*, vol. 81, no. 5, pp. 537–563, 2010.

[7] J. C. Michel and P. Suquet, "Nonuniform transformation field analysis," *International Journal of Solids and Structures*, vol. 40, no. 25, pp. 6937–6955, 2003.

[8] ——, "Computational analysis of nonlinear composite structures using the nonuniform transformation field analysis," *Computer Methods in Applied Mechanics and Engineering*, vol. 193, no. 48-51, pp. 5477–5502, 2004.

[9] B. A. Bednarcyk and S. M. Arnold, "Micromechanics-based deformation and failure prediction for longitudinally reinforced titanium composites," *Composites Science and Technology*, vol. 61, no. 5, pp. 705–729, 2001.

[10] A. Bensoussan, J. L. Lions, and G. Papanicolaou, *Asymptotic Analysis for Periodic Structures.* American Mathematical Society, 2011, vol. 374.

[11] S. J. Hollister, D. P. Fyhrie, K. J. Jepsen, and S. A. Goldstein, "Application of homogenization theory to the study of trabecular bone mechanics," *Journal of Biomechanics*, vol. 24, no. 9, pp. 825–839, 1991.

[12] K. Lee and S. Ghosh, "Small deformation multi-scale analysis of heterogeneous materials with the voronoi cell finite element model and homogenization theory," *Computational Materials Science*, vol. 7, no. 1, pp. 131–146, 1996.

[13] J. Fish, K. Shek, M. Pandheeradi, and M. S. Shephard, "Computational plasticity for composite structures based on mathematical homogenization: Theory and practice," *Computer Methods in Applied Mechanics and Engineering*, vol. 148, no. 1, pp. 53–73, 1997.

[14] F. Feyel and J. L. Chaboche, "FE^2 multiscale approach for modelling the elastoviscoplastic behaviour of long fibre Sic/Ti composite materials," *Computer Methods in Applied Mechanics and Engineering*, vol. 183, no. 3-4, pp. 309–330, 2000.

[15] F. Feyel, "A multilevel finite element method (FE^2) to describe the response of highly non-linear structures using generalized continua," *Computer Methods in Applied Mechanics and Engineering*, vol. 192, no. 28-30, pp. 3233–3244, 2003.

[16] N. Buannic and P. Cartraud, "Higher-order effective modeling of periodic heterogeneous beams. I. asymptotic expansion method," *International Journal of Solids and Structures*, vol. 38, no. 40-41, pp. 7139–7161, 2001.

[17] S. Kruch, "Homogenized and relocalized mechanical fields," *The Journal of Strain Analysis for Engineering Design*, vol. 42, no. 4, pp. 215–226, 2007.

[18] H. M. Sertse, "Micromechanics based failure analysis of heterogeneous materials," Ph.D. dissertation, Purdue University, 2017.

[19] P. A. Guidault, O. Allix, L. Champaney, and J. P. Navarro, "A two-scale approach with homogenization for the computation of cracked structures," *Computers & Structures*, vol. 85, no. 17-18, pp. 1360–1371, 2007.

[20] A. Ibrahimbegović and D. Markovič, "Strong coupling methods in multi-phase and multi-scale modeling of inelastic behavior of heterogeneous structures," *Computer Methods in Applied Mechanics and Engineering*, vol. 192, no. 28-30, pp. 3089–3107, 2003.

[21] W. K. Liu and C. McVeigh, "Predictive multiscale theory for design of heterogeneous materials," *Computational Mechanics*, vol. 42, no. 2, pp. 147–170, 2008.

[22] S. Ghosh, K. Lee, and P. Raghavan, "A multi-level computational model for multi-scale damage analysis in composite and porous materials," *International Journal of Solids and Structures*, vol. 38, no. 14, pp. 2335–2385, 2001.

[23] G. Nilakantan, M. Keefe, T. A. Bogetti, and J. W. Gillespie Jr, "Multiscale modeling of the impact of textile fabrics based on hybrid element analysis," *International Journal of Impact Engineering*, vol. 37, no. 10, pp. 1056–1071, 2010.

[24] W. Yu, "A unified theory for constitutive modeling of composites," *Journal of Mechanics of Materials and Structures*, vol. 11, no. 4, pp. 379–411, 2016.

[25] H. J. Böhm, "A short introduction to continuum micromechanics," in *Mechanics of Microstructured Materials.* Springer, 2004, pp. 1–40.

[26] S. Pecullan, L. V. Gibiansky, and S. Torquato, "Scale effects on the elastic behavior of periodic and hierarchical two-dimensional composites," *Journal of the Mechanics and Physics of Solids*, vol. 47, no. 7, pp. 1509–1542, 1999.

[27] M. Ostoja-Starzewski, "Material spatial randomness: From statistical to representative volume element," *Probabilistic Engineering Mechanics*, vol. 21, no. 2, pp. 112–132, 2006.

[28] S. Hazanov, "Hill condition and overall properties of composites," *Archive of Applied Mechanics*, vol. 68, no. 6, pp. 385–394, 1998.

[29] P. J. Blanco, P. J. Sánchez, E. A. de Souza Neto, and R. A. Feijóo, "Variational foundations and generalized unified theory of RVE-based multiscale models," *Archives of Computational Methods in Engineering*, vol. 23, no. 2, pp. 191–253, 2016.

[30] D. H. Pahr and H. J. Böhm, "Assessment of mixed uniform boundary conditions for predicting the mechanical behavior of elastic and inelastic discontinuously reinforced composites," *Computer Modeling in Engineering and Sciences*, vol. 34, no. 2, pp. 117–136, 2008.

[31] H. J. Böhm, "A short introduction to basic aspects of continuum micromechanics," Vienna University of Technology, ILSB Report 206, 2011. [Online]. Available: www.ilsb.tuwien.ac.at/links/downloads/cdlfmdrep03.pdf

[32] D. H. Pahr and P. K. Zysset, "Influence of boundary conditions on computed apparent elastic properties of cancellous bone," *Biomechanics and Modeling in Mechanobiology*, vol. 7, no. 6, pp. 463–476, 2008.

[33] S. D. Mesarovic and J. Padbidri, "Minimal kinematic boundary conditions for simulations of disordered microstructures," *Philosophical Magazine*, vol. 85, no. 1, pp. 65–78, 2005.

[34] E. A. de Souza Neto and R. A. Feijóo, "Variational foundations of large strain multiscale solid constitutive models: kinematical formulation," *Advanced Computational Materials Modeling: From Classical to Multi-Scale Techniques*, pp. 341–378, 2010.

[35] C. Huet, "Application of variational concepts to size effects in elastic heterogeneous bodies," *Journal of the Mechanics and Physics of Solids*, vol. 38, no. 6, pp. 813–841, 1990.

[36] S. J. Hollister and N. Kikuchi, "A comparison of homogenization and standard mechanics analyses for periodic porous composites," *Computational Mechanics*, vol. 10, no. 2, pp. 73–95, 1992.

[37] M. Jiang, M. Ostoja-Starzewski, and I. Jasiuk, "Scale-dependent bounds on effective elastoplastic response of random composites," *Journal of the Mechanics and Physics of Solids*, vol. 49, no. 3, pp. 655–673, 2001.

[38] K. Terada, M. Hori, T. Kyoya, and N. Kikuchi, "Simulation of the multi-scale convergence in computational homogenization approaches," *International Journal of Solids and Structures*, vol. 37, no. 16, pp. 2285–2311, 2000.

[39] M. J. Pindera, H. Khatam, A. S. Drago, and Y. Bansal, "Micromechanics of spatially uniform heterogeneous media: a critical review and emerging approaches," *Composites Part B: Engineering*, vol. 40, no. 5, pp. 349–378, 2009.

[40] F. Bouyge, I. Jasiuk, S. Boccara, and M. Ostoja-Starzewski, "A micromechanically based couple-stress model of an elastic orthotropic two-phase composite," *European Journal of Mechanics-A/Solids*, vol. 21, no. 3, pp. 465–481, 2002.

[41] M. Ostoja-Starzewski, "Random field models of heterogeneous materials," *International Journal of Solids and Structures*, vol. 35, no. 19, pp. 2429–2455, 1998.

[42] W. J. Drugan and J. R. Willis, "A micromechanics-based nonlocal constitutive equation and estimates of representative volume element size for elastic composites," *Journal of the Mechanics and Physics of Solids*, vol. 44, no. 4, pp. 497–524, 1996.

[43] Z. F. Khisaeva and M. Ostoja-Starzewski, "On the size of RVE in finite elasticity of random composites," *Journal of Elasticity*, vol. 85, no. 2, pp. 153–173, 2006.

[44] F. Larsson, K. Runesson, S. Saroukhani, and R. Vafadari, "Computational homogenization based on a weak format of micro-periodicity for RVE-problems," *Computer Methods in Applied Mechanics and Engineering*, vol. 200, no. 1, pp. 11–26, 2011.

[45] V. D. Nguyen, E. Béchet, C. Geuzaine, and L. Noels, "Imposing periodic boundary condition on arbitrary meshes by polynomial interpolation," *Computational Materials Science*, vol. 55, pp. 390–406, 2012.

[46] Z. Yuan and J. Fish, "Toward realization of computational homogenization in practice," *International Journal for Numerical Methods in Engineering*, vol. 73, no. 3, p. 361, 2008.

[47] S. Jacques, I. De Baere, and W. Van Paepegem, "Application of periodic boundary conditions on multiple part finite element meshes for the meso-scale homogenization of textile fabric composites," *Composites Science and Technology*, vol. 92, pp. 41–54, 2014.

[48] P. Tan, L. Tong, and G. P. Steven, "Modelling for predicting the mechanical properties of textile composites-a review," *Composites Part A: Applied Science and Manufacturing*, vol. 28, no. 11, pp. 903–922, 1997.

[49] ——, "Behavior of 3D orthogonal woven CFRP composites. part II. FEA and analytical modeling approaches," *Composites Part A: Applied Science and Manufacturing*, vol. 31, no. 3, pp. 273–281, 2000.

[50] D. Scida, Z. Aboura, M. L. Benzeggagh, and E. Bocherens, "A micromechanics model for 3D elasticity and failure of woven-fibre composite materials," *Composites Science and Technology*, vol. 59, no. 4, pp. 505–517, 1999.

[51] N. K. Naik and V. K. Ganesh, "Failure behavior of plain weave fabric laminates under on-axis uniaxial tensile loading: I-analytical predictions," *Journal of Composite Materials*, vol. 30, no. 16, pp. 1779–1822, 1996.

[52] T. Ishikawa, M. Matsushima, Y. Hayashi, and T. W. Chou, "Experimental confirmation of the theory of elastic moduli of fabric composites," *Journal of Composite Materials*, vol. 19, no. 5, pp. 443–458, 1985.

[53] D. S. Ivanov, S. V. Lomov, S. G. Ivanov, and I. Verpoest, “Stress distribution in outer and inner plies of textile laminates and novel boundary conditions for unit cell analysis,” *Composites Part A: Applied Science and Manufacturing*, vol. 41, no. 4, pp. 571–580, 2010.

[54] D. S. Ivanov, S. G. Ivanov, S. V. Lomov, and I. Verpoest, “Unit cell modelling of textile laminates with arbitrary inter-ply shifts,” *Composites Science and Technology*, vol. 72, no. 1, pp. 14–20, 2011.

[55] J. Gager and H. E. Pettermann, “Numerical homogenization of textile composites based on shell element discretization,” *Composites Science and Technology*, vol. 72, no. 7, pp. 806–812, 2012.

[56] ——, “FEM modeling of multilayered textile composites based on shell elements,” *Composites Part B: Engineering*, vol. 77, pp. 46–51, 2015.

[57] J. J. Espadas-Escalante, N. P. van Dijk, and P. Isaksson, “A study on the influence of boundary conditions in computational homogenization of periodic structures with application to woven composites,” *Composite Structures*, vol. 160, pp. 529–537, 2017.

[58] C. Mittelstedt and W. Becker, “Free-edge effects in composite laminates,” *Applied Mechanics Reviews*, vol. 60, no. 5, pp. 217–245, 2007.

[59] T. Kant and K. Swaminathan, “Estimation of transverse/interlaminar stresses in laminated composites–a selective review and survey of current developments,” *Composite Structures*, vol. 49, no. 1, pp. 65–75, 2000.

[60] R. B. Pipes and N. J. Pagano, “Interlaminar stresses in composite laminates under uniform axial extension,” *Journal of Composite Materials*, vol. 4, no. 4, pp. 538–548, 1970.

[61] A. S. D. Wang and F. W. Crossman, “Some new results on edge effect in symmetric composite laminates,” *Journal of Composite Materials*, vol. 11, no. 1, pp. 92–106, 1977.

[62] S. S. Wang and F. G. Yuan, “A singular hybrid finite element analysis of boundary-layer stresses in composite laminates,” *International Journal of Solids and Structures*, vol. 19, no. 9, pp. 825–837, 1983.

[63] S. G. Leknitskii and P. Fern, *Theory of Elasticity of an Anisotropic Elastic Body*. Holden-Day, 1963.

[64] R. B. Pipes, J. Goodsell, A. Ritchey, J. Dustin, and J. Gosse, “Interlaminar stresses in composite laminates: thermoelastic deformation,” *Composites Science and Technology*, vol. 70, no. 11, pp. 1605–1611, 2010.

[65] J. Goodsell, N. J. Pagano, O. Kravchenko, and R. B. Pipes, “Interlaminar stresses in composite laminates subjected to anticlastic bending deformation,” *Journal of Applied Mechanics*, vol. 80, no. 4, p. 041020, 2013.

[66] J. Goodsell and R. B. Pipes, “Free-edge interlaminar stresses in angle-ply laminates: a family of analytic solutions,” *Journal of Applied Mechanics*, vol. 83, no. 5, p. 051010, 2016.

[67] P. W. Hsu and C. T. Herakovich, "Edge effects in angle-ply composite laminates," *Journal of Composite Materials*, vol. 11, no. 4, pp. 422–428, 1977.

[68] S. Tang and A. Levy, "A boundary layer theory-part ii: extension of laminated finite strip," *Journal of Composite Materials*, vol. 9, no. 1, pp. 42–52, 1975.

[69] N. J. Pagano, "On the calculation of interlaminar normal stress in composite laminate," *Journal of Composite Materials*, vol. 8, no. 1, pp. 65–81, 1974.

[70] W. Becker, "Closed-form solution for the free-edge effect in cross-ply laminates," *Composite Structures*, vol. 26, no. 1, pp. 39–45, 1993.

[71] ——, "Closed-form analysis of the free edge effect in angle-ply laminates," *Journal of Applied Mechanics*, vol. 61, no. 1, pp. 209–211, 1994.

[72] A. V. K. Murty and H. K. H. Kumar, "Modelling of symmetric laminates under extension," *Composite Structures*, vol. 11, no. 1, pp. 15–32, 1989.

[73] M. Tahani and A. Nosier, "Edge effects of uniformly loaded cross-ply composite laminates," *Materials & Design*, vol. 24, no. 8, pp. 647–658, 2003.

[74] ——, "Free edge stress analysis of general cross-ply composite laminates under extension and thermal loading," *Composite Structures*, vol. 60, no. 1, pp. 91–103, 2003.

[75] A. Nosier and A. Bahrami, "Free-edge stresses in antisymmetric angle-ply laminates in extension and torsion," *International Journal of Solids and Structures*, vol. 43, no. 22, pp. 6800–6816, 2006.

[76] ——, "Interlaminar stresses in antisymmetric angle-ply laminates," *Composite Structures*, vol. 78, no. 1, pp. 18–33, 2007.

[77] A. Nosier and M. Maleki, "Free-edge stresses in general composite laminates," *International Journal of Mechanical Sciences*, vol. 50, no. 10, pp. 1435–1447, 2008.

[78] H. Y. Sarvestani and M. Y. Sarvestani, "Free-edge stress analysis of general composite laminates under extension, torsion and bending," *Applied Mathematical Modelling*, vol. 36, no. 4, pp. 1570–1588, 2012.

[79] C. Kassapoglou and P. A. Lagace, "An efficient method for the calculation of interlaminar stresses in composite materials," *Journal of Applied Mechanics*, vol. 53, no. 4, pp. 744–750, 1986.

[80] C. C. Lin, C. Y. Hsu, and C. C. Ko, "Interlaminar stresses in general laminates with straight free edges," *AIAA Journal*, vol. 33, no. 8, pp. 1471–1476, 1995.

[81] W. L. Yin, "Free-edge effects in anisotropic laminates under extension, bending and twisting, part i: a stress-function-based variational approach," *Journal of Applied Mechanics*, vol. 61, no. 2, pp. 410–415, 1994.

[82] ——, "Free-edge effects in anisotropic laminates under extension, bending, and twisting, part ii: eigenfunction analysis and the results for symmetric laminates," *Journal of Applied Mechanics*, vol. 61, no. 2, pp. 416–421, 1994.

[83] T. Kim and S. N. Atluri, "Interlaminar stresses in composite laminates under out-of-plane shear/bending," *AIAA Journal*, vol. 32, no. 8, pp. 1700–1708, 1994.

[84] ——, "Analysis of edge stresses in composite laminates under combined thermo-mechanical loading, using a complementary energy approach," *Computational Mechanics*, vol. 16, no. 2, pp. 83–97, 1995.

[85] M. Cho and H. S. Kim, "Iterative free-edge stress analysis of composite laminates under extension, bending, twisting and thermal loadings," *International Journal of Solids and Structures*, vol. 37, no. 3, pp. 435–459, 2000.

[86] M. Tahani and A. Andakhshideh, "Interlaminar stresses in thick rectangular laminated plates with arbitrary laminations and boundary conditions under transverse loads," *Composite Structures*, vol. 94, no. 5, pp. 1793–1804, 2012.

[87] A. Andakhshideh and M. Tahani, "Free-edge stress analysis of general rectangular composite laminates under bending, torsion and thermal loads," *European Journal of Mechanics-A/Solids*, vol. 42, pp. 229–240, 2013.

[88] N. Dhanesh, S. Kapuria, and G. G. S. Achary, "Accurate prediction of three-dimensional free edge stress field in composite laminates using mixed-field multiterm extended kantorovich method," *Acta Mechanica*, pp. 1–25, 2016.

[89] E. Carrera, "Theories and finite elements for multilayered, anisotropic, composite plates and shells," *Archives of Computational Methods in Engineering*, vol. 9, no. 2, pp. 87–140, 2002.

[90] M. D'Ottavio, P. Vidal, E. Valot, and O. Polit, "Assessment of plate theories for free-edge effects," *Composites Part B: Engineering*, vol. 48, pp. 111–121, 2013.

[91] C. Wenzel, M. D'Ottavio, O. Polit, and P. Vidal, "Assessment of free-edge singularities in composite laminates using higher-order plate elements," *Mechanics of Advanced Materials and Structures*, vol. 23, pp. 1–44, 2015.

[92] P. Vidal, L. Gallimard, and O. Polit, "Assessment of variable separation for finite element modeling of free edge effect for composite plates," *Composite Structures*, vol. 123, pp. 19–29, 2015.

[93] R. Esquej, L. Castejon, M. Lizaranzu, M. Carrera, A. Miravete, and R. Miralbes, "A new finite element approach applied to the free edge effect on composite materials," *Composite Structures*, vol. 98, pp. 121–129, 2013.

[94] U. Icardi and A. M. Bertetto, "An evaluation of the influence of geometry and of material properties at free edges and at corners of composite laminates," *Computers & Structures*, vol. 57, no. 4, pp. 555–571, 1995.

[95] V. T. Nguyen and J. F. Caron, "Finite element analysis of free-edge stresses in composite laminates under mechanical and thermal loading," *Composites Science and Technology*, vol. 69, no. 1, pp. 40–49, 2009.

[96] U. Icardi, S. Locatto, and A. Longo, "Assessment of recent theories for predicting failure of composite laminates," *Applied Mechanics Reviews*, vol. 60, no. 2, pp. 76–86, 2007.

[97] I. M. Daniel and O. Ishai, *Engineering Mechanics of Composite Materials*. Oxford University Press, New York, 1994, vol. 3.

[98] S. W. Tsai, "Strength characteristics of composite materials." Philco Corp Newport Beach CA, Tech. Rep., 1965.

[99] S. W. Tsai and E. M. Wu, "A general theory of strength for anisotropic materials," *Journal of Composite Materials*, vol. 5, no. 1, pp. 58–80, 1971.

[100] I. M. Daniel, "Failure of composite materials," *Strain*, vol. 43, no. 1, pp. 4–12, 2007.

[101] C. T. Sun, "Strength analysis of unidirectional composites and laminates," pp. 641–666, 2000.

[102] R. B. Pipes and B. W. Cole, "On the off-axis strength test for anisotropic materials1," *Journal of Composite Materials*, vol. 7, no. 2, pp. 246–256, 1973.

[103] S. R. Swanson, M. J. Messick, and Z. Tian, "Failure of carbon/epoxy lamina under combined stress," *Journal of Composite Materials*, vol. 21, no. 7, pp. 619–630, 1987.

[104] Z. Hashin and A. Rotem, "A fatigue failure criterion for fiber reinforced materials," *Journal of Composite Materials*, vol. 7, no. 4, pp. 448–464, 1973.

[105] Z. Hashin, "Failure criteria for unidirectional fiber composites," *Journal of Applied Mechanics*, vol. 47, no. 2, pp. 329–334, 1980.

[106] C. T. Sun, "Comparative evaluation of failure analysis methods for composite laminates," DOT/FAA/AR-95/109, Tech. Rep., 1996.

[107] J. E. Bailey, P. T. Curtis, and A. Parvizi, "On the transverse cracking and longitudinal splitting behaviour of glass and carbon fibre reinforced epoxy cross ply laminates and the effect of poisson and thermally generated strain," *Proceedings of the Royal Society of London, A*, vol. 366, no. 1727, pp. 599–623, 1979.

[108] D. L. Flaggs and M. H. Kural, "Experimental determination of the in situ transverse lamina strength in graphite/epoxy laminates," *Journal of Composite Materials*, vol. 16, no. 2, pp. 103–116, 1982.

[109] C. T. Sun and J. Tao, "Prediction of failure envelopes and stress/strain behaviour of composite laminates1," *Composites Science and Technology*, vol. 58, no. 7, pp. 1125–1136, 1998.

[110] A. Puck, "Calculating the strength of glass fibre/plastic laminates under combined load," *Kunststoffe*, vol. 55, pp. 18–19, 1969.

[111] A. Puck and W. Schneider, "On failure mechanisms and failure criteria of filament-wound glass-fibre/resin composites," *Plastics* & *Polymers*, vol. 37, no. 127, pp. 33–34, 1969.

[112] A. Puck, "Fracture criteria for highly stressed fibre-plastic composites which meet requirements of design practice," *Kunststoffe*, vol. 82, pp. 34–38, 1992.

[113] A. Puck and H. Schürmann, "Failure analysis of FRP laminates by means of physically based phenomenological models," *Composites Science and Technology*, vol. 62, no. 12-13, pp. 1633–1662, 2002.

[114] ——, "Failure analysis of FRP laminates by means of physically based phenomenological models," in *Failure Criteria in Fibre-Reinforced-Polymer Composites*. Elsevier, 2004, pp. 832–876.

[115] M. Steven, C. Andrew, and J. Hansen, "Multicontinuum failure analysis of composite structural laminates," *Mechanics of Composite Materials and Structures*, vol. 8, no. 4, pp. 249–262, 2001.

[116] C. Davila, N. Jaunky, and S. Goswami, "Failure criteria for FRP laminates in plane stress," in *44th AIAA/ASME/ASCE/AHS/ASC Structures, Structural Dynamics, and Materials Conference*, 2003, p. 1991.

[117] S. K. Ha, K. K. Jin, and Y. Huang, "Micro-mechanics of failure (MMF) for continuous fiber reinforced composites," *Journal of Composite Materials*, vol. 42, no. 18, pp. 1873–1895, 2008.

[118] T. E. Tay, G. Liu, V. B. C. Tan, X. S. Sun, and D. C. Pham, "Progressive failure analysis of composites," *Journal of Composite Materials*, vol. 42, no. 18, pp. 1921–1966, 2008.

[119] P. Pal and C. Ray, "Progressive failure analysis of laminated composite plates by finite element method," *Journal of Reinforced Plastics and Composites*, vol. 21, no. 16, pp. 1505–1513, 2002.

[120] W. C. Hwang and C. T. Sun, "Failure analysis of laminated composites by using iterative three-dimensional finite element method," *Computers & Structures*, vol. 33, no. 1, pp. 41–47, 1989.

[121] S. Tolson and N. Zabaras, "Finite element analysis of progressive failure in laminated composite plates," *Computers & Structures*, vol. 38, no. 3, pp. 361–376, 1991.

[122] Y. S. N. Reddy, C. M. D. Moorthy, and J. N. Reddy, "Non-linear progressive failure analysis of laminated composite plates," *International Journal of Non-Linear Mechanics*, vol. 30, no. 5, pp. 629–649, 1995.

[123] A. Matzenmiller, J. Lubliner, and R. L. Taylor, "A constitutive model for anisotropic damage in fiber-composites," *Mechanics of Materials*, vol. 20, no. 2, pp. 125–152, 1995.

[124] A. Turon, P. P. Camanho, J. Costa, and C. G. Dávila, "A damage model for the simulation of delamination in advanced composites under variable-mode loading," *Mechanics of Materials*, vol. 38, no. 11, pp. 1072–1089, 2006.

[125] P. Maimí, P. P. Camanho, J. A. Mayugo, and C. G. Dávila, "A thermodynamically consistent damage model for advanced composites," 2006.

[126] P. P. Camanho, P. Maimí, and C. G. Dávila, "Prediction of size effects in notched laminates using continuum damage mechanics," *Composites Science and Technology*, vol. 67, no. 13, pp. 2715–2727, 2007.

[127] P. Maimí, P. P. Camanho, J. A. Mayugo, and C. G. Dávila, "A continuum damage model for composite laminates: Part I–constitutive model," *Mechanics of Materials*, vol. 39, no. 10, pp. 897–908, 2007.

[128] I. Lapczyk and J. A. Hurtado, "Progressive damage modeling in fiber-reinforced materials," *Composites Part A: Applied Science and Manufacturing*, vol. 38, no. 11, pp. 2333–2341, 2007.

[129] P. F. Liu and J. Y. Zheng, "Recent developments on damage modeling and finite element analysis for composite laminates: A review," *Materials & Design*, vol. 31, no. 8, pp. 3825–3834, 2010.

[130] Z. P. Bažant and B. H. Oh, "Crack band theory for fracture of concrete," *Matériaux et Construction*, vol. 16, no. 3, pp. 155–177, 1983.

[131] G. Duvant and J. L. Lions, *Inequalities in Mechanics and Physics*. Springer Science & Business Media, 2012, vol. 219.

[132] J. C. Simo and T. J. R. Hughes, *Computational Inelasticity*. Springer Science & Business Media, 2006, vol. 7.

[133] W. Yu, "Structure genome: fill the gap between materials genome and structural analysis," in *56th AIAA/ASCE/AHS/ASC Structures, Structural Dynamics, and Materials Conference*, 2015, p. 0201.

[134] ——, "An introduction to micromechanics," *Applied Mechanics and Materials*, vol. 828, pp. 3–24, 2016.

[135] V. Berdichevsky, *Variational Principles of Continuum Mechanics: I. Fundamentals*. Springer Science & Business Media, 2009.

[136] W. Yu, "Swiftcomp user manual," *West Lafayette, IN 47907*, 2015. [Online]. Available: https://cdmhub.org/resources/scstandard/supportingdocs

[137] W. Yu, D. H. Hodges, and J. C. Ho, "Variational asymptotic beam sectional analysis–an updated version," *International Journal of Engineering Science*, vol. 59, pp. 40–64, 2012.

[138] C. Y. Lee, W. Yu, and D. H. Hodges, "Refined modeling of composite plates with in-plane heterogeneity," *ZAMM-Journal of Applied Mathematics and Mechanics*, vol. 94, no. 1-2, pp. 85–100, 2014.

[139] W. Yu, V. V. Volovoi, D. H. Hodges, and X. Hong, "Validation of the variational asymptotic beam sectional analysis," *AIAA Journal*, vol. 40, no. 10, pp. 2105–2112, 2002.

[140] L. Demasi and W. Yu, "Assess the accuracy of the variational asymptotic plate and shell analysis using the generalized unified formulation," *Mechanics of Advanced Materials and Structures*, vol. 20, no. 3, pp. 227–241, 2013.

[141] B. Peng, J. Goodsell, R. B. Pipes, and W. Yu, "Generalized free-edge stress analysis using mechanics of structure genome," *Journal of Applied Mechanics*, vol. 83, no. 10, p. 101013, 2016.

[142] O. A. Bauchau and S. Han, “Three-dimensional beam theory for flexible multibody dynamics,” *Journal of Computational and Nonlinear Dynamics*, vol. 9, no. 4, p. 041011, 2014.

[143] P. J. Couturier, S. Krenk, and J. Høgsberg, “Beam section stiffness properties using a single layer of 3D solid elements,” *Computers & Structures*, vol. 156, pp. 122–133, 2015.

[144] S. Han and O. Bauchau, “On the analysis of periodically heterogeneous beams,” *Journal of Applied Mechanics*, vol. 83, no. 9, p. 091001, 2016.

[145] L. Xu, G. Cheng, and S. Yi, “A new method of shear stiffness prediction of periodic timoshenko beams,” *Mechanics of Advanced Materials and Structures*, vol. 23, no. 6, pp. 670–680, 2016.

[146] V. L. Berdichevskii, “Variational-asymptotic method of constructing a theory of shells,” *Journal of Applied Mathematics and Mechanics*, vol. 43, no. 4, pp. 711–736, 1979.

[147] A. F. Bower, *Applied Mechanics of Solids*. CRC Press, 2009.

[148] U. Andelfinger and E. Ramm, “EAS-elements for two-dimensional, three-dimensional, plate and shell structures and their equivalence to HR-elements,” *International Journal for Numerical Methods in Engineering*, vol. 36, no. 8, pp. 1311–1337, 1993.

[149] M. D. S. Cook, R. D., M. E. Plesha, and R. J. Witt, *Concepts and Applications of Finite Element Analysis*. Wiley New York, 1974, vol. 4.

[150] J. C. Nagtegaal, D. M. Parks, and J. R. Rice, “On numerically accurate finite element solutions in the fully plastic range,” *Computer Methods in Applied Mechanics and Engineering*, vol. 4, no. 2, pp. 153–177, 1974.

[151] S. W. Sloan and M. F. Randolph, “Numerical prediction of collapse loads using finite element methods,” *International Journal for Numerical and Analytical Methods in Geomechanics*, vol. 6, no. 1, pp. 47–76, 1982.

[152] D. S. Malkus and T. J. Hughes, “Mixed finite element methodsreduced and selective integration techniques: a unification of concepts,” *Computer Methods in Applied Mechanics and Engineering*, vol. 15, no. 1, pp. 63–81, 1978.

[153] T. J. Hughes, *The Finite Element Method: Linear Static and Dynamic Finite Element Analysis*. Courier Corporation, 2012.

[154] Z. Hashin and B. W. Rosen, “The elastic moduli of fiber-reinforced materials,” *Journal of Applied Mechanics*, vol. 31, no. 2, pp. 223–232, 1964.

[155] S. Hazanov and C. Huet, “Order relationships for boundary conditions effect in heterogeneous bodies smaller than the representative volume,” *Journal of the Mechanics and Physics of Solids*, vol. 42, no. 12, pp. 1995–2011, 1994.

[156] Z. Hashin, “Analysis of properties of fiber composites with anisotropic constituents,” *Journal of Applied Mechanics*, vol. 46, no. 3, pp. 543–550, 1979.

[157] S. Firooz, S. Saeb, G. Chatzigeorgiou, F. Meraghni, P. Steinmann, and A. Javili, “Systematic study of homogenization and the utility of circular simplified representative volume element,” *Mathematics and Mechanics of Solids*, 2019. [Online]. Available: https://doi.org/10.1177/1081286518823834

[158] D. Scida, Z. Aboura, M. L. Benzeggagh, and E. Bocherens, “Prediction of the elastic behaviour of hybrid and non-hybrid woven composites,” *Composites Science and Technology*, vol. 57, no. 12, pp. 1727–1740, 1998.

[159] M. V. Donadon, B. G. Falzon, L. Iannucci, and J. M. Hodgkinson, “A 3-d micromechanical model for predicting the elastic behaviour of woven laminates,” *Composites Science and Technology*, vol. 67, no. 11, pp. 2467–2477, 2007.

[160] P. Upadhyaya and C. S. Upadhyay, “A three-dimensional micromechanical model to predict the viscoelastic behavior of woven composites,” *Composite Structures*, vol. 93, no. 11, pp. 2733–2739, 2011.

[161] X. Liu, K. Rouf, B. Peng, and W. Yu, “Two-step homogenization of textile composites using mechanics of structure genome,” *Composite Structures*, vol. 171, pp. 252–262, 2017.

[162] M. R. E. Nasution, N. Watanabe, A. Kondo, and A. Yudhanto, “A novel asymptotic expansion homogenization analysis for 3-d composite with relieved periodicity in the thickness direction,” *Composites Science and Technology*, vol. 97, pp. 63–73, 2014.

[163] B. Peng and W. Yu, “Remove homogeneous layer assumption from lamination theories,” in *American Society of Composites-30th Technical Conference*, EastLanding,Michigan, September 2015.

[164] H. M. Sertse, J. Goodsell, A. J. Ritchey, R. B. Pipes, and W. Yu, “Challenge problems for the benchmarking of micromechanics analysis: Level I initial results,” *Journal of Composite Materials*, 2017.

[165] C. Y. Lee, “Micro-mechanical approach for spanwise periodically and heterogeneously beam-like structures,” , vol. 36, no. 3, pp. 9–16, 2016.

[166] C. Y. Lee and W. Yu, “Variational asymptotic modeling of composite beams with spanwise heterogeneity,” *Computers & Structures*, vol. 89, no. 15, pp. 1503–1511, 2011.

[167] D. H. Hodges, “A mixed variational formulation based on exact intrinsic equations for dynamics of moving beams,” *International Journal of Solids and Structures*, vol. 26, no. 11, pp. 1253 – 1273, 1990.

[168] W. Yu, “Variational asymptotic modeling of composite dimensionally reducible structures,” Ph.D. dissertation, Aerospace Engineering, Georgia Institute of Technology, May 2002.

[169] D. A. Danielson and D. H. Hodges, “Nonlinear beam kinematics by decomposition of the rotation tensor,” *Journal of Applied Mechanics*, vol. 54, no. 2, pp. 258–262, 1987.

[170] D. H. Hodges, *Nonlinear Composite Beam Theory*. American Institute of Aeronautics and Astronautics, 2006.

[171] W. Yu, *Multiscale Structural Mechanics: Top-Down Modelling of Composites using the Structural Genome*. Wiley Online Library, to appear.

[172] N. Liu and W. Yu, "Evaluation of smeared properties approaches and mechanics of structure genome for analyzing composite beams," *Mechanics of Advanced Materials and Structures*, vol. 25, no. 14, pp. 1171–1185, 2018.

[173] S. W. Tsai and J. D. D. Melo, "A unit circle failure criterion for carbon fiber reinforced polymer composites," *Composites Science and Technology*, vol. 123, pp. 71–78, 2016.